STUDIES OF SUSPENSION BEHAVIOR

I. Instabilities of Non-Brownian Suspensions

II. Microrheology of Colloidal Suspensions

Thesis by

Ileana Cristina Carpen

In Partial Fulfillment of the Requirements

for the Degree of

Doctor of Philosophy

California Institute of Technology

Pasadena, California

2005

(Submitted October 29, 2004)

To Victor Nicolae (Bebe) Carpen, 1972-2001

Acknowledgments

"No man is an island," said Donne, and that is true in graduate school as in everything. I wish I could name all of those who have affected my path, but then this section would be most of the thesis. And lest you wonder, I leave sarcasm (my constant companion) at the door today as I write these words. Thank you all.

I want to thank John Brady for all of his help (also his patience and tolerance). I have great respect for him and his work ethic. Though others may wonder about their 'what ifs', given the choice I would work with him again.

My thesis committee: Julia Kornfield, Zhen-Gang Wang and Todd Squires: thank you for helping the great escape, and especially for your donated time and interesting questions.

I thank the Brady 'Bunch', past and present, for help and moral support. In particular, Ganesh Subramanian and David Fang have been and remain some of my best friends, but I am fond of the entire group and hope we meet again over the years. I shall miss our afternoon coffee breaks and the extremely random conversations.

Through rain, wind, and deadly California pollen, Andrea Wight and I made our way to the Red Door Café every morning for our dose of caffeine and stress relief. Andrea, the only other woman in my class, was there with me through the good and the bad, and fought the losing battle of trying to break me of my procrastination. I am fortunate in having her as a friend.

Graduate school can be an intense experience—the people I have known throughout my five years here have made it a cheerful one. My friends in the department have been there for help and for a laugh: Jimmy, Eric, Dean and the rest of the class, and Niki, Jenny, Adam, and Gordon among others. Mike Gordon in particular was a source of continuous amazement and amusement.

The staff up on the second floor have my heartfelt appreciation, and particular thanks go to Kathy Bubash, the all-knowing graduate program secretary, Suresh Guptha, our patient computer guru, Margie Dowens, John's secretary for most of my time here, and Donna Johnson, who took over.

Some of my best friendships date back to my involvement with the Graduate Student Council. Chip Sumner, Mike Fleming, and Heather Cox—for time spent talking about what is wrong with the world, and how we could do so much better than the people in charge—thank you.

But my last and best thanks go to my family. For their patience and unconditional love, as well as for the more than occasional restocking of my fridge, I will always be grateful to my parents. My two brothers were my childhood friends as well as relatives, and have been at the very least tolerant of their little sister. Although dedications are not the norm, I chose to dedicate this thesis to the younger of my two brothers, who died in my second year here. He was willing to slay my dragons (or at least beat up the bullies) and I wish he was still here to do it.

> *So Eden sank to grief,*
> *So dawn goes down to day.*
> *Nothing gold can stay.*
> Robert Frost

Abstract

Complex fluids are present in a multitude of forms: polymers, foods, paints, inks, biological materials, pharmaceuticals, cosmetics, etc. Many of these are suspensions, which have a particulate phase suspended in a solvent phase. This multiphase character gives a rich variety of behaviors, making suspensions interesting and useful materials but difficult to process. We investigate two different aspects of suspension behavior: instabilities in suspension flows and the use of microrheology in colloidal suspensions.

We look at two different mechanisms that generate instabilities and pattern formation in suspension flows. In the first, a jump in normal stresses at the interface between two fluids may lead to growing perturbations of the interface that ultimately give rise to migration of the particle phase into enriched regions. Fluids with a negative second normal stress difference, such as suspensions, can be unstable with respect to transverse or spanwise perturbations. The mechanism appears to be generic, although the details will depend on the specific system. The second mechanism may affect suspensions whose particle phase is not density-matched to the fluid. In this case, a flow can be unstable to spanwise perturbations of the particle phase when the shearing motion generates a density profile that increases with height. This is a Rayleigh–Taylor-like instability, due to having heavier material over light. As with the first instability, this mechanism may play an important role in pattern formation in multiphase flows.

The second aspect of suspension behavior we examine is the application of microrheology to colloidal suspensions. Microrheology has great promise for the study of soft, heterogeneous materials, but is not as well understood as traditional rheology. Most methods use tracer particles to investigate a medium, sometimes passively—tracking random motion (well established but restricted to the linear viscoelastic regime)—and more rarely actively—applying an external force to drive the tracers and access the medium's nonlinear response. Active microrheology is not well understood, and we study it by simulating a prototypical example, the motion of a particle due to an imposed force through a colloidal

suspension. The deformation of the microstructure results in resistance to the tracers motion. This system displays ‘force-thinning’, analogous to the ‘shear-thinning’ in a macrorheologically sheared suspension, but the comparison is not exact, and care needs to be taken in the use and application of microrheological results. Comparable length scales between the measurement device (the tracer) and the medium lead to interesting effects and distinctions between types of microrheological methods.

Contents

List of Figures

List of Tables

Chapter 1

Summary

Complex fluids surround us in a multitude of forms: from various plastics (polymers) to foods to paints and inks to biological materials to pharmaceuticals to cosmetics, etc. Many of these materials are suspensions, which are composed of a particulate phase suspended in a solvent phase. This multiphase character gives rise to a rich variety of behaviors, making suspensions among the most interesting and useful materials but also among the most difficult to process and understand. For suspensions, this includes shear-thinning and shear-thickening behavior, normal stress differences (which for polymers lead to the familiar example of 'rod-climbing' [1], but for suspensions lead to 'rod-dipping' [16]), and heterogeneous dispersion of the particle phase.

The work presented here investigates two aspects of suspension behavior: instabilities in suspension flows leading to pattern formation (Chapters 2 and 3, previously published [2, 3]) and the use of microrheology in colloidal suspensions (Chapter 4). The most familiar examples of instabilities in suspension flows are given by the demixing of granular flows based on such properties as particle size, shape and density [7], but also found in wetter flows with examples of fingering [9] and band formation in neutrally-buoyant [15] and non-neutrally buoyant suspensions [14]. Such phenomena and their causes are of great interest and concern, and are still often subject to debate. In regards to the second part of our study, microrheology is proving itself to be a useful tool in the study of materials at the small scale, but understanding of microrheology is lagging behind the technology.

In Chapter 2 an instability mechanism is shown to operate in complex, non-Newtonian fluids in which a jump in normal stresses occurs between two fluids. The study was prompted by recent experiments with viscous suspensions which showed particle segregation into bands along the axis of a rotating horizontal cylinder [15]. The particles were density-matched to the suspending fluid, but the pattern formation required a free surface in order to form. Similar behavior is found for granular materials in mixing drums [7, 6], although there the pattern formation has a more three-dimensional character. Consideration of the interfacial stress balance shows a simple link between a jump in the normal stresses across the interface and a perturbation to that interface, which suggests that such a jump in normal stresses may affect the stability of the system. A jump in the first normal stress difference has been shown to lead to longitudinal (flow-direction) instabilities in co-extruded polymers [8]. In an analogous way, a jump in the second normal stress difference is coupled to perturbations transverse to the flow, as we show here, and is particularly relevant to suspensions, which possess a negative second normal stress difference. We use a constitutive model for non-Brownian hard-sphere suspensions which produces a second normal stress difference in order to illustrate this instability mechanism for the cases of two-layer Couette and falling film flows of viscous suspensions. The mechanism appears to be generic, although the details will depend on the specific flow and the nature of the complex fluid, and a fluid which had significant normal stress differences could be unstable towards both longitudinal and transverse perturbations.

In Chapter 3 we study the gravity-driven flow of non-neutrally buoyant suspensions, and show such flows to be unstable to spanwise perturbations when the shearing motion generates a density profile that increases with height. A similar mechanism was shown to occur in granular flows down a slope [4], where it generated longitudinal vortices. The instability is simply due to having heavier material over light—a Rayleigh–Taylor-like instability. The initial particle migration and subsequent particle concentration is linked to the phenomenon of shear-induced migration, which can lead to particles concentrating in the regions of lowest shear rate when there is a shear gradient in the system. This leads to a particle concentration profile that is not homogenous across the flow, and which may have the density increasing with height if the particles are not neutrally-buoyant. We use the suspension-balance model [11, 12] which allows us to consider the particle phase separately and look at variations in particle concentration across the flow. We find that the wavelength of the fastest growing disturbance is on the order of the thickness of the suspension layer, with the problem affected by the angle of inclination of the layer relative to gravity, the relative density difference between the particles and the fluid, the ratio of the particle size to the thickness of the layer and the bulk volume fraction of particles. The instability is illustrated for a range of these parameters and shown to be most pronounced at intermediate values thereof. This instability mechanism may play an important role in pattern formation in multiphase flows, but we are not aware of any experiments involving heavy viscous suspension flows that are comparable.

In Chapter 4 we examine the application of microrheology to colloidal suspensions as examples of typical complex fluids. The improvement of imaging and computing technology given by the end of the last century has led to the expansion of rheology into a smaller dimension. Many materials that are of interest to researchers in both academia and industry are either naturally small-scaled, as in the case of cells and other such biomaterials, or present in small quantities, or are familiar materials that due to their microstructure are not amenable to bulk measurements. Microrheology, rheology at the microscopic scale, is starting to fill these needs and has great promise for the study of soft, heterogeneous materials, but unfortunately it is not as well understood as traditional macroscopic rheology and is therefore limited in its use. Most microrheology methods use tracer particles to investigate a medium, sometimes passively—tracking the random motion of the tracers (well established but restricted to the linear viscoelastic regime)—and more rarely actively—applying an external force to drive the tracers and thus accessing the medium's nonlinear response [10]. Traditional rheology studies both linear and nonlinear behavior, but understanding of active microrheology, which would bring parity between micro and macrorheology, is still lacking.

The purpose of this work has been to numerically study the 'active' system and its transition from the linear to the nonlinear regime. We do this by choosing a prototypical example, the motion of a particle due to an imposed force (or velocity) through a colloidal suspension. Colloids are ubiquitous examples of complex fluids and have been well-studied by traditional rheology both experimentally and theoretically as well as by active microrheology [5], and therefore allow us to compare our microrheological results to the results of macrorheology. We find that this system displays 'shear-thinning', analogous to the macrorheological sheared suspension, but the comparison is not exact, and care needs to be taken in the use and application of microrheological results. Comparable length scales between the measurement device (the tracer) and the medium lead to interesting effects and distinctions between types of microrheological methods, such as differences between applying a constant force versus a constant velocity to the tracer. The simulations compare well to the simple dilute theory results [13] but also allow us to see high-concentration effects such as yielding behavior, which cannot be captured by the simple theory. We also look at the effect of tracers upon each other—neighboring tracers may attract or repel each other depending on their relative separation (which may result in an excluded volume effect for the surrounding particles).

Bibliography

[1] R.B. Bird, R.C. Armstrong, and O. Hassager. *Dynamics of Polymeric Liquids*, volume 1. John Wiley & Sons, New York, 1977.

[2] J.F. Brady and I.C. Carpen. Second normal stress jump instability in non-Newtonian fluids. *J. Non-Newtonian Fluid Mech.*, 102:219–232, 1997.

[3] I.C. Carpen and J.F. Brady. Gravitational instability in suspension flow. *J. Fluid Mech.*, 472:201–210, 2002.

[4] Y. Forterre and O. Pouliquen. Longitudinal vortices in granular flows. *Phys. Rev. Lett.*, 86:5886–5889, 2001.

[5] P. Habdas, D. Schaar, A.C. Levitt, and E.R. Weeks. Forced motion of a probe particle near the colloidal glass transition. *Europhys. Lett.*, 67:477–483, 2004.

[6] K.M. Hill, A. Caprihan, and J. Kakalios. Bulk segregation in a rotated granular material measured by magnetic resonance imaging. *Phys. Rev. Lett.*, 78:50–53, 1997.

[7] K.M. Hill and J. Kakalios. Reversible axial segregation of rotating granular material. *Phys. Rev. E*, 52:4393–4400, 1995.

[8] E.J. Hinch, O.J. Harris, and J.M. Rallison. The instability mechanism for two elastic liquids being co-extruded. *J. Non-Newtonian Fluid Mech.*, 43:311–324, 1992.

[9] A. Lange, M. Schröter, M.A. Scherer, A. Engel, and I. Rehberg. Fingering instability in a water-sand mixture. *Eur. Phys. J. B*, 4:475–484, 1998.

[10] F.C. MacKintosh and C.F. Schmidt. Microrheology. *Curr. Op. Colloid Interf. Sci.*, 4:300–307, 1999.

[11] J.F. Morris and J.F. Brady. Pressure-driven flow of a suspension: buoyancy effects. *Int. J. Multiphase Flow*, 24:105–130, 1998.

[12] P.R. Nott and J.F. Brady. Pressure-driven flow of suspensions: simulation and theory. *J. Fluid Mech.*, 275:157–199, 1994.

[13] T.M. Squires and J.F. Brady. A simple paradigm for active and nonlinear microrheology. Submitted to Phys. Fluids.

[14] P.J. Thomas, G.D. Riddell, S. Kooner, and G.P. King. Fine structure of granular banding in two-phase rimming flow. *Phys. Fluids*, 13:2720–2723, 2001.

[15] M. Tirumkudulu, A. Mileo, and A. Acrivos. Particle segregation in monodisperse sheared suspensions in a partially filled rotating horizontal cylinder. *Phys. Fluids*, 12:1615–1618, 2000.

[16] I.E. Zarraga, D.A. Hill, and D.T. Leighton. The characterization of the total stress of concentrated suspensions of noncolloidal spheres in Newtonian fluids. *J. Rheol.*, 44:185–220, 2000.

Chapter 2

Second Normal Stress Difference Jump Instability in Suspension Flow

2.1 Introduction

Non-Newtonian liquids, such as polymer solutions and other so-called complex fluids, exhibit an interesting array of flow phenomena due to the presence of normal stress differences. A familiar example is 'rod-climbing', where a fluid climbs up a rotating rod due to hoop stresses generated along the curved fluid streamlines [2]. Another quite dramatic example of normal stress effects are the purely elastic flow instabilities that can arise, for example, in Taylor-Couette flow [13].

There have been a number of recent experiments in granular materials and viscous suspensions in which a flow becomes unstable to transverse or spanwise disturbances. In granular materials particles of different size or density have been observed to segregate along the axis of a drum when it is rotated horizontally [8, 7]. In a similar experiment, a viscous suspension of neutrally buoyant spherical particles segregated along the axis of a rotating horizontal cylinder [15]. In both of these situations a free surface separates the non-Newtonian granular or suspension material from a Newtonian fluid, air.

At a flat interface between two flowing materials the shear and normal stresses, say σ_{yx}, σ_{yz} and σ_{yy} (see Figure 2.1), must be continuous, but the normal stresses in directions perpendicular to the interface—in the flow and transverse or spanwise directions (σ_{xx} and σ_{zz})—need not be continuous, and in general will not be if one or both of the materials are rheologically complex and possess normal stress differences. This is a perfectly acceptable mechanical balance for a flat interface. If the interface is perturbed, however, the mismatch or jump in normal stresses of the undisturbed flow couples to the perturbed interface and creates a traction that can act to destabilize the interface (*cf.* Figure 2.1). The

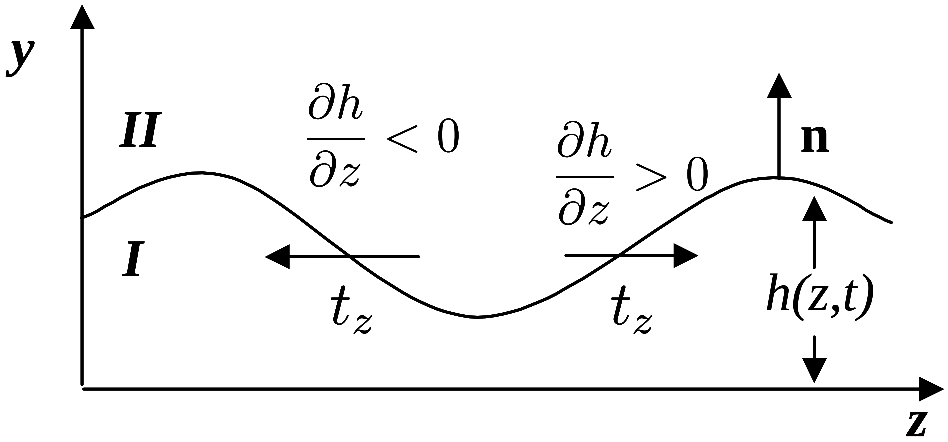

Figure 2.1: Transverse perturbation to the interface: a positive second normal stress jump across the interface gives rise to a traction t_z that acts to amplify the disturbance.

first normal stress difference governs the behavior due to perturbations in the flow direction [9], while transverse perturbations are governed by the second normal stress difference and will be the focus of this study.

As we show below, the basic mechanism driving the instability—the jump in normal stresses—is generic and therefore the general conclusions reached should be applicable to a wide range of materials and conditions, although the details depend both on the flow type and on the constitutive law governing the non-Newtonian material behavior. Our interest here is in viscous suspension flows and we use a simple model for the rheological behavior that captures the experimental observations. In particular, viscous suspensions have relatively large *negative* second normal stress differences, which is just the condition needed to see the instability. We consider two simple flows—two-layer Couette flow and flow down a vertical plane—that allow analytical solutions to be obtained. The only other related work we have found is that of Renardy & Renardy [11] on the stability of a Giesekus fluid to a jump in second normal stress differences.

2.2 Stability analysis

Consider the flow of two immiscible fluids (denoted I and II) in the x-direction as illustrated in Figure 2.2 for the two-layer Couette flow or Figure 2.6 for the falling film problem. The interface separating the two layers is perturbed in the transverse direction as illustrated in Figure 2.1. The interface is located at $y = h(z,t)$, and the interfacial conditions on stress are

$$\text{x-mom:} \qquad t_x = \sigma_{yx}^{II} - \sigma_{yx}^{I} - \frac{\partial h}{\partial z}(\sigma_{zx}^{II} - \sigma_{zx}^{I}) = 0, \tag{2.1a}$$

$$\text{y-mom:} \qquad t_y = \sigma_{yy}^{II} - \sigma_{yy}^{I} - \frac{\partial h}{\partial z}(\sigma_{zy}^{II} - \sigma_{zy}^{I}) = \gamma(\nabla\cdot\boldsymbol{n}), \tag{2.1b}$$

$$\text{z-mom:} \qquad t_z = \sigma_{yz}^{II} - \sigma_{yz}^{I} - \frac{\partial h}{\partial z}(\sigma_{zz}^{II} - \sigma_{zz}^{I}) = -\frac{\partial h}{\partial z}\gamma(\nabla\cdot\boldsymbol{n}), \tag{2.1c}$$

where $\boldsymbol{t}$ is the traction vector, $\boldsymbol{n}$ is the normal from fluid I to II and γ is the coefficient of interfacial tension.

From the continuity of the normal stresses at the undisturbed interface the traction transverse to the interface to leading order in $\partial h/\partial z$ can be written as

$$t_z = \sigma_{yz}^{II} - \sigma_{yz}^{I} + (N_2^{II} - N_2^{I})\frac{\partial h}{\partial z} = 0, \tag{2.2}$$

where the second normal stress difference N_2 is

$$N_2 = \sigma_{yy} - \sigma_{zz}.$$

A positive second normal stress difference jump, $\Delta N_2 = N_2^{II} - N_2^{I} > 0$, exerts a traction on the interface that acts to enhance the perturbation as illustrated in Figure 2.1. Since most non-Newtonian fluids have *negative* second normal stress differences, this means that fluid I should be 'more non-Newtonian' than fluid II, which is the case for a Newtonian fluid over a non-Newtonian fluid in the two-layer Couette flow, or for the falling film problem in Figure 2.6 with air as fluid II. The traction due to the jump in the second normal stress difference is balanced by the perturbation to the shear stresses, and so whether or not the flow is unstable depends not only on the magnitude of N_2—the nature of the non-Newtonian material—but also on the type of flow and the geometry.

An analogous situation arises for perturbations in the flow direction—along x—and there is a similar traction from a jump in first normal stress differences:

$$-(N_1^{II} - N_1^{I})\frac{\partial h}{\partial x},$$

where the first normal stress difference N_1 is

$$N_1 = \sigma_{xx} - \sigma_{yy}.$$

It is now a *positive* N_1 that determines instability.

Most polymeric liquids have a positive N_1, and a much smaller negative N_2 [2], and thus may be subject to longitudinal instabilities due to a jump in N_1. The sign of N_2 would also allow transverse instabilities but these would most likely be overwhelmed by any N_1-driven instability. By contrast, viscous suspensions (specifically at high Péclet number where Brownian motion is not important [1, 6, 16]) and many granular materials [4] have negative first and second normal stress differences both of which are of the same magnitude. Thus, flows of these materials will be stable to longitudinal perturbations, but may be unstable to transverse perturbations due to a jump in N_2.

Our interest is in viscous suspension flows and we will use a simple microstructurally-based constitutive model for non-Brownian suspensions at low particle Reynolds numbers that follows from the work of Brady & Morris [3] and is in fair agreement with Stokesian Dynamics simulations for simple shear [6, 14] and planar extensional [12] flows and with laboratory experiment [16]. The stress is composed of a Newtonian fluid part and a contribution from the suspended particles:

$$\boldsymbol{\sigma} = -p\,\boldsymbol{I} + 2\,\eta\,\boldsymbol{e} - \eta_p\dot{\gamma}^{\circ} \oint_{\gamma_r<0} \hat{\boldsymbol{r}}\hat{\boldsymbol{r}}(\gamma_r)^2 d\Omega, \tag{2.3}$$

where the pressure in the suspending fluid is p, its viscosity is η, the rate of strain of the suspension is $\boldsymbol{e}$, and the integral takes into account the non-Newtonian character of the suspension, in particular the deformation of the microstructure due to shear. The 'particle' viscosity η_p is a function of the volume fraction ϕ of suspended particles, with $\eta_p(\phi) \sim \eta\phi^2$ as $\phi \to 0$ and diverging as maximum packing is approached. The integral in (2.3) is over the surface of a sphere (with solid angle $d\Omega$) and comes from a consideration of the stress due to a pair of contacting particles in shear flow [3, 6, 14]. As shown by Morris and Brady [3], the dominant stresses come from particle pairs along the compressive axis of the flow, and thus the range of integration is restricted to lie along this axis, $\gamma_r < 0$, where

$$\gamma_r = \hat{\boldsymbol{r}} \cdot \hat{\boldsymbol{e}} \cdot \hat{\boldsymbol{r}},$$

and $\hat{\boldsymbol{r}}$ is a unit vector on the surface of the sphere. Here, $\hat{\boldsymbol{e}}$ has been made nondimensional by the magnitude of the shearing motion $\dot{\gamma}^\circ$.

In simple shear flow, $\dot{\gamma}^\circ$ is a constant, $\partial u_x^\circ/\partial y$, where the flow direction is x, the velocity-gradient direction y and the vorticity direction z, and the first and second normal stress differences for the model are

$$N_1 = -\eta_p\dot{\gamma}^\circ \int\limits_{\frac{\pi}{2},\frac{3\pi}{2}}^{\pi,2\pi} \int\limits_{0}^{\pi} (\hat{r}_x^2 - \hat{r}_y^2)\hat{r}_x^2\hat{r}_y^2 \sin\theta \; d\theta \; d\varphi = 0,$$

$$N_2 = -\eta_p\dot{\gamma}^\circ \int\limits_{\frac{\pi}{2},\frac{3\pi}{2}}^{\pi,2\pi} \int\limits_{0}^{\pi} (\hat{r}_x^2 - \hat{r}_z^2)\hat{r}_x^2\hat{r}_y^2 \sin\theta \; d\theta \; d\varphi = -\frac{4\pi}{105}\eta_p\dot{\gamma}^\circ.$$

The model gives $N_1 = 0$ because of the assumed symmetry about the compressive axis. The actual particle pair distribution is not symmetric about this axis [1], which results in a small negative N_1. Since our focus is on N_2-driven instability this limitation of the model is of no consequence. Note that the non-Newtonian stress may vary from point to point in a flow either because the magnitude of the shear rate varies, $\dot{\gamma}^\circ$, or because the local orientation of the compressive axis varies, γ_r.

In an actual experiment the particle volume fraction may not remain constant as a flow or

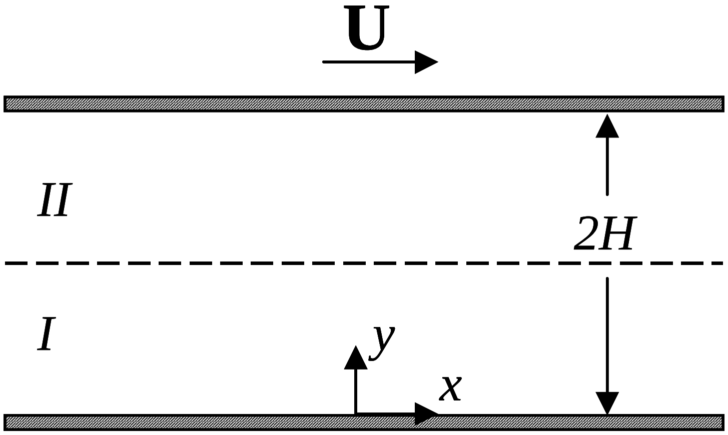

Figure 2.2: Planar Couette flow of two immiscible fluids in a gap of height $2H$, with the interface located at $y = h(z,t) \approx H$. The top plate moves with a velocity $\boldsymbol{U}$ while the bottom plate remains stationary.

instability develops. Particle migration and concentration inhomogeneities can be modeled by writing separate mass and momentum balances for the suspension as a whole (to which (2.3) applies) and for the particle phase [5, 10]. However, our focus is on the basic character of the instability, and therefore we shall consider a simpler model in which we treat ϕ as constant. This allows for an analytical solution and should capture the instability qualitatively, if perhaps not quantitatively. For a first study it would seem prudent to use as simple a model as possible.

2.3 Model flow problems

We consider two suspension flow problems that illustrate the instability. The first problem is a two-layer Couette flow in which a jump in second normal stress differences couples with a jump in viscosity between the two fluids to drive the instability. The second problem is the gravity-driven flow of a film down a vertical wall.

2.3.1 Two-layer Couette flow

The two-layer Couette flow is shown in Figure 2.2. For simplicity each fluid occupies half the gap between the moving and stationary plates and the two fluids are described by the constitutive equation (2.3) with different shear and particle viscosities. Each fluid is incompressible and the Reynolds number is taken to be small, and therefore the mass and momentum balances are

$$\nabla\cdot\boldsymbol{u} = 0\ , \quad \nabla\cdot\boldsymbol{\sigma} = 0\,,$$

where $\boldsymbol{u}$ is the suspension velocity. The fluids satisfy the no-slip condition at the two plates, and continuity of velocity and the interfacial stress conditions (2.1a-2.1c) at the interface between the two fluids $y = h(z,t)$. In addition, we have the kinematic condition at the interface

$$\frac{\partial h}{\partial t} = v - w\frac{\partial h}{\partial z}\,,$$

where (u, v, w) are the (x, y, z) components of the suspension velocity. Since inertia is not important, the only time dependence is in the kinematic condition.

The base state for fully-developed flow with a flat interface is simply

$$\begin{aligned} u^{\circ,I}(y) &= U\left(\frac{\eta^{II}_{eff}}{\eta^{I}_{eff} + \eta^{II}_{eff}}\right)\left(\frac{y}{H}\right), \\ u^{\circ,II}(y) &= U\left(1 + \frac{\eta^{I}_{eff}}{\eta^{I}_{eff} + \eta^{II}_{eff}}\left(\frac{y}{H} - 2\right)\right), \\ [v^\circ, w^\circ]^{I,II} &= 0, \end{aligned}$$

where the superscripts I and II denote the two fluids. The base state stresses can be found from the velocities and the constitutive equation (2.3). For example, η^{I}_{eff} is

$$\eta^{I}_{eff} = \eta^{I} + \frac{16}{105}\eta^{I}_{p}.$$

We perform a standard linear stability analysis with $\boldsymbol{u} = \boldsymbol{u}^\circ + \boldsymbol{u}'$ and $h(z,t) = H + \epsilon H\, e^{ikz+st}$, where s is the growth rate, k the wave number and ϵ the small amplitude. Writing $\boldsymbol{u}' =$

$\epsilon\,(u(y), v(y), w(y))\,e^{ikz+st}$, we find for u and v, after rendering y dimensionless by H,

$$u'' - \frac{(kH)^2}{1+\dfrac{16}{105}\dfrac{\eta_p}{\eta_{eff}}}\,u = \frac{\dfrac{4\,\pi}{105}\dfrac{\eta_p}{\eta_{eff}}}{1+\dfrac{16}{105}\dfrac{\eta_p}{\eta_{eff}}}(v'' - (kH)^2 v), \tag{2.4a}$$

$$v^{(4)} - \left(2 - \frac{8}{105}\frac{\eta_p}{\eta_{eff}}\right)(kH)^2 v'' + (kH)^4 v = -\frac{4\,\pi}{105}\frac{\eta_p}{\eta_{eff}}(kH)^2(u'' - (kH)^2 u). \tag{2.4b}$$

Equation (4) applies to both regions I and II upon replacing the dimensionless y with $y_{new} = y - 2$ for region II and u by $u\;Sgn(U)$. The perturbation satisfies no slip at $y = y_{new} = 0$:

$$u(0) = v(0) = v'(0) = 0, \tag{2.5}$$

and the continuity of velocity and the stress balances at the interface ($y = 1$, $y_{new} = -1$) become

$$\Delta v = 0, \tag{2.6a}$$

$$\Delta v' = 0, \tag{2.6b}$$

$$\Delta u = -|U|\left(\frac{\eta^{I}_{eff} - \eta^{II}_{eff}}{\eta^{I}_{eff} + \eta^{II}_{eff}}\right), \tag{2.6c}$$

$$\Delta\left[\eta_{eff}\left(\left(1 + \frac{16}{105}\frac{\eta_p}{\eta_{eff}}\right)u' - \left(\frac{8\,\pi}{105}\frac{\eta_p}{\eta_{eff}}\right)v'\right)\right] = 0, \tag{2.6d}$$

$$\Delta[-\eta_{eff}v''' + \left(3\eta_{eff} - \frac{8}{105}\eta_p\right)(kH)^2 v' - \frac{4\,\pi}{105}\eta_p(kH)^2 u'] = (kH)^4\gamma, \tag{2.6e}$$

$$\Delta\left[\eta_{eff}(v'' + (kH)^2 v) - \frac{4\,\pi}{105}\eta_p(kH)^2 u\right] = -(kH)^2 H \Delta N_2^{\circ}, \tag{2.6f}$$

where $\Delta = II - I$ and $\Delta N_2^{\circ} = N_2^{\circ,II} - N_2^{\circ,I} = \frac{4\pi}{105}(\eta_p^{I}\dot{\gamma}^{\circ,I} - \eta_p^{II}\dot{\gamma}^{\circ,II}) = \frac{4\pi}{105}\frac{|U|}{H}(\eta_p^{I}\eta^{II}_{eff} - \eta_p^{II}\eta^{I}_{eff})/(\eta^{I}_{eff} + \eta^{II}_{eff})$. The growth rate, from a symmetric form of the kinematic condition, is

$$s = \left[\frac{v(H)}{H}\right]^{I,II}.$$

Note that in obtaining the disturbance equations, the perturbation to both the amplitude of the shearing motion, $\boldsymbol{e} \to \boldsymbol{e}^\circ + \boldsymbol{e}'$, and the principal axis determining the deformed microstructure in the limits of integration in (2.3), $\gamma_r \to \gamma_r^\circ + \gamma_r'$, have been included.

An analytical solution is possible, with *Mathematica* to aid in the algebra, but the resulting formulae are too long to record here. Equation (2.6c) points to the fact that the stability is dependent on the viscosity contrast between the two fluids. Indeed, a viscosity contrast is needed in order for the system to be unstable. This is most clearly seen at long wavelengths. At small kH the perturbation velocity v is $O(kH)^2$ and the growth rate has the asymptotic form

$$s \sim -\frac{1}{2}(kH)^2\, \Delta N_2^\circ\, \Delta\eta_{eff}\, \frac{1}{[(\eta_{eff}^I)^2 + (\eta_{eff}^{II})^2 + 14\eta_{eff}^I\eta_{eff}^{II}]}. \tag{2.7}$$

For $\Delta N_2^\circ > 0$ then $\Delta\eta_{eff} < 0$ in order to have a positive growth rate. That is, if the top (II) fluid is Newtonian, then it must have a lower viscosity than the non-Newtonian fluid on the bottom (I). (Recall that $N_2 < 0$ for most materials.) The viscosity contrast is necessary so that the flow driven by the jump in shear stress (2.2) acts to amplify the disturbance.

Figure 2.3 shows the z-component of the disturbance velocity (w) due to ΔN_2° only for the case of fluid II a Newtonian fluid for three different viscosity ratios. All three profiles show that at the interface w is in the direction of the traction force (*cf.* Figure 2.1). However, conservation of volume requires that the net flow of fluid at any z-location must be zero, and therefore there is a 'return' flow in each of the layers, with a larger return flow in the fluid with the smaller viscosity. (If the layers were of different thickness, then the criterion would involve the ratio η/H for each layer.) When $\Delta\eta_{eff} = 0$ the return flow is equal in both layers and the interface is marginally stable. When fluid II has a lower viscosity, the return flow is larger and this drives more fluid into the trough in Figure 2.1, which amplifies the perturbation and the interface is unstable. The opposite occurs if fluid I has a lower viscosity. This effect of the return flow is similar to the behavior seen in the N_1-driven instabilities considered in [9]. Note that the growth rate in (2.7) is symmetric with interchange of the two fluids ($I \leftrightarrow II$) as it must be.

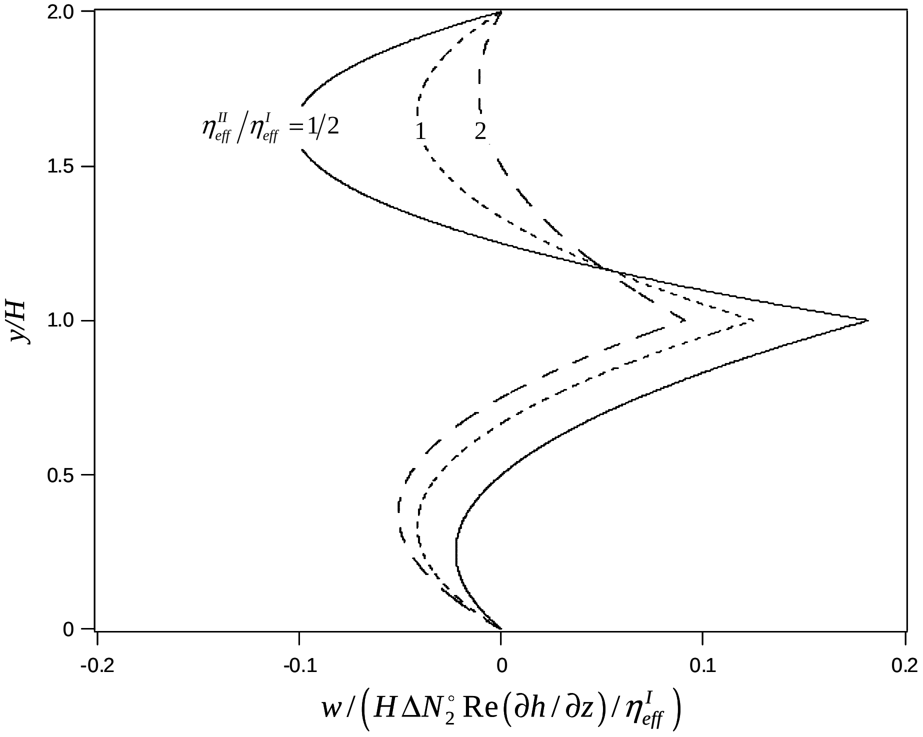

Figure 2.3: The z-component of the disturbance velocity w due to ΔN_2° for fluid II a Newtonian fluid for three different viscosity ratios. The strength of the 'return' flow in each layer acts either to amplify or dampen the perturbation shown in Figure 2.1.

The jump in viscosity also drives a perturbation to the longitudinal flow from (2.6c) which is $O(|U|)$. This flow perturbs the shear rate in each layer and thus generates a normal stress difference of $O(kH)^2$ in the interface balances. Thus, there is also an $O(kH)^2$ contribution to s that is proportional to $|U|$:

$$\begin{aligned} s \sim\ & \frac{2\pi}{105}(kH)^2\frac{|U|}{H}\Delta\eta_{eff}\frac{1}{(\eta^I_{eff}+\eta^{II}_{eff})} \\ \times\ & \frac{175\eta^I_{eff}\eta^{II}_{eff}\Delta\eta_p + 32\eta^I_p\eta^{II}_p\Delta\eta_{eff} - 35[(\eta^I_{eff})^2\eta^{II}_p - (\eta^{II}_{eff})^2\eta^I_p]}{[(\eta^I_{eff})^2+(\eta^{II}_{eff})^2+14\eta^I_{eff}\eta^{II}_{eff}][16(\eta^I_p+\eta^{II}_p)+105(\eta^I_{eff}+\eta^{II}_{eff})]}, \end{aligned} \tag{2.8}$$

where $\Delta\eta_p = \eta_p^{II} - \eta_p^I$. The growth rate is proportional to $|U|$ as the actual direction of motion of the boundaries does not change the sign of the normal stress differences. When fluid II is a Newtonian fluid with a lower viscosity than fluid I ($\Delta\eta_{eff} < 0$), the decreased shear rate in region I decreases the normal

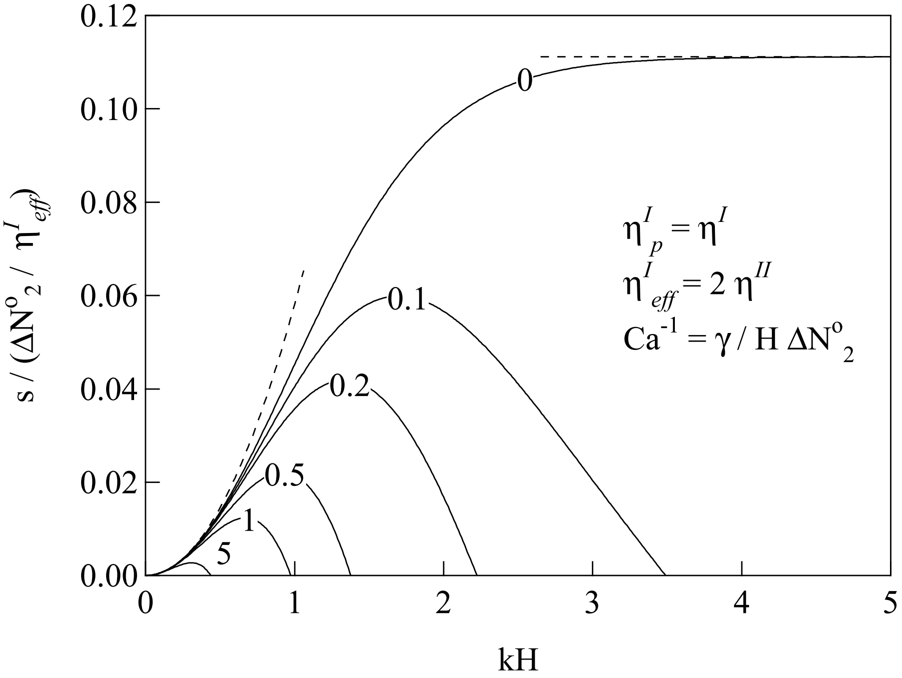

Figure 2.4: Couette results with $\eta_p^I = \eta^I$ and $\eta_{eff}^I = 2\eta^{II}$: the inverse Capillary number (Ca^{-1}), which compares the strength of surface tension to that of ΔN_2°, is varied from 0 to 5. The asymptotic limits for low and high kH are shown as dashed curves for the case of zero surface tension ($Ca^{-1} = 0$).

stress below a trough (*cf.* Figure 2.1) which destabilizes the interface. Note that (2.8) is symmetric upon interchange of the two fluids.

Finally, surface tension stabilizes the interface, and the leading order term is $O(kH)^4$:

$$s \sim -\frac{\gamma}{3H}\,(kH)^4\,\frac{\eta_{eff}^I + \eta_{eff}^{II}}{[(\eta_{eff}^I)^2 + (\eta_{eff}^{II})^2 + 14\eta_{eff}^I\eta_{eff}^{II}]}. \tag{2.9}$$

As mentioned before, the general formulae are too long to write out, and so in Figure 2.4 we show the growth rate for fluid II a Newtonian fluid with viscosity half that of the non-Newtonian suspension. The various curves correspond to different values of the 'N_2-Capillary' number $Ca = H\Delta N_2^\circ/\gamma$. In the absence of surface tension the layer is unstable at all wavenumbers with the maximum growth rate occurring as $kH \to \infty$. The effect of surface tension is to stabilize short wavelength disturbances, to reduce the growth rate and to shift the maximum growth rate to smaller wavenumbers. The growth rate

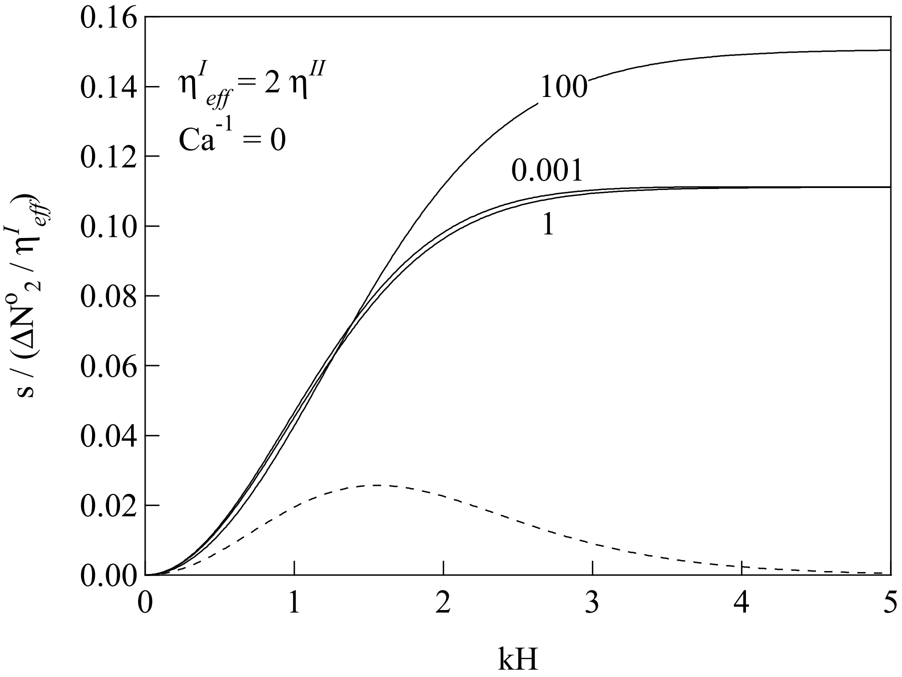

Figure 2.5: Couette results for various ratios of η_p^I to η^I for $Ca^{-1} = 0$ and $\eta^I_{eff} = 2\eta^{II}$. The range of η_p/η varies from 0.001 to 100. The apparent nonmonotonicity for small η_p^I/η^I arises because ΔN_2° is proportional to η_p^I. The dashed curve corresponds to a 'Newtonian' layer I—ΔN_2° is presumed nonzero, but η_p^I is set to zero for the perturbed flow.

is proportional to the only timescale, the shear rate U/H. At high wavenumber the growth rate has the asymptotic form

$$s \sim 0.000205\left(\frac{\Delta N_2^\circ}{\eta^I_{eff}}\right) + 0.111\left(\frac{4\pi}{105}\frac{\eta_p^I\eta^{II}_{eff}}{\eta^I_{eff}\left(\eta^I_{eff}+\eta^{II}_{eff}\right)}\right)\frac{|U|}{H} - 0.337\left(\frac{\gamma}{H\eta^I_{eff}}\right)(kH),\;\; kH \to \infty,$$

for the case of $\eta_p^I = \eta^I$ and $\eta^I_{eff} = 2\eta^{II}_{eff}$, although the dependence on kH would remain unchanged for other values of η_p^I. The results in Figure 2.4 are for the particle viscosity equal to the fluid viscosity, $\eta_p^I = \eta^I$. In Figure 2.5 we show the effect of varying η_p^I/η^I on the growth rate in the absence of surface tension ($Ca^{-1} = 0$). Changing η_p^I/η^I has a quantitative, but not qualitative, effect on the behavior. Note that both ΔN_2° and η^I_{eff} also change with η_p^I/η^I. The normal stress jump is proportional to η_p^I and, for large η_p^I (high volume fractions ϕ) $\eta^I_{eff} \approx \eta_p^I$, so that $\Delta N_2^\circ/\eta^I_{eff}$ and the growth rate s are independent of

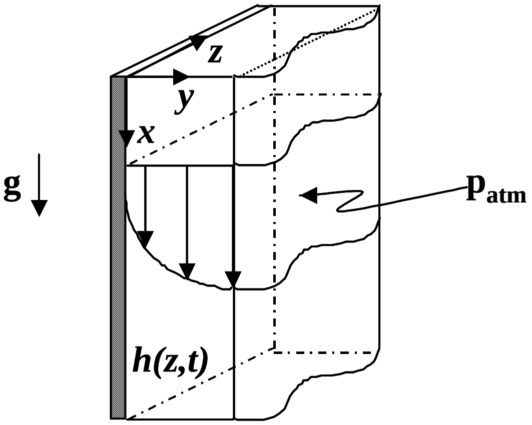

Figure 2.6: The falling film problem: flow down a vertical wall with a non–Newtonian fluid-air interface located at $y = h(z,t) \approx H$.

η^I/η^I_{eff}. At the other extreme as $\eta^I_p/\eta^I \to 0$, ΔN_2° vanishes but $\eta^I_{eff} \sim \eta$. In Figure 2.5 we have scaled ΔN_2° by η^I_{eff}, which accounts for the apparent nonmonotonic behavior as $\eta^I_p/\eta^I \to 0$. Also shown in Figure 2.5 is a dashed curve corresponding to a 'Newtonian' fluid—that is, we set $\eta^I_p = 0$ everywhere in equations (2.6a -2.6f) but keep ΔN_2° fixed as a forcing on the right hand side of (2.6f). This shows that the details of the constitutive law are not important; it is a nonzero ΔN_2° that destabilizes the system.

2.3.2 Falling film

The falling film problem is illustrated in Figure 2.6. Fluid II will be air with a constant pressure p_{atm}. The mass balance is as in the Couette flow, but the momentum balance has gravity as the driving force

$$\nabla \cdot \boldsymbol{\sigma} = -\rho \boldsymbol{g}\,,$$

where ρ the suspension density and $\boldsymbol{g}$ is the acceleration of gravity. The suspension is assumed to satisfy the no-slip boundary condition at the solid wall,

$$\boldsymbol{u} = 0 \quad @ \quad y = 0,$$

and the interfacial conditions (2.1a-2.1c) apply at the suspension-air interface $y = h(z,t)$.

The base state for steady, fully-developed flow with a flat interface $y = H$ is simply

$$u^\circ = \frac{\rho g H^2}{\eta_{eff}} \left(\frac{y}{H} - \frac{1}{2} \left(\frac{y}{H} \right)^2 \right) \;,\; v^\circ = w^\circ = 0,$$

$$\sigma^\circ_{yy} = -p_{atm} \,,$$

where η_{eff} from (2.3) is as before $\eta_{eff} = \eta + \frac{16}{105}\eta_p$, and we have dropped the unnecessary superscripts I and II labeling the two fluids. The normal stresses σ^0_{xx} and σ^0_{zz} can be found from the base solution and the constitutive equation.

The stability analysis proceeds as before, with equations (2.4a-2.4b) governing the perturbation velocities, subject to no slip at the wall

$$u(0) = v(0) = v'(0) = 0, \tag{2.10}$$

and at the undisturbed interface $y = 1$:

$$\left(1 + \frac{16}{105}\frac{\eta_p}{\eta_{eff}}\right) u' - \frac{8\,\pi}{105}\frac{\eta_p}{\eta_{eff}} v' = \frac{\rho g H^2}{\eta_{eff}}, \tag{2.11a}$$

$$v''' - \left(3 - \frac{8}{105}\frac{\eta_p}{\eta_{eff}}\right)(kH)^2 v' + \frac{4\,\pi}{105}\frac{\eta_p}{\eta_{eff}}(kH)^2 u' = (kH)^4 \frac{\gamma}{\eta_{eff}}, \tag{2.11b}$$

$$v'' + (kH)^2 v - \frac{4\,\pi}{105}\frac{\eta_p}{\eta_{eff}}(kH)^2 u = (kH)^2 \frac{H \Delta N_2^\circ}{\eta_{eff}}, \tag{2.11c}$$

where $\Delta N_2^\circ = -N_2^\circ = -(\sigma^\circ_{yy} - \sigma^\circ_{zz})$. Finally, the growth rate is determined from the kinematic condition

$$s = v(H)/H \,.$$

An analytical solution to the disturbance problem is again possible, with *Mathematica* to aid in the algebra, but the resulting formulae are too long to record here. There are four separate effects influencing the stability of the system. The ΔN_2° forcing on the right-hand side (RHS) of (2.11c) is the primary mechanism of the traction coupling to the perturbed interface as illustrated in Figure 2.1 and is destabilizing for $\Delta N_2^\circ > 0$. On the LHS of (2.11b), which is the perturbed normal stress balance at the interface, the term involving u' arises from the extra 'pressure' associated with the enhanced flow under a crest in the perturbed interface. The driving force for the flow is gravity, as seen on the RHS of (2.11a), and under a crest there is more mass and therefore a larger flow (and shear) rate, which in turn implies a larger normal stress from the constitutive equation. This extra stress is destabilizing. Third, the extra mass under a crest drives an extra longitudinal flow (u), and the stresses generated by this flow from the RHS of (2.4b) act against the perturbation and stabilize the interface. Finally, surface tension on the RHS of (2.11b) stabilizes short wavelength (high k) disturbances.

In order to determine the stability, we need to evaluate N_2° from the base state, and this is where our simplified constitutive model that neglects variation in volume fraction breaks down. At the free surface, the base state has zero shear rate, which would give a zero N_2°. However, a zero N_2° is not the correct behavior for suspension flows. A proper model for viscous suspensions has momentum balances for both the suspension as a whole and for the particles as a phase, with stress tensors $\boldsymbol{\sigma}$ and $\boldsymbol{\sigma}^p$, respectively. In each phase the $y-$momentum balance requires both σ_{yy} and σ_{yy}^p to be constant across the film. The suspension stress is given by the constitutive equation (2.3), while the particle-phase stress is simply the integral term in (2.3). Clearly, it is not possible to have a constant σ_{yy}^p and a zero shear rate at the interface. What happens in actual suspension flows is that there is particle migration to the free surface and so the assumption of a constant volume fraction is not correct. Also, the simple constitutive model with the normal stress proportional to the local shear rate is not valid when the shear rate vanishes and a nonlocal constitutive model is needed [10]. One could carry out the stability analysis with a more complete, nonlocal, constitutive model and also allow the volume fraction to vary spatially, but then an analytical solution is not possible. In order to illustrate more clearly the instability we have kept the simple model (2.3) and have evaluated N_2° at the average shear rate across the layer:

$$\langle N_2^\circ \rangle = -\frac{2\pi}{105}\frac{\eta_p}{\eta_{eff}}\rho g H.$$

This will only affect the quantitative, and not the qualitative, behavior. Indeed, the two-layer Couette

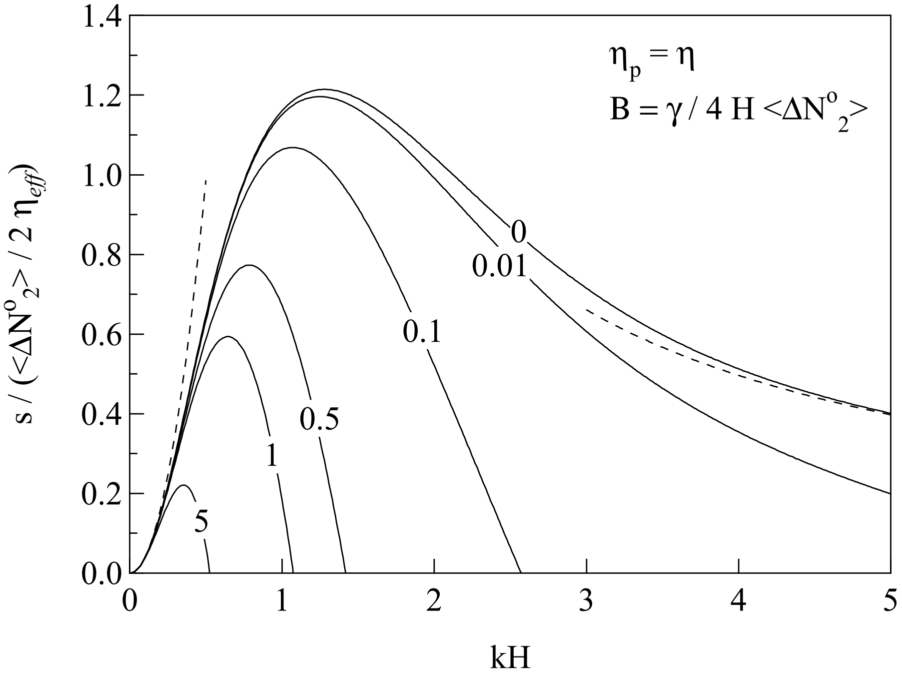

Figure 2.7: Falling film results with $\eta_p = \eta$: the N_2-Bond number B, which compares the strength of surface tension to that of the gravity-based ΔN_2°, is varied from 0 to 5. The asymptotic limits for low and high kH are shown as dashed curves for the case of zero surface tension ($B = 0$).

flow shows the same characteristic behavior as the falling film problem but does not have the problem of a vanishing shear rate and the simple constitutive model (2.3) holds throughout the flow. The stability analysis with the more complete constitutive model allowing for particle migration will be addressed in a future study.

Figure 2.7 shows the total growth rate, non-dimensionalized by the characteristic second normal stress difference as a function of dimensionless wave number for various values of the 'N_2-Bond' number $B = \gamma/(4H\,\langle \Delta N_2^\circ \rangle) = \gamma/(8\pi\eta_p\rho g H^2/105\eta_{eff})$. In the absence of surface tension, $B = 0$, the falling film is unstable at all wavelengths, with a maximum growth rate of 1.21 at a dimensionless wavenumber of $kH = 1.28$. Surface tension stabilizes short wavelength disturbances, which shifts the maximum growth rate to smaller kH and reduces its magnitude. Note that the growth rate is proportional to the shear rate, $\rho g H/\eta_{eff}$, as this is the only timescale for viscous suspensions.

In the limits of small and high wavenumbers, the dimensionless growth rate has the asymp-

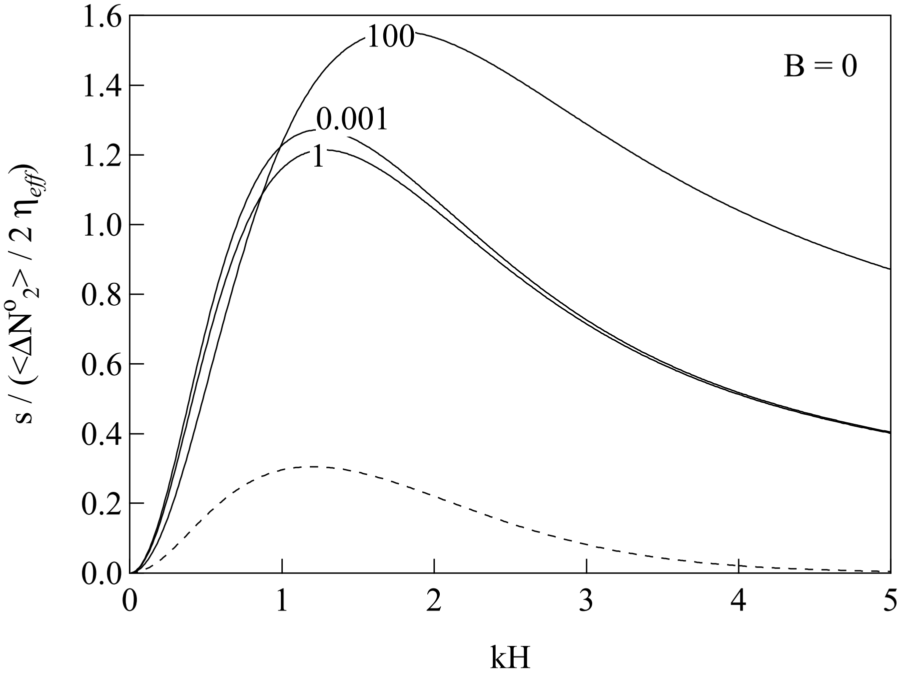

Figure 2.8: Falling film results for various ratios of η_p to η for $B = 0$. The range of η_p/η varies from 0.001 to 100. The apparent nonmonotonicity for small η_p/η arises because ΔN_2° is proportional to η_p. The dashed curve corresponds to a 'Newtonian' fluid film—ΔN_2° is presumed nonzero, but η_p is set to zero for the perturbed flow.

totic forms

$$s \quad \sim \quad \left(\frac{\langle \Delta N_2^\circ \rangle}{2\eta_{eff}}\right)(kH)^2 + \left(\frac{\pi \eta_p \rho g H}{105\eta_{eff}^2}\right)\left(\frac{350\eta_{eff}}{16\eta_p + 105\eta_{eff}}\right)(kH)^2 - \frac{1}{6}\frac{\gamma}{H\eta_{eff}}(kH)^4, \quad kH \quad \rightarrow \quad 0,$$

$$s \quad \sim \quad 0.00261\left(\frac{\langle \Delta N_2^\circ \rangle}{2\eta_{eff}}\right) + 1.975\left(\frac{\pi \eta_p \rho g H}{105\eta_{eff}^2}\right)\frac{1}{kH} - 2.033\left(\frac{\gamma}{8H\eta_{eff}}\right)(kH), \quad kH \quad \rightarrow \quad \infty,$$

where the latter is for $\eta_p = \eta$, although the relationship with kH would remain unchanged for other values of η. The separate terms in the growth rate correspond to the three driving forces on the RHS of (2.11a-2.11c): ΔN_2°, the enhanced flow under a crest $\rho g H$ and surface tension γ.

The results in Figure 2.7 are for the particle viscosity equal to the fluid viscosity, $\eta_p = \eta$. In Figure 2.8 we show the effect of varying η_p/η on the growth rate in the absence of surface tension

($B = 0$); the effect is much the same as for the Couette flow.

A similar analysis can be carried out for a film falling down a plane inclined at an angle relative to gravity. However, one cannot just simply change the magnitude of g in the above formulae because the component of gravity perpendicular to the layer couples to the stress boundary condition and the perturbation at the free surface. Nevertheless, the results are as to be expected with a decrease in the maximum growth rate and a shift to longer wavelengths as the angle of inclination approaches the horizontal.

2.4 Conclusions

In both of the problems considered a maximum growth rate exists at a wavelength on the order of the thickness of the film or layer (for non-zero surface tension). The size of the suspended particles does not enter. And the similarity of the results for the two-layer Couette flow and the falling film problem shows that the vanishing of N_2° at the free surface is not a fatal flaw for the falling film problem; a more complete analysis allowing for particle migration would presumably give qualitatively the same behavior. The growth rate is proportional to the shear rate—U/H for the Couette flow and $\rho g H/\eta_{eff}$ for the falling film problem—as this is the only timescale present in viscous suspensions, but its magnitude is set by the size of the second normal stress difference, i.e., $\eta_p(\phi)$. Normal stresses in suspensions are small at low concentration, behaving as ϕ^2 for small ϕ, but grow to be as large as the shear stress for volume fractions of 40% or larger. At the same time, concentrated suspensions tend to be very viscous and therefore in the falling film problem the instability will take a long time—and long length—to develop. It is also not fully understood how particle concentration affects the surface tension between two fluids, although the experiments of Zarraga *et al.* [16] indicate that it drops significantly for concentrated suspensions undergoing shear.

Unfortunately, it is not possible to make a direct comparison with experiment because there are no reported investigations of *linear* stability (or instability) in viscous suspensions. The observations that have been reported (e.g., [15]) are for fully-developed segregation effects that are certainly not small amplitude perturbations. The segregation patterns that have been observed might be the nonlinear evolution of this second normal stress jump instability—and the predictions of the stability analysis are not in conflict with the observations—but it is still an open question as to the origin of the segregation effects. To make a more direct comparison with the experiments one needs to carry out a more complete analysis that includes the spatial variation in the volume fraction, address the much more complicated flow geometry used in the rotating cylinder experiments, and determine the nonlinear evolution of the interface and concentration. It might, therefore, be worthwhile to investigate experimentally a two-layer Couette flow, or a two-layer torsional flow since the timescales can be long, and monitor directly the linear stability of the interface.

For granular flows the constitutive equation for the stress scales with the square of the shear rate (inertial stresses), rather than as the shear rate, which will surely change quantitatively the behavior. Furthermore, fluid inertia is now important and, while this does not affect the base states considered here since they are steady unidirectional flows valid for all Reynolds numbers, the disturbance equations are modified with additional inertial terms that can easily be included (specifically, $\rho(s\,u + v\,du^\circ/dy)\,, \rho(s\,v)$ and $\rho(s\,w)$). How this affects the stability analysis has not been determined. More importantly, constitutive equations that recognize the different constituents by size, weight, shape, angle of friction, etc. may be needed to predict segregation. It would be interesting to see if this second normal stress jump instability plays a role in granular segregation.

Bibliography

[1] J. Bergenholtz, J.F. Brady, and M. Vicic. The non-Newtonian rheology of dilute colloidal suspensions. *J. Fluid Mech.*, 456:239–275, 2002.

[2] R.B. Bird, R.C. Armstrong, and O. Hassager. *Dynamics of Polymeric Liquids*, volume 1. John Wiley & Sons, New York, 1977.

[3] J.F. Brady and J.F. Morris. Microstructure of strongly-sheared suspensions and its impact on rheology and diffusion. *J. Fluid Mech.*, 348:103–139, 1997.

[4] C.S. Campbell. The stress tensor for simple shear flows of a granular material. *J. Fluid Mech.*, 203:449–473, 1989.

[5] Z. Fang, A.A. Mammoli, J.F. Brady, M.S. Ingber, L.A. Mondy, and A.L. Graham. Flow-aligned tensor models for suspension flows. *Int. J. Multiphase Flow*, 28:137–166, 2001.

[6] D.R. Foss and J.F. Brady. Structure, diffusion and rheology of Brownian suspensions by Stokesian Dynamics simulations. *J. Fluid Mech.*, 407:167–200, 2000.

[7] K.M. Hill, A. Caprihan, and J. Kakalios. Bulk segregation in a rotated granular material measured by magnetic resonance imaging. *Phys. Rev. Lett.*, 78:50–53, 1997.

[8] K.M. Hill and J. Kakalios. Reversible axial segregation of rotating granular material. *Phys. Rev. E*, 52:4393–4400, 1995.

[9] E.J. Hinch, O.J. Harris, and J.M. Rallison. The instability mechanism for two elastic liquids being co-extruded. *J. Non-Newtonian Fluid Mech.*, 43:311–324, 1992.

[10] P.R. Nott and J.F. Brady. Pressure-driven flow of suspensions: simulation and theory. *J. Fluid Mech.*, 275:157–199, 1994.

[11] Y.Y. Renardy and M. Renardy. Instability due to second normal stress jump in a two-layer shear flow of the Giesekus fluid. *J. Non-Newtonian Fluid Mech.*, 81:215–234, 1999.

[12] S. Sami. Stokesian Dynamics simulation of Brownian suspensions in extensional flow. Master's thesis, California Institute of Technology, Pasadena, CA 91125, 1996.

[13] E.S.G. Shaqfeh. Purely elastic instabilities in viscometric flows. *Ann. Rev. Fluid Mech.*, 28:129–185, 1996.

[14] A. Sierou and J.F. Brady. Rheology and microstructure in concentrated noncolloidal suspensions. *J. Rheol.*, 46:1031–1056, 2002.

[15] M. Tirumkudulu, A. Mileo, and A. Acrivos. Particle segregation in monodisperse sheared suspensions in a partially filled rotating horizontal cylinder. *Phys. Fluids*, 12:1615–1618, 2000.

[16] I.E. Zarraga, D.A. Hill, and D.T. Leighton. The characterization of the total stress of concentrated suspensions of noncolloidal spheres in Newtonian fluids. *J. Rheol.*, 44:185–220, 2000.

Chapter 3

Gravitational Instability in Suspension Flow

3.1 Introduction

Particulates are an integral part of many industries, and whether in the form of suspensions or dry granular flows, they present an engineering challenge that has so far been met empirically and with only partial success. Thus, there has been interest in the last few decades in analyzing the complex behaviors of granular and granular-fluid flow, but the field remains rich with unexplained problems, with new phenomena being continually discovered.

Granular media can exhibit complex behaviours, being solid, liquid, or gas-like depending on the situation, and sometimes exhibiting multiple states (e.g., see the reviews by Jaeger and coworkers [7, 6] and Savage [13]). Among the interesting facets of granular flow behavior is a large set of instabilities, including oscillons formed in vertically vibrated containers, e.g., see [15], segregation of granular media in mixers driven by such differences in particle properties as size, density and shape [5], fingering instabilities in suspensions and dry granular flows [8, 12], segregation of neutrally-buoyant particles in suspensions [14], wave patterns in sand [4], and longitudinal vortices in granular flows [3]. Analyzing these instabilities and patterns can lead to crucial insights into granular and granular-fluid flow behaviour.

In many situations, the particles are heavier than the suspending fluid, whether liquid or gas, and the resulting density variations can lead to flow, as in the experiments of [3] for granular flow down an inclined plane, or the fingering instability in a sedimenting suspension analysed by [16]. In flows with heavy particles, rapid shearing motion adjacent to a boundary can create a region of low density that supports the weight of a denser, slower shearing layer (c.f. Figure 3.5). This adverse density stratification can then be unstable to spanwise (or longitudinal) disturbances, similar to the classic Rayleigh–Taylor

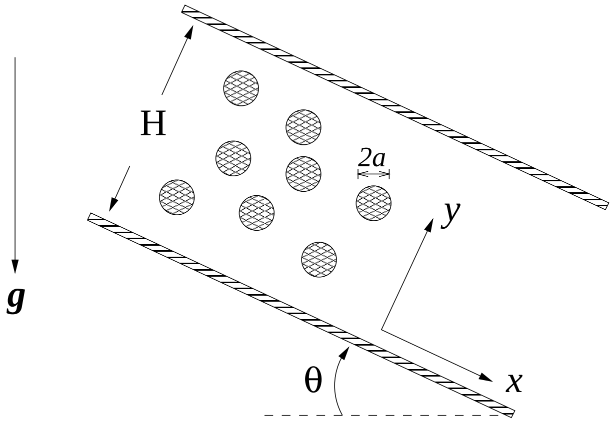

Figure 3.1: Gravity-driven flow of a suspension through an inclined channel of height H. The inclination angle θ ranges between 0° and 90°, from pure sedimentation to vertical flow. The direction parallel to the channel walls (the flow direction) is taken to be x.

instability: a local increase in density (or particle fraction) will fall due to gravity and drag down material from above which is even denser, further enhancing the perturbation. This instability mechanism appears to be new and generic, although the precise growth rates and wavelengths will depend on the nature of the suspension or granular flow. This instability may be operative in several granular and suspension flows and may be responsible for a variety of patterns observed in these systems.

To illustrate this basic instability mechanism we consider the situation of a heavy particle viscous suspension flowing through an inclined channel and examine its stability towards perturbations spanwise to the flow. In the gravity-driven flow, the particle volume fraction, and therefore the density, can increase with height in the velocity gradient direction due to a balance between shear-induced particle migration and buoyancy and thus be unstable. Section 3.2 defines the problem and introduces the governing equations. The base state showing the adverse density stratification is discussed in §3.3, and its linear stability to spanwise perturbations is considered in §3.4, where the motion is seen to be unstable at all wavelengths, with a maximum growth rate at a wavelength on the order of the suspension layer thickness. Concluding remarks are given in §3.5.

3.2 The governing equations

The problem considered is gravity-driven flow of a suspension down an inclined channel as illustrated in Figure 3.1. The system is modeled as a continuum viscous suspension and we use the suspension-balance model of [10] as modified by [9]. In the following we ignore inertial effects, an acceptable assumption for low particle and geometry Reynolds numbers, and the suspension as a whole is incompressible. Thus, conservation of mass and momentum for the suspension are

$$\boldsymbol{\nabla} \cdot \langle \boldsymbol{u} \rangle = 0 \tag{3.1a}$$

and

$$\boldsymbol{\nabla} \cdot \langle \boldsymbol{\sigma} \rangle + \rho\, \boldsymbol{g} = 0, \tag{3.1b}$$

where $\rho = \rho_f + \Delta\rho\phi$ and $\Delta\rho = \rho_p - \rho_f$. The subscripts p and f denote the particle and fluid phases, respectively. We also have mass and momentum conservation for the particle phase:

$$\frac{\partial \phi}{\partial t} + \boldsymbol{\nabla} \cdot \langle \boldsymbol{u} \rangle_p \phi = 0 \tag{3.2a}$$

and

$$\boldsymbol{\nabla} \cdot \langle \boldsymbol{\sigma} \rangle_p + \Delta\rho\, \phi\, \boldsymbol{g} - \frac{9}{2}\frac{\eta}{a^2}\frac{\phi}{f(\phi)}(\langle \boldsymbol{u} \rangle_p - \langle \boldsymbol{u} \rangle) = 0, \tag{3.2b}$$

where $f(\phi)$ is the hindered settling function, and ϕ denotes the volume fraction of particles of size a. The stress $\langle \boldsymbol{\sigma} \rangle$ and the velocity $\langle \boldsymbol{u} \rangle$ are suspension-averaged quantities (particle-phase averages if accompanied by the subscript p). In addition to the mass and momentum conservation equations for the suspension and the particle phases, it is necessary to include an energy balance, bringing in the suspension temperature. In an inhomogeneous flow, the stress can be finite even in regions of vanishing shear rate due to a possibly non-zero local fluctuational motion $\boldsymbol{u}'_p = \boldsymbol{u}_p - \langle \boldsymbol{u} \rangle_p$. The suspension temperature $T = \langle \boldsymbol{u}'_p \cdot \boldsymbol{u}'_p \rangle$ introduces the necessary nonlocality for the stress. For these inertia-free flows the energy balance takes the form

$$\langle \boldsymbol{\sigma} \rangle_p : \langle \boldsymbol{e} \rangle - \eta \frac{\alpha(\phi)}{a^2} T + \eta \boldsymbol{\nabla} \cdot \kappa(\phi) \boldsymbol{\nabla} T = 0, \tag{3.3}$$

where $\langle \boldsymbol{e} \rangle$ is the average rate of strain tensor, and the flux of fluctuational energy has been modeled by a Fourier-type law. For convenience in notation, $\langle \cdot \rangle$, denoting an average, shall be dropped from all further equations.

The constitutive relations for the particle and suspension stresses are taken to be those appropriate for a viscous suspension [9]:

$$\boldsymbol{\sigma}_p = -\Pi \boldsymbol{I} + 2\eta\eta_p(\phi)\boldsymbol{e} \tag{3.4a}$$

and

$$\boldsymbol{\sigma} = -p_f \boldsymbol{I} + 2\eta \boldsymbol{e} + \boldsymbol{\sigma}_p = -\left(p_f + \Pi\right) \boldsymbol{I} + 2\eta\eta_s(\phi)\boldsymbol{e}, \tag{3.4b}$$

where Π is the particle-phase pressure

$$\Pi = \eta a^{-1} p(\phi) \sqrt{T}, \tag{3.4c}$$

p_f is the average pressure in the fluid, and η_p and η_s are the relative viscosities for the particle phase and the suspension, respectively.

To close the equation set we also need to specify the volume fraction dependence of the functions p, η_s, α, κ and f; as in [9], we take these functions to be

$$p(\phi) = \eta_p(\phi), \tag{3.5}$$

$$\eta_s(\phi) = 1 + \eta_p(\phi) = \left(1 - \phi/\phi_m\right)^{-2}, \tag{3.6}$$

$$\alpha(\phi) = k_\alpha \eta_p(\phi)/\phi, \tag{3.7}$$

$$\kappa(\phi) = k_\kappa \eta_p(\phi) \tag{3.8}$$

and

$$f(\phi) = (1-\phi)^{-5}, \tag{3.9}$$

with $k_\alpha = 0.815$ and $k_\kappa = 0.8$. The maximum volume fraction is taken to be $\phi_m = 0.68$. In a homogeneous shear flow with constant shear rate $\dot{\gamma}$, $\langle\sigma\rangle_p = \eta\eta_p\dot{\gamma}$ and equation (3.3) gives an uniform suspension temperature $T = (\dot{\gamma}a)^2\alpha(\phi)/\eta_p(\phi)$ as expected.

For a more complete description of the model chosen and the reasoning behind its derivation, the reader is referred to [10], [9] and references contained therein.

3.3 The base state

The parameters that govern the flow are the angle of inclination with respect to the horizontal, θ, the ratio of the particle size, a, to the channel width, H, with $\epsilon = a/H \ll 1$, the bulk volume fraction of particles, ϕ_b, and the density ratio $B = \Delta\rho/\rho_f$. The gravitational acceleration g and the fluid viscosity η are important in establishing the characteristic velocity, $U_c = \rho_f g H^2/\eta$, but do not appear in the dimensionless groups characterising the problem and therefore affect only the quantitative behaviour of the system. Gravity affects the qualitative behaviour of the system through the angle of inclination θ.

The base state flow is unidirectional, parallel to the channel walls, and satisfies the conservation equations (3.1–3.3). Using the constitutive relations defined above and taking (u, v, w) as the (x, y, z) components of the suspension velocity, we obtain the following system of dimensionless equations, where the variables are scaled with $y \sim H$, $u \sim U_c$ and $T \sim \epsilon^2 U_c^2$:

$$\frac{d}{dy}\eta_s(\phi)\frac{du}{dy} = -(1 + B\phi)\sin\theta, \tag{3.10a}$$

$$\frac{d}{dy}\left(p(\phi)\sqrt{T}\right) = -B\phi\,\cos\theta \tag{3.10b}$$

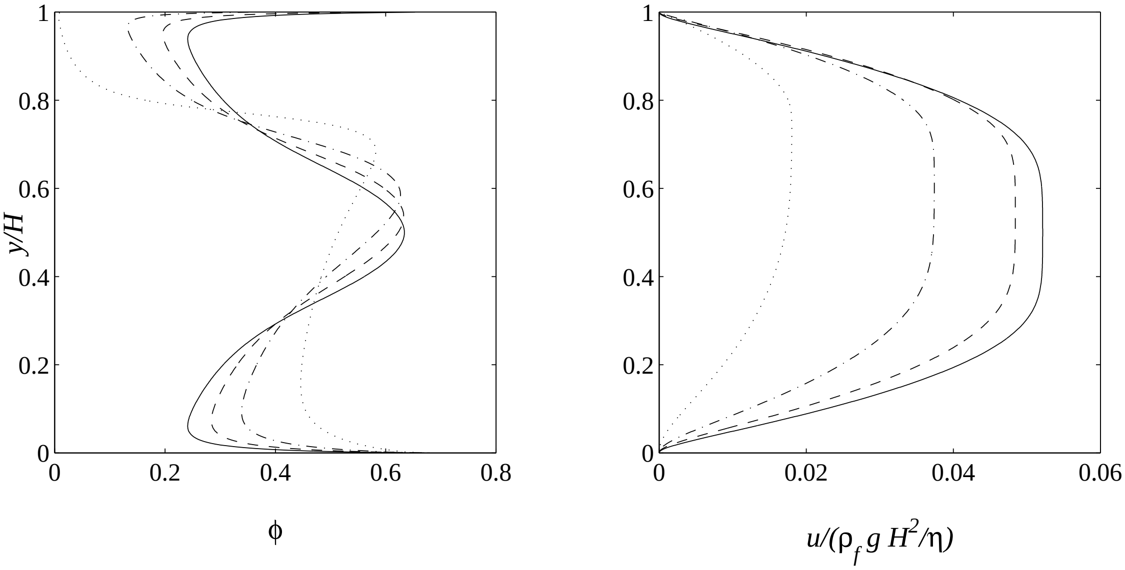

Figure 3.2: Base state particle volume fraction and velocity profiles for $\phi_b = 0.40$, $H/a = 30.54$ and $B = 1$: $\theta = \{30^\circ$ (*dotted*), 50° (*dash-dotted*), 70° (*dashed*), 90° (*solid*)$\}$. Increasing θ results in increasing symmetry around the centre of the channel.

and

$$\epsilon^2 \frac{d}{dy}\kappa(\phi)\frac{dT}{dy} - \alpha(\phi)T = -\eta_p(\phi)\left(\frac{du}{dy}\right)^2. \tag{3.10c}$$

The velocity, temperature and volume fraction satisfy the boundary conditions

$$u = 0 \quad \text{at } y = 0 \text{ and } y = 1, \tag{3.11a}$$

$$T = \frac{\eta_p(\phi)}{\alpha^*(\phi)}\left(\frac{du}{dy}\right)^2 \quad \text{at } y = 0 \text{ and } y = 1, \tag{3.11b}$$

and the integral constraint on volume fraction reads

$$\int_0^1 \phi(y)\, dy = \phi_b. \tag{3.11c}$$

In (3.11b) $\alpha^*(\phi) = 20\,\alpha(\phi)$ [9] stating that the fluctuational motion is reduced near a boundary but scales in the same manner as in the bulk. In the base state $u_p - u \sim O(\epsilon^2)$, i.e., there is no phase slip.

This system does not lend itself to an analytical solution and was solved numerically. Typical

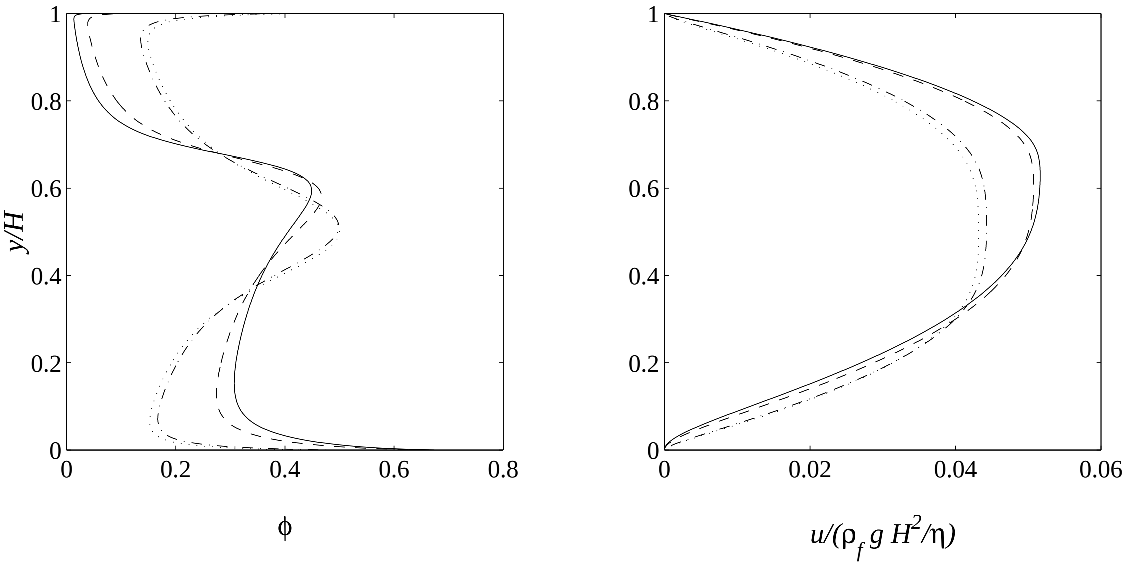

Figure 3.3: Base state volume fraction and velocity profiles for $\phi_b = 0.27$, $\theta = 45°$, $H/a = 18.32$ and $B = \{0.01$ (*dotted*), 0.1 (*dash-dotted*), 1 (*dashed*), 1.4 (*solid*)$\}$. For small B the velocity grows with increasing B. It achieves a maximum for $B \approx 1$, and experiences a slight decrease upon further increase in B. Increasing B always results in increasing asymmetry in the velocity and density profiles.

results are shown in Figure 3.2 for a range of channel inclinations and at a density ratio $B = 1$, in Figure 3.3 for a range of B at a specific channel inclination and in Figure 3.4 for a range of bulk volume fractions and a range of $\epsilon = a/H$, the ratio of particle size to channel height. In general, the suspension velocity profile is blunted in comparison to the corresponding parabolic Newtonian velocity profile—the variation in the particle volume fraction affects the suspension viscosity, very strongly so in regions of high density such as near the centre of the channel (where $\phi \to \phi_m$), and since the shear stress varies almost linearly with position, the shear rate is diminished in those regions. Note that the blunting of the velocity profile 'follows' the maximum in the volume fraction (see Figure 3.3). Decreasing inclination angle, θ, and increasing density ratio, B, lead to increasing sedimentation, and in the limits $\theta \to 0$ or $B \to \infty$ the particles pack down on the bottom of the channel and flow as a plug (if they flow at all—in the $\theta \to 0$ limit, the driving force for flow in the x direction is lost and the system becomes a sedimenting one). However, for $\theta \neq 0$ and more physically reasonable density ratios, $B \sim O(1)$, the particle volume fraction varies in a more interesting manner across the channel, as seen in Figure 3.2, reminiscent of the results of [10] and [9] for pressure-driven flow. Similar to the results of [9], we note that having particles of a

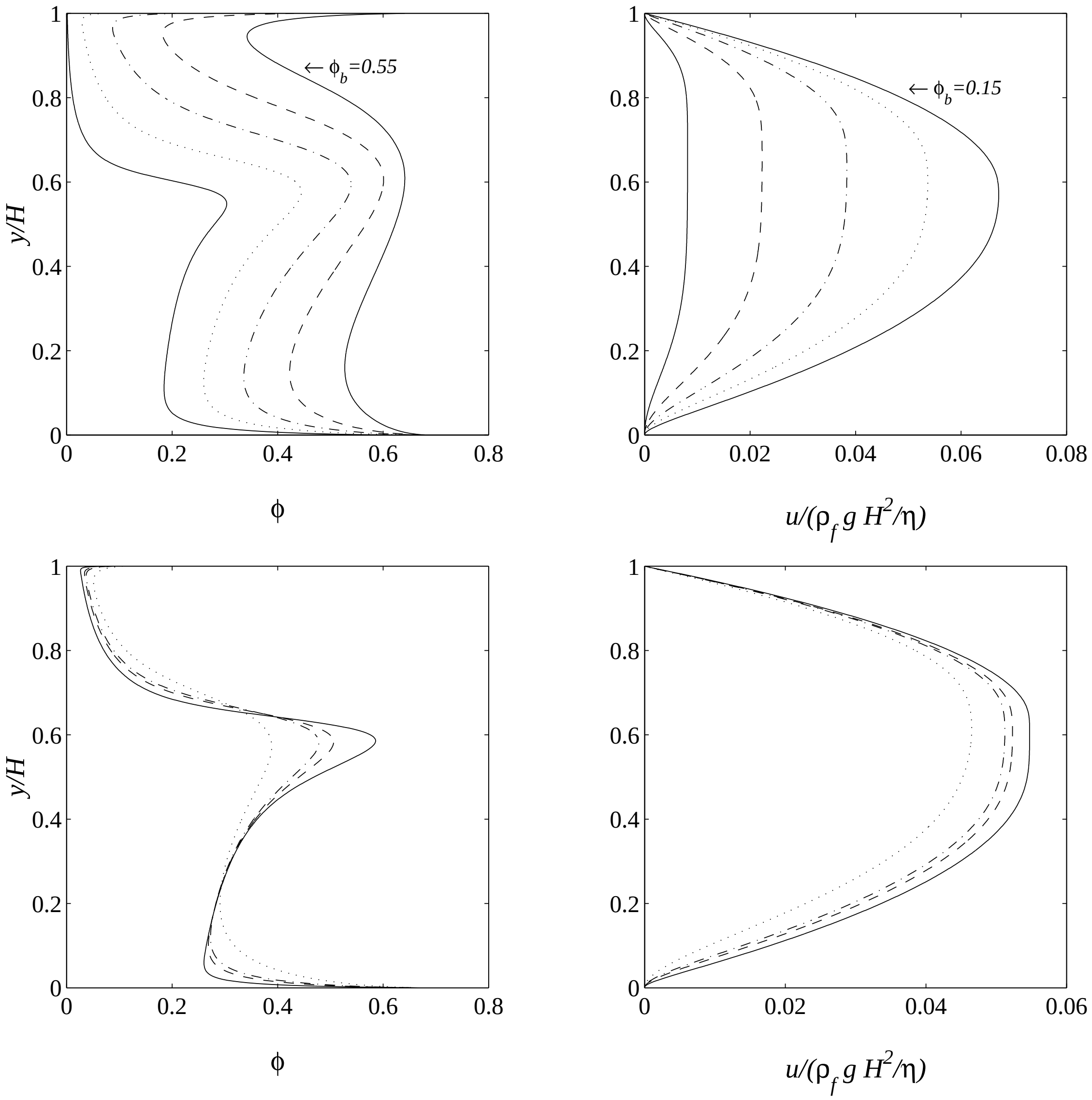

Figure 3.4: Base state volume fraction and velocity profiles for $B = 1$ and $\theta = 45°$. Top: $H/a = 18.32$, with $\phi_b = \{0.15$ (*solid*), 0.25 (*dotted*), 0.35 (*dash-dotted*), 0.45 (*dashed*), 0.55 (*solid*)$\}$. Bottom: $\phi_b = 0.27$, with $H/a = \{10$ (*dotted*), 20 (*dash-dotted*), 25 (*dashed*), 50 (*solid*)$\}$. The velocity increases with decreasing ϕ_b and increasing H/a. The density (volume fraction) profile decreases with decreasing ϕ_b and its maximum in the centre of the channel becomes more pronounced with increasing H/a.

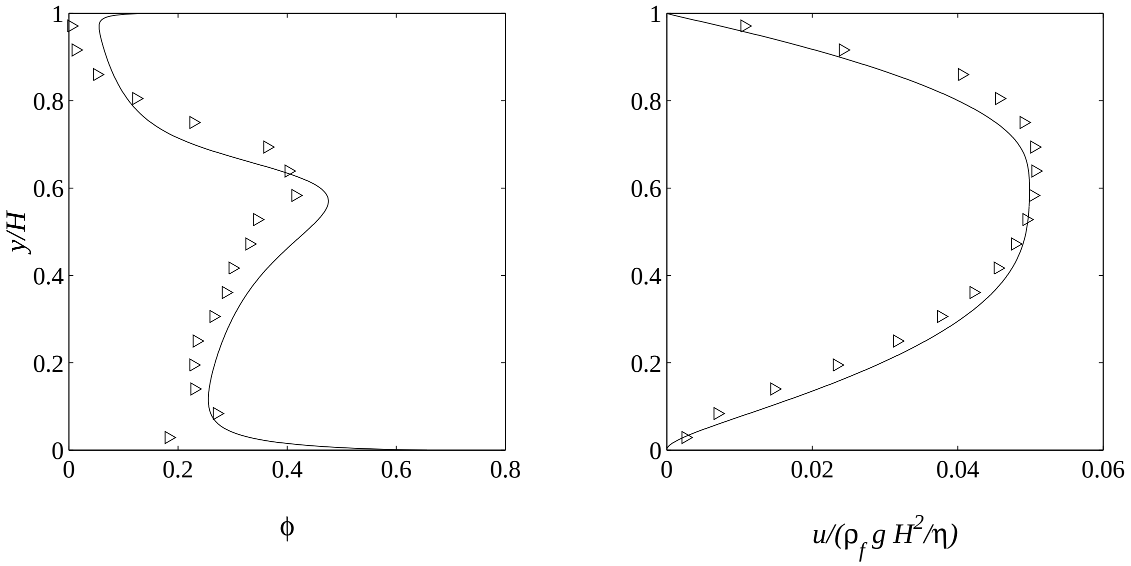

Figure 3.5: Base state particle volume fraction and velocity profiles for $\phi_b = 0.27$, $H/a = 18.32$, $B = 0.8$ and $\theta = 45°$. Comparison of model results (line) with Stokesian Dynamics simulations (triangles).

different density breaks the symmetry around the centre of the channel, such that the maximum in the particle volume fraction and in the velocity tends to occur above the centreline. Most importantly, the rapid shearing motion close to the bottom wall generates a large pressure (via the suspension temperature and (3.4c) for the particle-phase pressure) so that the region of low density near the wall can support the weight of the heavier, slower shearing region in the middle, and the system has an adverse density profile of heavier material over light, the driving force for instability.

The results of the model compare favorably to Stokesian Dynamics simulations, as can be seen in Figure 3.5. These base state profiles may depend slightly upon the choice of model—for example, one could use the diffusive-flux model of [17]. However, as shown in [2, Fang *et al.* (2002)], these differences are minor, and the inverted concentration profile, the important result, is maintained regardless of the model chosen. The mechanism of instability and all of the conclusions drawn here are therefore independent of the model.

3.4 Linear stability analysis

We perform a standard linear stability analysis of equations (3.1–3.3) to perturbations in the spanwise direction z of the form $f'(y) = \delta f(y)\,\mathrm{e}^{ikz+st}$, with k the wavenumber and s the growth rate. Here δ is the small amplitude of the perturbation. ($f(y)$ denotes a general function, not to be confused with the hindered settling function $f(\phi)$.) All variables are non-dimensionalized as before. In solving the perturbed problem, all terms of $O(\epsilon^2, \delta^2)$ or smaller are neglected, and the linearized perturbation problem becomes:

$$\mathrm{D}\left(\eta_s^\circ \mathrm{D}u\right) - \tilde{k}^2 \eta_s^\circ u = -B\psi \sin\theta - \mathrm{D}\left(\eta_s' \psi \mathrm{D}u^\circ\right), \tag{3.12a}$$

$$\left(\mathrm{D}^2 + \tilde{k}^2\right) \eta_s^\circ \left(\mathrm{D}^2 + \tilde{k}^2\right) v - 4\tilde{k}^2 \mathrm{D}\left(\eta_s^\circ \mathrm{D}v\right) = -B\psi\tilde{k}^2 \cos\theta, \tag{3.12b}$$

$$\tilde{s}\psi = -v\mathrm{D}\phi^\circ \tag{3.12c}$$

and

$$-\alpha^\circ T = \alpha' T^\circ \psi - 2\eta_p^\circ \mathrm{D}u^\circ \mathrm{D}u - \eta_p' \left(\mathrm{D}u^\circ\right)\psi, \tag{3.12d}$$

subject to the conditions

$$u = v = \mathrm{D}v = 0 \quad \text{at } y = 0 \text{ and } y = 1, \tag{3.13a}$$

$$T = \frac{{\eta_p}'}{\alpha}\psi\left(\mathrm{D}u^\circ\right)^2 + 2\frac{\eta_p^\circ}{\alpha^\circ}\mathrm{D}u^\circ \mathrm{D}u \quad \text{at } y = 0 \text{ and } y = 1 \tag{3.13b}$$

and

$$\int_0^1 \int_{-W/H}^{W/H} \psi \, dy \, dz = 0, \tag{3.13c}$$

where ψ is the perturbation in volume fraction, $\mathrm{D} = d/dy$, $^\circ$ denotes a base state quantity and the $'$ denotes differentiation with respect to the volume fraction. The dimensionless wavenumber and growth rate are $\tilde{k} = kH$, $\tilde{s} = sH/U_c = s/(\rho_f gH/\eta)$, respectively, and W is the period of the perturbation in the z direction.

In order to determine the growth rate $\tilde{s}(\tilde{k})$, we need only solve the eigenvalue problem

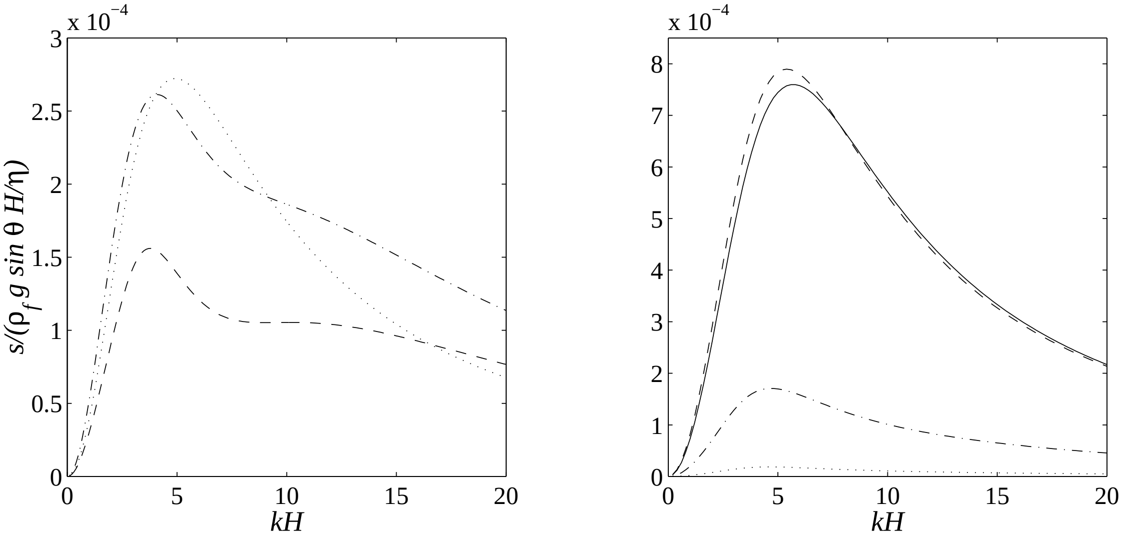

Figure 3.6: Left: dimensionless temporal growth rate of the instability, $s/(\rho_f g \sin\theta H/\eta)$, as a function of dimensionless wavenumber kH for $\phi_b = 0.40$, $H/a = 30.54$ and $B = 1$: $\theta = \{30^\circ$ (*dotted*), 50° (*dash-dotted*), 70° (*dashed*)$\}$. Because here s has been scaled with $\sin\theta$, the growth rate increases with decreasing θ. If this scaling were removed, the growth rate would achieve a maximum at an intermediate value of θ. Right: $\phi_b = 0.27$, $H/a = 18.32$ and $\theta = 45^\circ$: $B = \{0.01$ (*dotted*), 0.1 (*dash-dotted*), 1 (*dashed*), 1.4 (*solid*)$\}$.

obtained by combining (3.12b) and (3.12c):

$$\left(\mathrm{D}^2 + \tilde{k}^2\right)\eta_s^\circ\left(\mathrm{D}^2 + \tilde{k}^2\right)v - 4\tilde{k}^2\mathrm{D}\left(\eta_s^\circ \mathrm{D}v\right) = -\frac{B\,\tilde{k}^2\cos\theta\,\mathrm{D}\phi^\circ}{\tilde{s}}v, \tag{3.14}$$

with the boundary conditions on v given by (3.13a). Equation (3.14) shows clearly that the driving force for the instability is the base state density gradient $\mathrm{D}\phi^\circ = d\phi^\circ/dy$. When $d\phi^\circ/dy > 0$ the system has an adverse density stratification and is unstable. Equation (3.14) is a fourth order ordinary differential equation with variable coefficients and was solved numerically. *Matlab* proved quite helpful in this regard and the results corresponding to the base state profiles given in the previous section are shown in Figure 3.6 and Figure 3.7.

In the sedimenting limit, $\theta \to 0$ or $B \to \infty$, the density gradient $\mathrm{D}\phi^\circ$ is negative throughout the channel, and the system is stable—light material over heavy. However, for intermediate values of θ ($0^\circ < \theta < 90^\circ$) and B there is always some heavier material above light, a system which is inherently unstable. In these regimes, the temporal growth rate of the instability is positive and any small per-

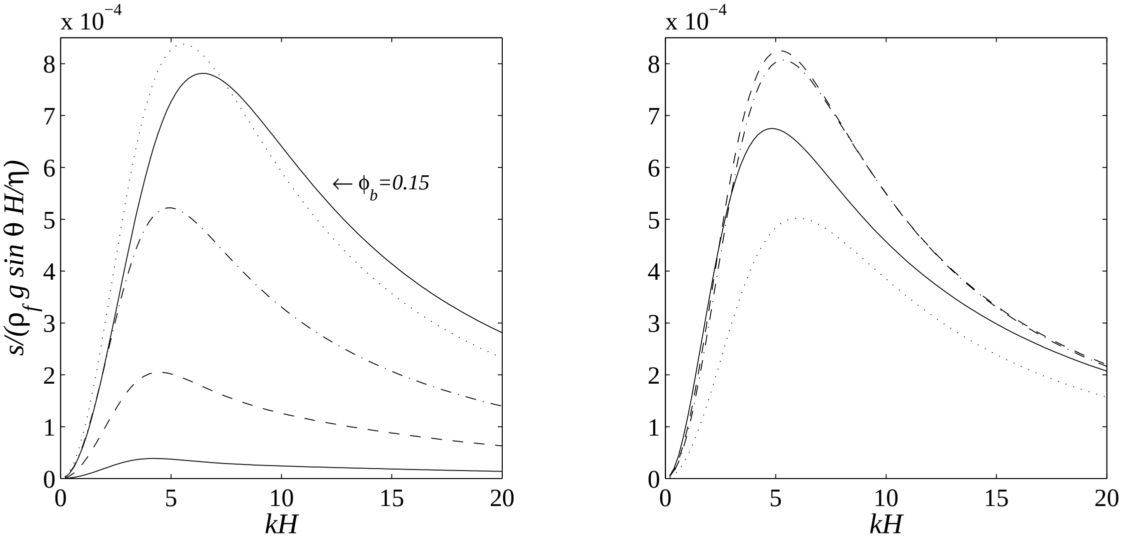

Figure 3.7: Left: dimensionless temporal growth rate of the instability, $s/(\rho_f g \sin\theta H/\eta)$, as a function of dimensionless wavenumber kH for $B = 1$, $\theta = 45°$, $H/a = 18.32$ and $\phi_b = \{0.15$ (*solid*), 0.25 (*dotted*), 0.35 (*dash-dotted*), 0.45 (*dashed*), 0.55 (*solid*)$\}$. Right: $B = 1$, $\theta = 45°$, $\phi_b = 0.27$ and $H/a = \{10$ (*dotted*), 20 (*dash-dotted*), 25 (*dashed*), 50 (*solid*)$\}$.

turbation would grow. The system is unstable for all wavenumbers, with a maximum growth rate at a wavelength of $O(H)$, the height of the layer. (From (3.14) one can see that in the low wavenumber limit ($\tilde{k} \to 0$) $\tilde{s}$ grows as $\tilde{k}^2$, while in the high wavenumber limit ($\tilde{k} \to \infty$) $\tilde{s}$ decays as $1/\tilde{k}^2$ due to viscous damping.) Thus, one would expect patterns of this wavelength to form initially, which might then lead to the kinds of patterns seen in suspension and granular flows. (Note that, although the system is unstable as $\tilde{k} \to \infty$, when the wavelength is of order the particle size, $ka \sim O(1)$, the continuum model may no longer be appropriate and we could expect, therefore, a high $\tilde{k}$ cutoff.)

The results shown in Figure 3.6 illustrate the effect of varying B and θ upon the growth rate of the instability. Increasing B—increasing the relative density difference between the particles and fluid—causes the system to be more unstable, at least in the intermediate B range. The instability of the system is also dependent upon θ. Basically, the two extremes of inclination—horizontal and vertical—give two stability limits. In the limit $\theta \to 0°$, the system moves towards sedimentation. In the limit $\theta \to 90°$, there is no longer a component of gravity perpendicular to the walls, and, even though the density varies in the 'right' way for instability, the system is stable due to the lack of a driving force. As a result, the system is most unstable for angles that lie between these two extremes. Figure 3.7 (left) illustrates the effect of varying the bulk volume fraction ϕ_b. Increasing ϕ_b is similar to increasing B—the system becomes slightly more stable for the higher bulk volume fractions. Figure 3.7 (right) shows the effect of varying H/a, and it is seen that provided $H/a10$ there is little effect of the particle size on the instability. (Note that H/a must be large in order to treat the suspension as a continuum.) Indeed, to a first approximation the growth rate and most rapidly growing wavelength are roughly independent of particle size and the slight decrease in the growth rate for large H/a is due to the high volume fraction near the centreline (c.f. Figure 3.4) which increases the local viscosity. It is important to note that the system is most unstable at intermediate values of the parameters—that is, when the system is at its most physically reasonable—not $\theta \to 0°$ nor $\theta \to 90°$, not $B \to 0$ nor $B \to \infty$, not $H/a \to 1$ nor $H/a \to \infty$ and not $\phi_b \to 0$ nor $\phi_b \to \phi_m$, but somewhere in between.

3.5 Conclusions

For the problem of gravity-driven flow of non-neutrally buoyant suspensions, we report the existence of a maximum growth rate for spanwise instabilities on the order of the height of the channel, H. The instability is present whenever the flow-generated density gradient is aligned antiparallel to gravity. Although this unstable density gradient is generated only by flow, it shares some characteristics with the classical Rayleigh–Taylor instability—basically, having heavier material over light. The system is unstable to small perturbations over the range of the most physically-reasonable particle-fluid density ratios and channel inclination angles, with the growth rate of the instability depending upon these parameters as well as on the bulk particle volume fraction and to a much lesser extent on the ratio of particle size to channel height. As seen in Figures 3.6 and 3.7 the growth rate is small and therefore one would need a long channel $[L/H \sim O(1/\tilde{s})]$ in order to see the instability, suggesting that rotating drum experiments might be more desirable in practice. Also note that although the precise details of the growth rate, etc. depend on the constitutive relations used in the suspension-balance model, the basic instability mechanism does not.

Although we are not aware of any heavy viscous suspension experiments with which to compare, the experiments of [3] for the stability of granular flow down an inclined plane are qualitatively similar to the system examined in this work. Rapid granular flows display the same flow-induced adverse density profile and therefore should be subject to the same instability. Indeed, the experiments of [3] showed the formation of spanwise patterns whose wavelength was on the order of $3h$, where h was the height of their granular layer. It is interesting to note that for the current work, the most unstable wavelength tends to be approximately $1.2H$ for most parameter sets (corresponding to $\tilde{k} \sim 5$), and since the channel height is approximately twice that of the suspension layer, $H \approx 2h$, the most unstable wavelength is approximately $2.4h$, quite close to the observed granular flow instability wavelength.

In addition to the extra inertial effects associated with granular flows (note, however, that in the steady unidirectional base state, inertia is not important), the stability of suspensions and granular flows may also be affected by the presence of normal stress differences [1], which were not included in the present analysis. Normal stresses can be expected to enhance the intriguing behaviour of these systems and might prove interesting to investigate.

Finally, the gravity-driven flow investigated here may also be unstable to longitudinal perturbations—in the flow direction, for example as seen in the case of stratified flow with a free surface [11]—perturbations whose form will now be complex—a traveling wave in addition to an exponentially growing part.

Bibliography

[1] J.F. Brady and I.C. Carpen. Second normal stress jump instability in non-Newtonian fluids. *J. Non-Newtonian Fluid Mech.*, 102:219–232, 1997.

[2] Z. Fang, A.A. Mammoli, J.F. Brady, M.S. Ingber, L.A. Mondy, and A.L. Graham. Flow-aligned tensor models for suspension flows. *Int. J. Multiphase Flow*, 28:137–166, 2001.

[3] Y. Forterre and O. Pouliquen. Longitudinal vortices in granular flows. *Phys. Rev. Lett.*, 86:5886–5889, 2001.

[4] E. Fried, A.Q. Shen, and S.T. Thoroddsen. Wave patterns in a thin layer of sand within a rotating horizontal cylinder. *Phys. Fluids*, 10:10–12, 1998.

[5] K.M. Hill and J. Kakalios. Reversible axial segregation of rotating granular material. *Phys. Rev. E*, 52:4393–4400, 1995.

[6] H.M. Jaeger, S.R. Nagel, and R.P. Behringer. Granular solids, liquids, and gases. *Phys. Today*, 49:32–38, 1996.

[7] H.M. Jaeger, S.R. Nagel, and R.P. Behringer. The physics of granular materials. *Rev. Mod. Phys.*, 68:1259–1273, 1996.

[8] A. Lange, M. Schröter, M.A. Scherer, A. Engel, and I. Rehberg. Fingering instability in a water-sand mixture. *Eur. Phys. J. B*, 4:475–484, 1998.

[9] J.F. Morris and J.F. Brady. Pressure-driven flow of a suspension: buoyancy effects. *Int. J. Multiphase Flow*, 24:105–130, 1998.

[10] P.R. Nott and J.F. Brady. Pressure-driven flow of suspensions: simulation and theory. *J. Fluid Mech.*, 275:157–199, 1994.

[11] P. Plaschko and U. Schaflinger. Absolute instabilities in two-layer gravity driven film flow with a free surface. *Z. angew. Math. Phys.*, 49:194–204, 1998.

[12] O. Pouliquen, J. Delour, and S.B. Savage. Fingering in granular flows. *Nature*, 386:816–817, 1997.

[13] S.B. Savage. The mechanics of rapid granular flows. *Adv. Appl. Mech.*, 24:289–366, 1984.

[14] M. Tirumkudulu, A. Mileo, and A. Acrivos. Particle segregation in monodisperse sheared suspensions in a partially filled rotating horizontal cylinder. *Phys. Fluids*, 12:1615–1618, 2000.

[15] P.B. Umbanhowar, F. Melo, and H.L. Swinney. Localized excitations in a vertically vibrated granular layer. *Nature*, 382:793–796, 1996.

[16] C. Völtz, W. Pesch, and I. Rehberg. Rayleigh-Taylor instability in a sedimenting suspension. *Phys. Rev. E*, 65:Art. No. 011404, 2002.

[17] K. Zhang and A. Acrivos. Viscous resuspension in fully developed laminar pipe flows. *Int. J. Multiphase Flow*, 20:579–591, 1994.

Chapter 4

Microrheology

4.1 Introduction

Rheology, the study of the deformation and flow of matter, has a long history with many of its experimental methods and tools firmly established, and it is in the measurements that one finds the most novelty. However, the end of the last century saw tremendous improvements in imaging technology and computing power, which have enabled scientists to look at rheology on a different level—at the microscopic scale. In the last decade microrheology, as this type of rheology has come to be called, has gained momentum as a novel tool with novel measurements, useful for studying the properties of materials on a much smaller scale. In this, it is particularly well-suited for examining the properties of soft, heterogeneous materials, especially biological materials. Such multiphase, or complex, materials present a challenge to traditional rheology—bulk measurements alone provide little insight when a material can internally rearrange under deformation.

Among the collection of techniques known as microrheology, most involve tracking the motion of a colloidal particle or set of particles in order to determine the properties of the surrounding environment [20]. Due to the small length scales involved, microrheology became practical only with recent advances in technology (although early examples do exist [12]); the imaging technology itself also places constraints on the minimum level of error one can expect [16]. Particle-tracking microrheology can be categorized as either *passive*—tracking the random motion of probe particles due to thermal fluctuations—or *active*—applying a constant or oscillatory force to the probe particles, for example by using optical tweezers or magnetic fields. Unlike conventional rheology, which studies bulk properties, microrheology allows the measurement of local viscoelastic properties and requires minute material samples, a particular bonus for scarce biomaterials and systems such as individual cells; for gels, microrheology also avoids the problem of slip at the walls, often encountered with rheometers. Microrheological techniques have been used to study a diverse set of systems: cells [3, 14, 19], actin networks [13, 25], gelatin [12], DNA and polyethylene oxide solutions [21], and the behavior of colloids near the glass transition [15], as well as fundamental interactions between pairs of colloidal spheres [7] and entropic forces in binary colloids [8]. Microrheology has also been proposed as a tool for fundamental physics and for high-throughput material screening [6].

The cornerstone of passive particle-tracking microrheology is the use of the generalized Stokes-Einstein relation for a sphere in a homogeneous, incompressible fluid. For single particle tracking experiments, this takes the form:

$$D^s_\infty = \frac{kT}{6\pi\eta_{eff}a}, \tag{4.1}$$

where D^s_∞ is the long-time self-diffusivity of the probe, obtained from its mean-squared-displacement, η_{eff} is the sought-after effective viscosity of the medium, kT is the thermal energy, and a is the radius of the probe particle. A similar equation applies for two-point microrheology, for which the correlated motion of pairs of particles is used instead of the single-particle mean-squared-displacement [9]. The Stokes-Einstein relation translates the microrheological measurement (mean-squared-displacement) into the macroscopic measurement (effective viscosity or complex modulus), and is therefore crucial to any type of comparison between micro- and macrorheology. Most applications of microrheology have been in this passive regime and the applicability, or lack thereof, of the generalized Stokes-Einstein equation (4.1) has been examined [9]. In the passive regime, the mean-squared-displacement of the probe is a measure of the diffusivity, and the macroscopic rheology ‘equivalent’ is the dynamic viscosity; both properties have been extensively studied for colloidal dispersions (e.g., [5],[24]). Further, Brady [5] has shown theoretically that the frequency (or time)-dependent self-diffusivity can be compared to the frequency-dependent dynamic viscosity, with good agreement for all frequencies and volume fractions when the different volume fraction scalings ($\mathcal{O}(\phi)$ versus $\mathcal{O}(\phi^2)$ in the dilute limit, reflecting the dipolar versus quadrupolar forcing) are taken into account (see also Khair and Brady [18]).

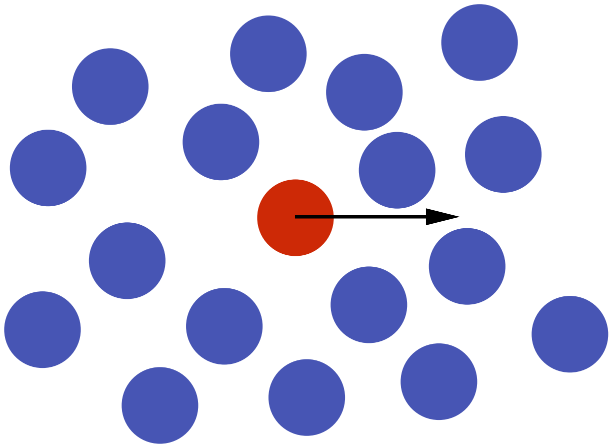

Figure 4.1: The model system: a probe particle is dragged by means of an imposed external force through a surrounding suspension of monodisperse force-free bath particles. The relative strength of Brownian ($U^B \sim D/a \sim kT/6\pi\eta a^2$) to 'driven' motion ($U^F \sim F/6\pi\eta a$) gives the Péclet number $Pe = Fa/kT$ and governs the behavior of the system. Here, D is the Stokes-Einstein diffusivity of a single particle of radius a and thermal energy kT in a fluid of viscosity η. (Alternatively, the probe particle may be dragged with a constant velocity U, in which case $U^F = U$ and $Pe = Ua/D$.)

By contrast, much less work has been done on active microrheology, where the tracked particle is driven by an external force (e.g., the experiments of Habdas and coworkers [15] and the theoretical work of Brady and coworkers [18, 23]). By its very nature the passive regime is limited to studying the *linear* viscoelastic behavior of the material, while the active regime can be used to drive the system out of equilibrium and investigate the material's *nonlinear* response. In many situations, materials are often subjected to strong flows and large deformations, and therefore it is important to know and understand the nonlinear behavior. Macroscopic rheology takes this into account: viscosities and other material properties of complex fluids, including colloids (e.g., [4]), are measured under varying conditions (shear rates, etc.) to determine the complete behavior. It is the purpose of this work to numerically study active microrheology and the transition from linear to nonlinear behavior. We shall do this using a model complex fluid—a colloidal dispersion—given the availability of complementary results in the colloids literature. Furthermore, we are interested in how far one may extend the comparison between the micro and macro measurements, given the obvious differences between the forcings employed in these methods.

In microrheology experiments, the displacement of a probe particle can be induced through the use of magnetic fields and optical tweezers, or alternatively, by having a heavy particle suspended amidst a sea of neutrally-buoyant particles. The basic problem reduces to examining the motion of a single particle under the action of an imposed external force and how this motion is affected by the response of the material. As the probe moves, it disturbs the local medium, which relaxes through thermally-driven motion. Here, we investigate perhaps the simplest viscoelastic fluid—a dispersion of colloidal particles suspended in a Newtonian solvent. The basic problem is illustrated in Figure 4.1. We chose to study active microrheology using Brownian dynamics (BD) simulations. These are particle-level simulations—the dispersion is treated as a collection of spheres in a Newtonian fluid. The particles are monodisperse hard spheres (no overlap or deformation of particles is allowed). Each individual colloidal particle is subject to viscous drag and Brownian motion, but we choose to ignore (for this study) fluid-mediated (hydrodynamic) interactions between the particles. The benefits of simulations are twofold: first of all, they provide a means of checking and extending theoretical analyses, and secondly, they allow us to analyze experimental systems in which different effects can be cleanly separated. Although the removal of hydrodynamic interactions may appear to be a harsh assumption, it can be achieved experimentally with particles subject to a repulsive potential that prevents them from approaching too closely. As Brady and coworkers [4, 18] have noted, even a small difference between the effective and the hydrodynamic radii can strongly decrease the effect of hydrodynamic lubrication interactions.

Because the probe's motion is no longer purely Brownian in active microrheology, the probe particle has an average displacement and therefore an average velocity, from which we can *define* an effective microviscosity of the dispersion through the use of Stokes drag law. This microviscosity is a function of the Péclet number—the ratio of the imposed motion to the thermal motion—and the volume fraction of the freely suspended bath particles. The results of a series of BD simulations are detailed in §4.4. The microviscosity exhibits a Newtonian plateau for low Péclet numbers, force-thins as the Péclet number is increased, and finally reaches a second plateau region for high Péclet numbers. The microviscosity is also an increasing function of volume fraction, and a simple theory by Squires and Brady

[23] can be used to give appropriate scaling relations that collapse the effective viscosities at different suspension volume fractions and Péclet numbers onto a single universal curve (a brief overview of the dilute theory is given in §4.3). The dispersion with the highest volume fraction (55%), displays yield behavior, and the simple scaling arguments of Squires and Brady [23] only apply at the highest Péclet numbers studied where the motion of the probe 'liquefies' the material in its immediate neighborhood. For small Pe the system is solid-like. We also address the difference in the measurements when the probe is dragged with a constant force versus a constant velocity. These two cases result in different effective viscosities—when the particle is dragged with a constant velocity, the probe cannot move laterally as it passes suspended particles, the suspension is more dissipative and the effective viscosity calculated is higher than for the equivalent constant force measurement. The use of multiple probe particles can also disturb the measurements, as (even in the absence of hydrodynamic interactions) probes can affect each other through the microstructural deformation caused by their motion. The last part of our study involves the interactions between pairs of probe particles, wherein we find that probes can attract or repel each other depending on their separation and relative orientation.

One of the central issues in the use of microrheology is the relation between the microviscosity and the macroviscosity—the viscosity measured in a conventional macroscopic rheometer—, and therefore one of the key goals of this study has been to compare our microviscosity results to the results obtained for a homogeneously sheared suspension. A direct comparison can be made to the simulation work of Foss and Brady [11] who conducted BD simulations of suspensions at some of the same volume fractions as used in this study. In the BD simulations of Foss and Brady [11] a simple shear flow is applied and a shear viscosity (defined in the standard way) obtained, which is dependent on the volume fraction and Péclet number, which for their problem is defined as a ratio of shear to thermal forces. We find that the results for the shear viscosity (both theory and simulations) and the microrheology results agree qualitatively, and almost quantitatively when appropriately interpreted (allowance made for the obvious volume fraction difference in their definitions)—the micro- and macroviscosities both exhibit a force/shear-thinning region and a high Péclet number Newtonian plateau. We conclude in §4.5 with some final remarks and suggestions for future work.

4.2 Brownian dynamics simulation method

The problem we address is that of a single 'probe' particle moving through a surrounding colloidal dispersion with either a constant force or a constant velocity, as illustrated in Figure 4.1. While the detailed interparticle interactions and chemistry are often important for specific systems, the most basic property of a complex fluid is a microstructure that can be deformed by an external probe and which returns to equilibrium by thermal motion. The simplest system that captures this basic essence is a colloidal dispersion of neutrally-buoyant monodisperse hard spheres. For microrheology the 'probe' particle can be the same as any other colloidal particle (for simplicity the probe and background particles in this study are the same size; in experiments the sizes are often different), and without any external forcing, its motion is simply diffusive. However, when its motion is driven by an external force, so that it is no longer completely thermal, the probe can drive the surrounding microstructure out of equilibrium, and thereby transitions from passive to active microrheology and from linear to nonlinear behavior.

Brownian dynamics (BD) can be used to simulate colloids at the particle level. The size of colloidal particles is such that there is a clear separation of time and length scales between the particles and the fluid molecules—therefore the fluid can be treated as a continuum—but the particles are still small enough to be affected by collisions with the fluid molecules and are thus Brownian. The BD method is well-established and has been investigated and expanded by various researchers (a further description of BD and relevant references are given in [1]). Our approach is similar to that used by Foss and Brady [10] for sheared colloidal dispersions.

The motion of the individual particles is governed by the Langevin equation—a balance between the hydrodynamic, Brownian, and any other forces that may be present:

$$\boldsymbol{m} \cdot \frac{d\boldsymbol{U}}{dt} = \boldsymbol{F}^H + \boldsymbol{F}^B + \boldsymbol{F}^P. \tag{4.2}$$

Here, $\boldsymbol{m}$ is the generalized mass/moment of inertia tensor, $\boldsymbol{U}$ is the particle velocity vector, $\boldsymbol{F}^H$ represents the hydrodynamic forces on the particles; $\boldsymbol{F}^B$ are the Brownian forces; and $\boldsymbol{F}^P$ represents any other deterministic non-hydrodynamic forces that are present, e.g., hard-sphere and external. For colloidal systems inertia is not important (small Reynolds number) and (4.2) reduces to

$$\mathbf{0} = \boldsymbol{F}^H + \boldsymbol{F}^B + \boldsymbol{F}^P. \tag{4.3}$$

For BD there are no hydrodynamic interactions and therefore the forces in (4.3) are given simply by

$$\boldsymbol{F}^H = -6\pi\eta a \boldsymbol{U}, \tag{4.4}$$

$$\overline{\boldsymbol{F}^B} = \mathbf{0},\ \overline{\boldsymbol{F}^B(0)\boldsymbol{F}^B(t)} = 2kT(6\pi\eta a)\boldsymbol{I}\delta(t),\ \text{and} \tag{4.5}$$

$$\boldsymbol{F}^P = \boldsymbol{F}^{HS} + \boldsymbol{F}^{ext} = 6\pi\eta a \frac{\Delta \boldsymbol{X}^{HS}}{\Delta t} + \boldsymbol{F}^{ext}, \tag{4.6}$$

where η is the solvent viscosity, a is the particle radius, and kT is the thermal energy. The overbars indicate an ensemble average over the thermal fluctuations in the fluid, with the amplitude of the Brownian forcing being given by the fluctuation-dissipation theorem. For microrheology the external force $\boldsymbol{F}^{ext}$ is only applied to the probe particle. The factor $\Delta \boldsymbol{X}^{HS}$ is a displacement due to hard-sphere collisions, which will be discussed further below. For spherical particles in the absence of hydrodynamic interactions, rotation of the particles does not matter.

An integral of (4.3) over the time step Δt gives the non-dimensional displacement equation

$$\Delta \boldsymbol{X} = \Delta \boldsymbol{X}^B + Pe\, \boldsymbol{F}^{ext}\Delta t + \Delta \boldsymbol{X}^{HS}, \tag{4.7}$$

with

$$\overline{\Delta \boldsymbol{X}^B} = \mathbf{0} \text{ and } \overline{\Delta \boldsymbol{X}^B \Delta \boldsymbol{X}^B} = 2\Delta t \boldsymbol{I}. \tag{4.8}$$

Here, time is non-dimensionalized by the characteristic diffusive time, $\tau = a^2/D$, where $D = kT/6\pi\eta a$ is the Stokes-Einstein diffusivity of an isolated particle, length by the particle radius, a, the external force by its magnitude, F, and the Brownian displacement by its characteristic scale, $\sqrt{kT(6\pi\eta a)}$. The relative importance of 'driven' ($U^F \sim F/6\pi\eta a$) to Brownian ($U^B \sim D/a \sim kT/6\pi\eta a^2$) motion is expressed as a Péclet number, $Pe = U^F/U^B = Fa/kT$. For simulations wherein the Péclet number is large ($Pe > 1$), it is appropriate to use a time scale based on the external driving force, $\tau = 6\pi\eta a^2/F$, resulting in a slightly different version of the displacement equation[1]:

$$\Delta \boldsymbol{X} = \frac{1}{\sqrt{Pe}} \Delta \boldsymbol{X}^B + \boldsymbol{F}^{ext} \Delta t + \Delta \boldsymbol{X}^{HS}. \tag{4.9}$$

At each time step the positions of the particles are updated first by adding in the displacement due to the Brownian and the external forces, and second by an iterative method which corrects collisions by applying a hard-sphere force/displacement $\Delta \boldsymbol{X}^{HS}$. This hard-sphere collision scheme is based on the 'potential-free' algorithm of Heyes & Melrose [17] in which the overlap between pairs of particles is corrected by moving the particles equal amounts along the line-of-centers, back to contact. This algorithm is 'potential-free' in that it does not require a specific declaration of a pair potential, although it implements the hard-sphere potential which is infinite if the particles are overlapping and zero otherwise.

The above approach was used to examine the properties of a colloidal dispersion in two cases: with probe particles acting under either an imposed constant force or constant velocity.

4.2.1 Constant force

For the constant force case, a constant in time (although one could impose an arbitrary time-dependence if desired) external force is exerted on the probe particle. From the displacement of the probe we can obtain its average velocity resulting from the applied external force, and this may be used to define an effective viscosity for the suspension from Stokes drag. The probe's mean velocity is given by

$$\langle \boldsymbol{U} \rangle = \frac{\langle \Delta \boldsymbol{X} \rangle}{\Delta t} = \frac{\langle \Delta \boldsymbol{X}^B \rangle}{\Delta t} + Pe \, \langle \boldsymbol{F}^{ext} \rangle + \frac{\langle \Delta \boldsymbol{X}^{HS} \rangle}{\Delta t}, \tag{4.10}$$

---

[1] The two versions of the displacement equation are equivalent. In the following sections, we shall use the low Péclet displacement equation (4.7) to derive further results—it is straightforward to convert these to the high-Péclet analogues.

where the average $\langle\cdot\rangle$ is defined as the average over a time period $M\Delta t$, e.g., $\langle\beta\rangle = (1/M)\sum_{i=1}^{M}\beta(t_i)$. Noting that the average Brownian displacement is zero, $\overline{\langle\Delta\boldsymbol{X}^B\rangle} = 0$, one obtains

$$\langle\boldsymbol{U}\rangle = Pe\,\langle\boldsymbol{F}^{ext}\rangle + \frac{\langle\Delta\boldsymbol{X}^{HS}\rangle}{\Delta t}. \tag{4.11}$$

Returning to dimensional quantities, we *define* an effective viscosity for the suspension from Stokes drag:

$$\frac{\eta_{eff}}{\eta} \equiv \frac{F_x}{6\pi\eta a\langle U_x\rangle}, \tag{4.12}$$

where we have taken x to be the direction of the external force. This effective viscosity is a function of the Péclet number and of the volume fraction of bath particles in the dispersion, $\phi = (4/3)\pi a^3 n$, where $n = N/V$ is the number density of bath particles. In the simulations, the probe is included in the definition of the volume fraction, and therefore there is a $1/N$ 'error' in ϕ (the volume fraction of bath particles is slightly lower). However, as the number of particles N used in the BD simulations is 300 or greater, this deviation is not significant.

4.2.2 Constant velocity

Rather than impose a constant force, one can impose the velocity of the probe and measure the force required to maintain the constant velocity. The dynamics are now somewhat different and the simulations must be performed in a slightly different fashion. From the displacement equation (4.7), we note that in the case of an imposed velocity the probe particle is displaced according to the following rule (all of the other particles are still displaced according to (4.7)):

$$\boldsymbol{X}_{probe}(t+\Delta t) - \boldsymbol{X}_{probe}(t) = Pe\,\boldsymbol{U}\Delta t, \tag{4.13}$$

where now the velocity of the probe, $\boldsymbol{U}$, is known rather than the applied external force, $\boldsymbol{F}^{ext}$. For the probe particle

$$\Delta \boldsymbol{X}_{probe} = Pe\, \boldsymbol{U} \Delta t = \Delta \boldsymbol{X}^{B} + Pe\, \boldsymbol{F}^{ext} \Delta t + \Delta \boldsymbol{X}^{HS}, \tag{4.14}$$

from which the external force necessary to maintain the constant velocity can be determined. The Péclet number is now defined based on the magnitude of the imposed velocity, $Pe = U/U^{B} = Ua/D$. In the imposed velocity problem, hard-sphere collisions between particles fall into two categories: collisions between background particles (no imposed velocity) and collisions between a background particle and the probe particle. The first collision type is the same as before. The second collision type needs to take into account the fact that since the probe is moving with a set velocity, it is the background particle that needs to be displaced the entire amount back to the contact position.

It is straightforward to calculate the average external force $\langle \boldsymbol{F}^{ext} \rangle$ exerted on the probe to keep it moving with a constant velocity $\boldsymbol{U}$

$$\langle \boldsymbol{F}^{ext} \rangle = \boldsymbol{U} - \frac{\langle \Delta \boldsymbol{X}^{HS} \rangle}{Pe\, \Delta t}, \tag{4.15}$$

and from there the effective viscosity is now defined as

$$\frac{\eta_{eff}}{\eta} \equiv \frac{\langle F_x \rangle}{6\pi\eta a U_x}. \tag{4.16}$$

Note that for constant velocity the force required fluctuates as the microstructure changes about the moving probe, while at constant force the probe velocity fluctuates in response to the fluctuating environment.

4.3 Simple theory

Theoretical work on active microrheology includes Squires and Brady [23] (without hydrodynamic interactions between colloidal particles) and Khair and Brady [18] (including hydrodynamics). We shall focus here on the work of Squires and Brady [23] because it provides the theoretical analogue of our simulations. The authors consider a probe particle being dragged with a constant force (or velocity) in a suspension of other colloidal particles. The particles are subject to a hard-sphere potential and hydrodynamic interactions are neglected[2]. When the system is in equilibrium, there is a spherically symmetric probability distribution of encountering bath particles, but this symmetry is lost when the probe is induced to move. The motion of the probe is resisted by the viscous drag of the solvent and by the thermal motion of the surrounding particles: as the probe particle moves, it encounters more particles on its front (forming a zone of increased particle density), and has a trailing wake, a zone of depleted particle density, e.g., see Figure 4.4. This microstructural deformation creates a resistance to the motion of the probe particle: there is an entropic reactive force proportional to the thermal energy and the length scale for the deformed microstructure. Near equilibrium—in passive microrheology—the velocity is linear in the applied force and may be directly related to the long-time self-diffusivity

$$\langle \boldsymbol{U} \rangle = M_{\infty}^{s} \boldsymbol{F}^{ext} = \frac{D_{\infty}^{s}}{kT} \boldsymbol{F}^{ext}, \tag{4.17}$$

where D_{∞}^{s} and M_{∞}^{s} are, respectively, the long-time self-diffusivity and mobility [5].

Squires and Brady [23] also use Stokes drag to define an effective viscosity ($\boldsymbol{F}^{ext} = 6\pi\eta_{eff} a \langle \boldsymbol{U} \rangle$). This definition requires the pair-distribution function $g(\boldsymbol{r})$—the probability density of finding a bath particle at location $\boldsymbol{r}$ relative to the probe—in order to solve for the mean probe velocity $\langle \boldsymbol{U} \rangle$, and the authors assume that the suspension is dilute in order to obtain analytic solutions. They define the 'viscosity increment' as

$$\Delta\eta = \eta_{eff} - \eta, \tag{4.18}$$

removing the solvent contribution. This viscosity increment effectively captures the contribution due to the microstructural deformation, and therefore should convey the same underlying physics as the

---

[2] Note that the inclusion of hydrodynamics does not qualitatively change the behavior of the effective microviscosity in the low Péclet regime, but does qualitatively change its behavior in the high Péclet regime, resulting in 'force-thickening' of the effective microviscosity in this region [18]. This is reminiscent of the behavior of sheared suspensions and the transition from shear-thinning to shear-thickening at high shear rates [4].

equivalent macroscopic measurement (the macroviscosity increment). One of the main results of this study is that the system 'force-thins', i.e.,

$$\lim_{Pe \to 0} \frac{\Delta\eta}{\eta} = 2 \lim_{Pe \to \infty} \frac{\Delta\eta}{\eta}, \tag{4.19}$$

similar to the 'shear-thinning' found in sheared colloidal suspensions [4]. Squires and Brady [23] extend their study to a comparison between the constant force and constant velocity probes, and conclude that the two cases are different (the effective viscosity is twice as large when dragging the probe with a constant velocity than with a constant force). In addition, they analyze the effect of the size ratio (probe versus bath particles) and compute fluctuations in the probe motion. In the next section we compare the (finite volume fraction) simulation results to the results given by the dilute theory and use the theory as a guide in scaling the simulation results.

4.4 Simulation results

The active microrheology problem is illustrated in Figure 4.1: a single probe particle the same size as the bath particles is pulled through a colloidal dispersion. [The two-particle studies use two 'probes' which are dragged with a constant velocity.] Although BD simulations are computationally less intensive than Stokesian Dynamics and its derivatives, which include hydrodynamic interactions, the BD simulations can still be time-consuming. In particular, factors such as volume fraction and the number of particles in the simulation cell can lead to a wide variation in computational time. Moreover, because we are interested in measuring the probe's average velocity, and we only have one probe particle per simulation run, long and/or multiple runs are required to obtain good accuracy. Recall that for a time average done over a period of M time steps, we have M velocities (for the probe particle) to average, which is a factor of N smaller than if we were allowed to average over all N particles in the simulation cell[3]. Typical

---

[3] To obtain the average velocity, an initial time is subtracted from the run—the time it takes the system to reach steady-state—and then a moving average ($\langle\beta\rangle = (1/M)\sum_{i=\zeta}^{M+\zeta-1} \beta(t_i)$) is performed over the rest of the run, with the time period $M\Delta t$ typically equal to 1000 simulation time units. The moving averages are then averaged together to obtain the final average, as well as the deviation from the average.

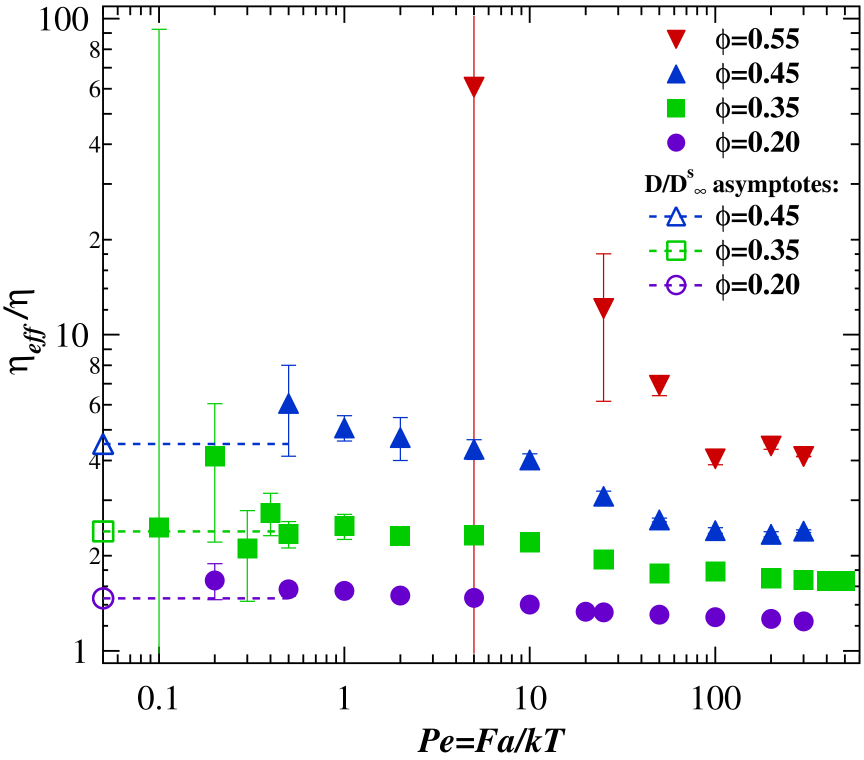

Figure 4.2: The effective microviscosity for a constant force probe, $\eta_{eff}/\eta = F_x/6\pi\eta a\langle U_x\rangle$, plotted against the Péclet number for different values of the suspension volume fraction. The open symbols/dashed lines represent the $Pe \rightarrow 0$ asymptotes ($\eta_{eff}/\eta = D/D^s_\infty(\phi)$) for volume fractions of 20%, 35%, and 45% respectively [D^s_∞ data was obtained from separate pure Brownian ($Pe = 0$) simulations].

runs are for 5000 simulation time units ($\tau = a^2/D$ for $Pe \leq 1$ or $\tau = 6\pi\eta a^2/F$ for $Pe > 1$) or longer. Many of the simulations were done with 300 particles, with higher Péclet number runs often requiring longer simulation cells (and correspondingly more particles) in order to accommodate the microstructural deformation caused by the probe. Although the particles do not interact hydrodynamically, a probe particle can affect itself due to the periodicity of the simulation cell through a long-ranged deformation of the surrounding microstructure[4]. It is important to be aware of this effect and to size the simulation cell accordingly (see Figure 4.4).

4.4.1 Constant force

Simulations were done for a range of volume fractions, $0.20 \leq \phi \leq 0.55$, and Péclet numbers, $0.1 \leq Pe = Fa/kT \leq 500$, so as to study the effects of the Péclet number and the volume fraction upon the effective microviscosity measured in active microrheology. Figure 4.2 shows the effective microviscosity (as given by (4.12)) plotted against the Péclet number—the dimensionless force with which the probe is being pulled—for the volume fractions studied: 20%, 35%, 45%, and 55% (see also Figure 4.3). The low Péclet number asymptotes, from (4.17), are also shown for $\phi \leq 0.45$. The long-time self-diffusivity (D^s_∞) data was independently obtained from separate pure Brownian ($Pe = 0$) simulations. At small Péclet number, for volume fractions $\phi \leq 0.45$, there is a linear relation between the applied force and the velocity resulting in a Newtonian plateau for the microviscosity, and the results approach the passive microrheology limit. The effective microviscosity 'force-thins' as the Péclet number is increased as the probe deforms the surrounding microstructure. This 'force-thinning' in the microrheological context is reminiscent of the shear thinning found in macrorheological measurements of suspensions, and is consistent with the analysis of Squires and Brady [23]. A second Newtonian plateau is achieved at large Péclet numbers.

The effective microviscosity of the dispersion with the highest volume fraction ($\phi = 0.55$) shows a qualitatively different behavior: this suspension appears to yield, resulting in a diverging viscosity for the lower range of Péclet numbers. The freezing point for a hard-sphere suspension occurs at a volume fraction $\phi \approx 0.494$ and the melting point at $\phi \approx 0.545$. It has been argued that such suspensions also undergo a glass transition at a volume fraction between the freezing point and random close packing ($\phi = 0.64$). Our highest volume fraction ($\phi = 0.55$) suspension is in a solid-like state and therefore displays a very different behavior from that at lower volume fractions, which all corresponded to liquid-like states. However, a probe moved with a strong force (high Pe) is able to 'melt' its local environment, and thus the effective viscosity found at high Pe for $\phi = 0.55$ starts to behave in a manner similar to that at lower volume fractions.

One can gain a qualitative impression of the suspension behavior through microstructural

---

[4] The probe can leave a 'trail' that is almost free of particles, and the length of this region increases with increasing Péclet number.

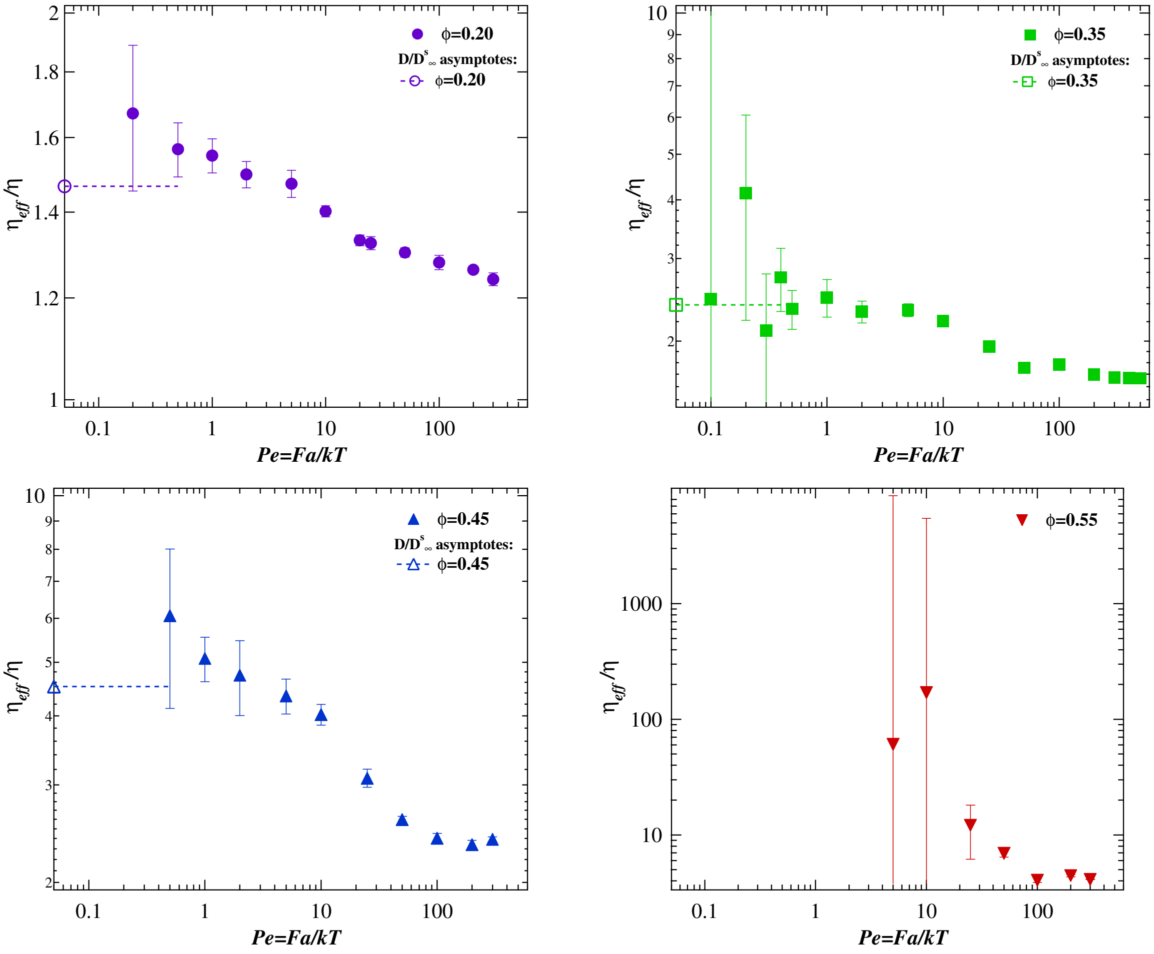

Figure 4.3: The effective microviscosity for a constant force probe, $\eta_{eff}/\eta = F_x/6\pi\eta a\langle U_x\rangle$, plotted against the Péclet number for different values of the suspension volume fraction. The open symbols/dashed lines represent the $Pe \rightarrow 0$ asymptotes ($\eta_{eff}/\eta = D/D^s_\infty(\phi)$) [$D^s_\infty$ data was obtained from separate pure Brownian ($Pe = 0$) simulations].

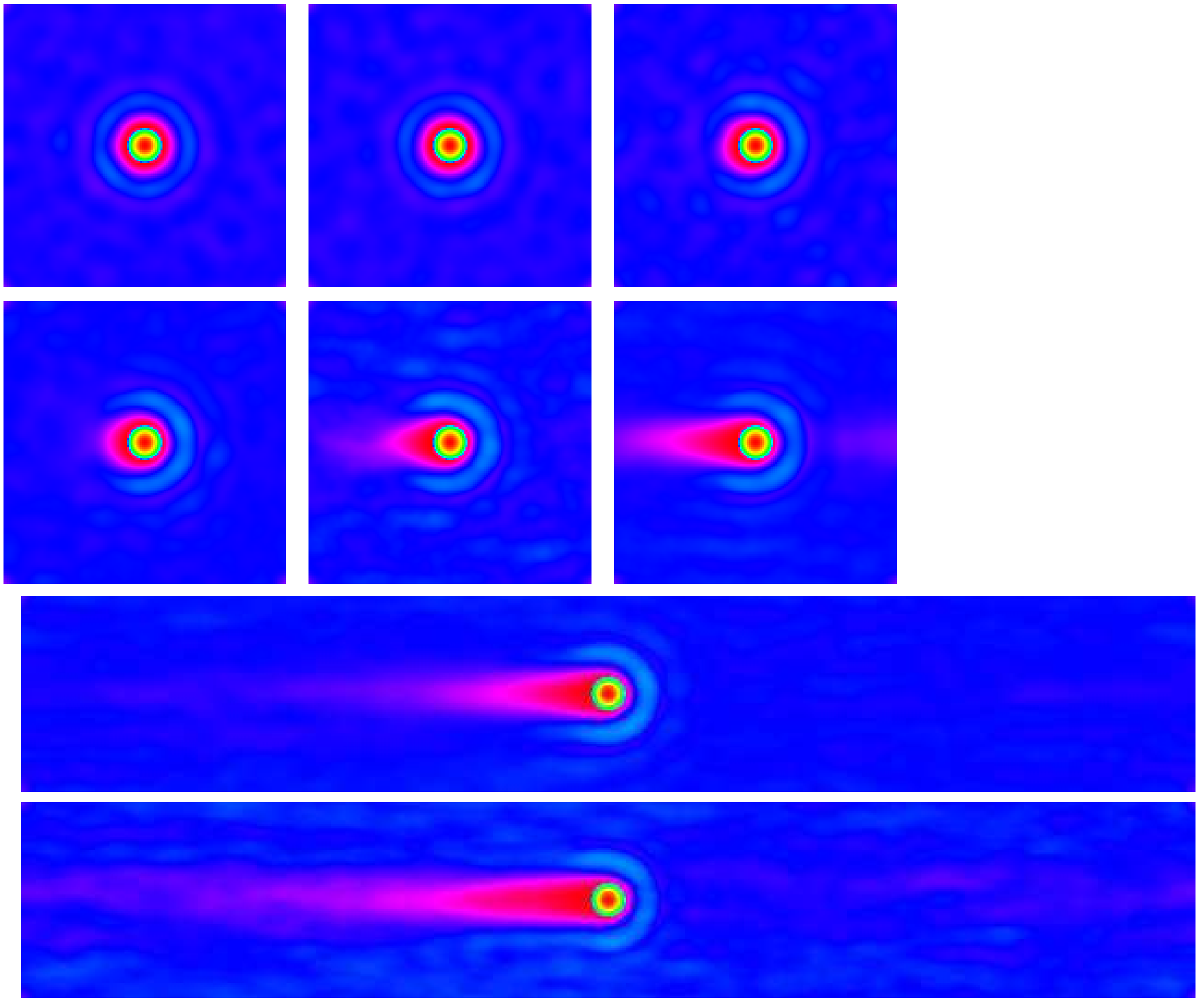

Figure 4.4: Brownian Dynamics results for the average density (the x-y plane projection) around a probe particle pulled with a constant force for $\phi = 0.35$ for different values of the Péclet number. Total number of particles used for the simulations is 300 for the top six (cubic boxes) and 600 for the bottom two (for which the length/width/height ratio is 6/1/1). From left to right: top row: $Pe = 0.1, 1, 5$; second row: $Pe = 10, 25, 50$; third row: $Pe = 100$; bottom row: $Pe = 300$. The images have been processed to improve contrast—the green denotes the edge of the probe particle, with the light blue denoting higher density areas and the red/magenta denoting lower density areas.

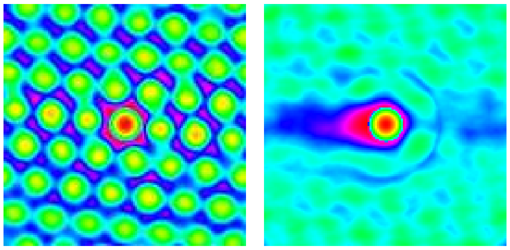

Figure 4.5: Brownian Dynamics results for the average density (the x-y plane projection) around a probe particle pulled with a constant force for $\phi = 0.55$ at $Pe = 5$ and $Pe = 100$. The number of particles used in the simulation cell is 300. The images have been processed to improve contrast.

density profiles relative to the probe (see Figures 4.4 and 4.5). The pictures shown are time averages of the particle density around the probe (center), projected into the x-y plane (where x is the direction of the force/motion of the probe) with the density averaged over the z direction. Close to equilibrium, a probe in a 35% volume fraction suspension is almost equally likely to find a bath particle in any direction, characteristic of liquids, thus the ring structure seen in the top row of Figure 4.4. However, at the highest volume fraction ($\phi = 0.55$) this is no longer the case (Figure 4.5, first picture), and the suspension is clearly organized into a solid-like structure.

Figure 4.4 shows the different density profiles relative to the probe for a volume fraction of 35% at different Péclet numbers. For small Pe (top row), Brownian motion is strong enough to minimize the effect of the probe, and the density is almost symmetric (as it would be at equilibrium). The break in symmetry about the probe is clearly seen for $Pe > 1$, with the development of a high particle density layer on the front of the probe particle (a sort of cap formed from bath particles, very clear in Figure 4.5 for the $\phi = 0.55$, $Pe = 100$ case) and a low-density, cometlike wake behind the probe. The 'force-thinning' of the microviscosity is a symptom of this change in the microstructure. The wake grows longer as the Péclet number is increased, reflecting the decreasing ability of thermal/Brownian motion to heal the microstructure. Squires and Brady [23] find that in the high Pe limit, the effect of the probe on the microstructure of the dispersion is strongly localized to a thin convection-diffusion boundary layer of thickness $\delta \sim \mathcal{O}(a/Pe)$ on the front of the probe (in which the pair distribution function $g(\boldsymbol{r})$ is greatly enhanced to a value of $\mathcal{O}(Pe)$) and a trailing wake devoid of bath particles ($g = 0$). The reactive force of the dispersion due to this deformation is $\mathcal{O}(kT/\delta)$, or $\mathcal{O}(kT/a \times Pe)$—as large as the driving force!—resulting in a finite value for the microviscosity in the limit of $Pe \to \infty$.

For $\phi = 0.55$, the system is closely packed, solid-like, and displays yield behavior—forces that are too small cannot break the probe particle out of its local 'cage' (see Figure 4.5 and note that the figure for $Pe = 5$ corresponds to the *time-averaged* microstructure relative to the probe—clearly, the probe hops quickly from site to site in the lattice, spending a relatively long time at a lattice site before the next jump). A relatively large force (Péclet number) is required to 'melt' the local microstructure

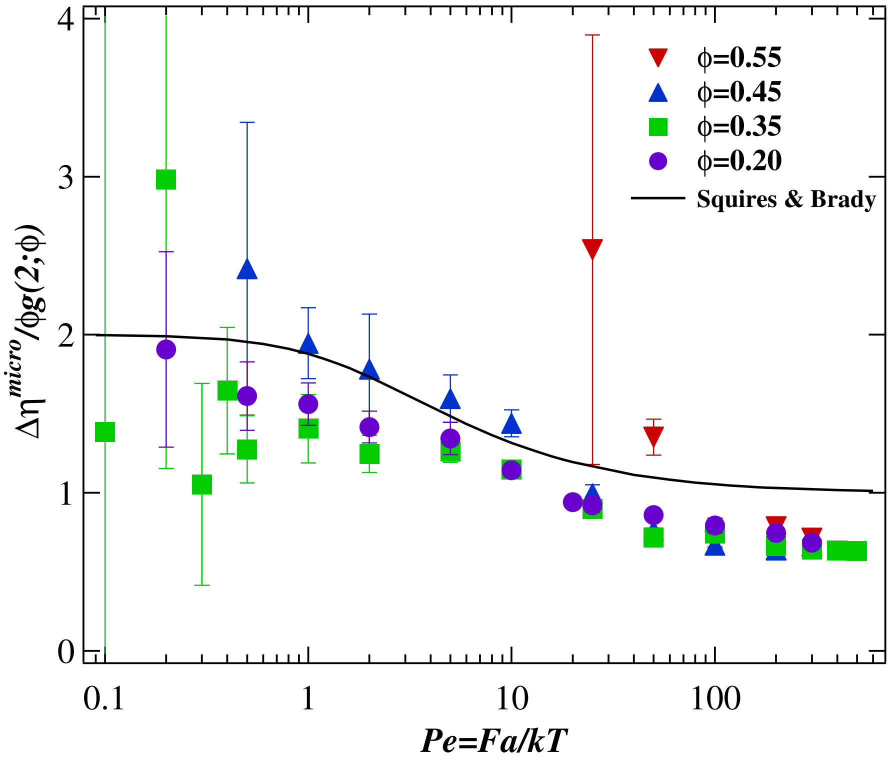

Figure 4.6: The solid symbols give the microviscosity increments, $\Delta\eta^{micro} = (\eta_{eff} - \eta)/\eta$, for the constant force system, scaled by $\phi g^{eq}(2;\phi)$, plotted as a function of the Péclet number. This is the same data as in Figures 4.2 and 4.3, rescaled. The solid curve gives the corresponding (dilute) theoretical prediction from Squires and Brady (2004).

and allow the probe to break free. This behavior is very interesting and is in accord to the observations of Habdas and coworkers in their experiments [15], in which they studied the behavior of colloids close to the glass transition. This type of yield behavior cannot be predicted by the simple analytical theories used to date (which treat the system as liquid-like), but is captured in the simulations. Note that no effort was made to study the effects of the direction of the external force relative to the suspension lattice on the motion of the probe.

From Figure 4.2, we see that the volume fraction can have a very strong effect upon the effective microviscosity: the data spans two orders of magnitude. It is desirable, if possible, to scale out the volume fraction dependence and obtain an universal curve that is independent of ϕ, as this would eliminate the necessity of making measurements at every volume fraction of interest. In the passive microrheology regime, Brady [5] showed that the microviscosity is inversely proportional to the long-time self-diffusivity; D/D^s_∞ are the asymptotic limits at small Pe in Figure 4.2. Further, Brady [5] proposed a simple model for D^s_∞:

$$D^s_\infty \simeq D^s_0(1 + 2\phi g^{eq}(2;\phi))^{-1}, \tag{4.20}$$

where D^s_0 is the short-time self-diffusivity, which in the absence of hydrodynamic interactions is just the isolated particle Stokes-Einstein diffusivity D, and $g^{eq}(2;\phi)$ is the equilibrium value of the pair-distribution function at particle-particle contact, which can be found from the Carnahan-Starling equation of state:

$$g^{eq}(2;\phi) = \frac{1 - \frac{1}{2}\phi}{(1-\phi)^3},\ \phi \leq 0.50. \tag{4.21}$$

At high volume fractions, the long-time self-diffusivity behaves as $D^s_\infty/D^s_0 \sim (\phi g^{eq}(2;\phi))^{-1}$, and as the volume fractions used in our simulations enter this range, we shall use this as our scaling for the microviscosity [although the Carnahan-Starling equation applies for $\phi \leq 0.50$, we use the same formula for $\phi = 0.55$—the value obtained is close to the one found for the metastable fluid branch using molecular dynamics by Rintoul and Torquato [22], 7.96 from Carnahan-Starling versus 8.22 from simulations]. Physically, the term $\phi g^{eq}(2;\phi)$ gives the number of particles contacting the probe.

In addition to scaling the effective viscosity we must also consider scaling the Péclet number, which was defined based on the characteristic probe speed U^F and Brownian speed $U^B = D/a$, and may therefore also be affected by the volume fraction. At low Pe the response time of the microstructure to damage caused by the probe, which is on the scale of the particle radius a, scales with the long-time self-diffusivity, $\tau \sim a^2/D^s_\infty(\phi)$. From our previous discussion, the mean velocity of the probe scales as $D^s_\infty(\phi)F/kT$, and therefore the Péclet number is independent of the volume fraction, i.e. $Pe = Fa/kT$, at least for Pe up to order unity. For high Péclet number, however, the main contribution to the reactive force, and therefore to the microviscosity, occurs in a thin boundary layer whose length scale is $\delta \sim a/Pe$. In this case the response time of the microstructure depends on the time to diffuse this small length, which is governed by the short-time self-diffusivity, D^s_0, rather than the long-time self-diffusivity. The velocity of the probe is given by the product of the mobility and the difference between the external force

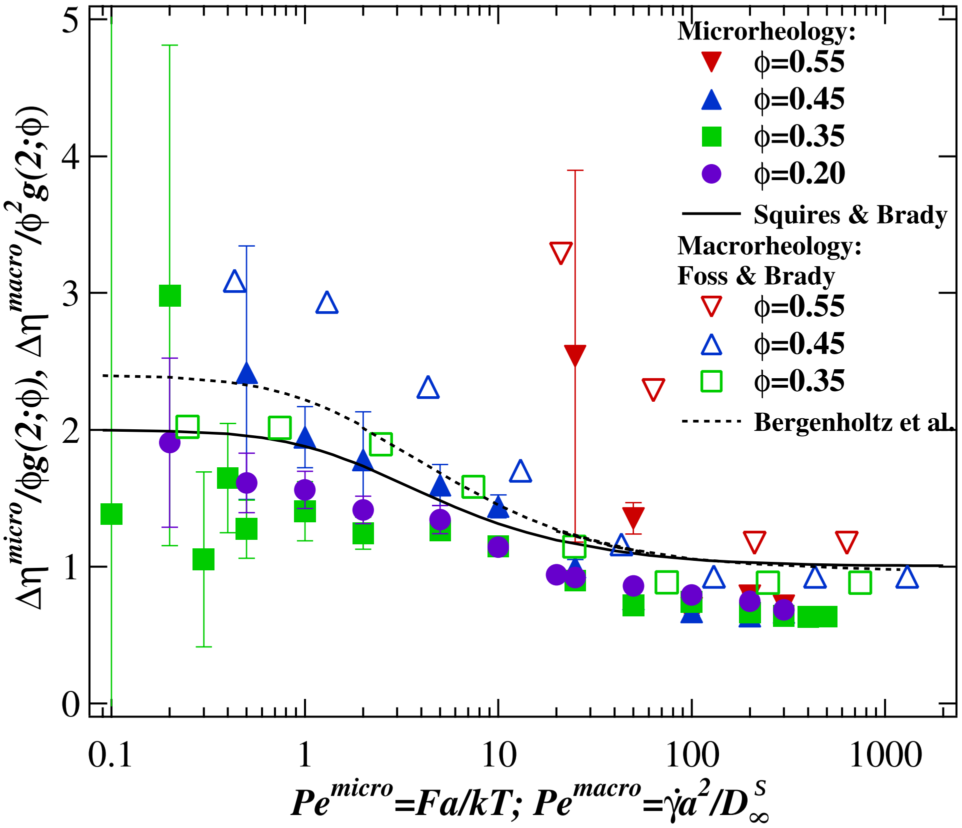

Figure 4.7: The solid symbols give the microviscosity increment $\Delta\eta^{micro} = (\eta_{eff} - \eta)/\eta$ for the constant force system, scaled by $\phi g^{eq}(2;\phi)$, plotted as a function of the Péclet number. Shown also are the dilute theory results of Squires and Brady (2004) for the microviscosity (solid line), and the dilute theory results of Bergenholtz and coworkers (2002) (dashed line) and BD simulation results of Foss and Brady (2000) (open symbols) for the macroviscosity.

and the reactive Brownian force (due to the deformation of the microstructure). At high Pe, the reactive Brownian force is proportional to the number of bath particles which collide with the probe $\phi g(2; \phi)$ (and $\phi g(2; \phi) \sim Pe\, \phi g^{eq}(2; \phi)$), and is therefore of the same order of magnitude as the driving force. This results in a mean velocity of the probe that scales as $U^F \sim (F/6\pi\eta a)[1 + C\phi g^{eq}(2; \phi)]^{-1}$, where C is an $\mathcal{O}(1)$ constant. Therefore, the correct Péclet number in the strong external forcing regime is given by $Pe = (Fa/kT)/(1 + C\phi g^{eq}(2; \phi))$, i.e., the rescaled Péclet number is a function of the volume fraction. The factor $\phi g^{eq}(2; \phi)$ varies from 0.35 to 2.09 for most of the range of volume fractions considered in this study (4.5 for the 55% system); the combination $(1 + C\phi g^{eq}(2; \phi))$ thus may give a weak to moderate dependence on volume fraction. Furthermore, this will just cause a lateral shift in the data at high Pe where they are already in the high-Pe Newtonian plateau and therefore would be hard to discern. Thus, we shall not scale the Péclet number with ϕ at high Pe. The scaling of the Péclet number and the microviscosity is discussed in more detail by Squires and Brady [23].

Although the effective microviscosity of the suspension contains a contribution from the solvent, the relevant contribution is that caused by the microstructural deformation. Therefore we define the microviscosity increment $\Delta\eta^{micro}$ as

$$\Delta\eta^{micro} = \frac{\eta_{eff}}{\eta} - 1, \tag{4.22}$$

in order to focus on the effect of the microstructure. In Figure 4.6 we plot the microviscosity increment scaled by $\phi g^{eq}(2; \phi)$, as a function of the (unscaled) Péclet number. This scaling provides an impressive collapse of the data—note that the scaled viscosity is now on a linear, rather than logarithmic, scale—which shows the features observed before: low and high Péclet number Newtonian plateaus and force-thinning at intermediate values of the Péclet number. In addition, we can see that even the high volume fraction data ($\phi = 0.55$), joins the universal curve at high Péclet number. At this point, the force on the probe becomes strong enough to locally melt the microstructure and thus the suspension behaves (locally) as a liquid. Plotted also is the dilute theory prediction of Squires and Brady [23] (solid line). Qualitative and quantitative agreement between the scaled microviscosity increments is excellent for all volume fractions (other than $\phi = 0.55$).

One of the main goals of this study is to compare micro- and macrorheological measurements. Figure 4.7 shows the scaled microviscosity simulation data together with the dilute microrheology theory prediction (solid line) of Squires and Brady [23], compared to data from both dilute theory [4] (dashed line) and BD simulation results at matching volume fractions [11] (open symbols) for the macroviscosity. The shear viscosity increment, $\Delta\eta^{macro} = \eta^{macro}/\eta - 1 - 2.5\phi$ (both the solvent and Einstein's single-particle viscosity correction are removed), is plotted against a Péclet number based on the shear rate, $Pe = \dot{\gamma}a^2/D^s_\infty$, where $\dot{\gamma}$ is the shear rate, and the long-time self-diffusivity is the appropriate diffusivity for the microstructural relaxation[5]. In addition, the microviscosity increment is $\mathcal{O}(\phi)$, while the macroviscosity increment is $\mathcal{O}(\phi^2)$, and this has been taken into account when scaling the data. Qualitative (and perhaps even quantitative) agreement between the micro and macroviscosity increments is very good. At low Péclet numbers (low shear, low force) both display a Newtonian plateau; as the Péclet number is increased, the viscosity decreases—force-thinning in the microrheology case and shear-thinning in the macrorheology case—until a second Newtonian plateau is reached at high Péclet numbers. While this nearly quantitative agreement only applies to the viscosity increments, these reflect the underlying microstructural dynamics responsible for force or stress. Therefore, even though the micro- and macroviscosities are fundamentally different and correspond to distinct forcings, the viscosity increments evidently reflect the same microstructural physics.

4.4.2 Constant velocity simulations

The comparison in Figure 4.7 is not proper in the sense that the microrheology data is measured at fixed force, while the macrorheology data is at fixed shear rate. The correct comparison should be done between the fixed velocity and the fixed shear rate systems, or between fixed force and fixed stress. In macrorheology to leading order in ϕ (at the pair-level) the viscosity measured at fixed stress is the same

---

[5] In macrorheology, as in microrheology, at high Péclet number there is a boundary layer at particle-particle contact that is responsible for the high Pe Newtonian plateau in the viscosity. The relaxation time for the boundary layer, and hence the stress, is governed by the short-time self-diffusivity, which in the absence of hydrodynamic interactions is just the isolated particle value. Thus, the Péclet number should not be scaled with ϕ at high Pe as was done in figure 4.6. This would cause an indiscernible lateral shift in the data at high Pe and therefore has not been done in the figure.

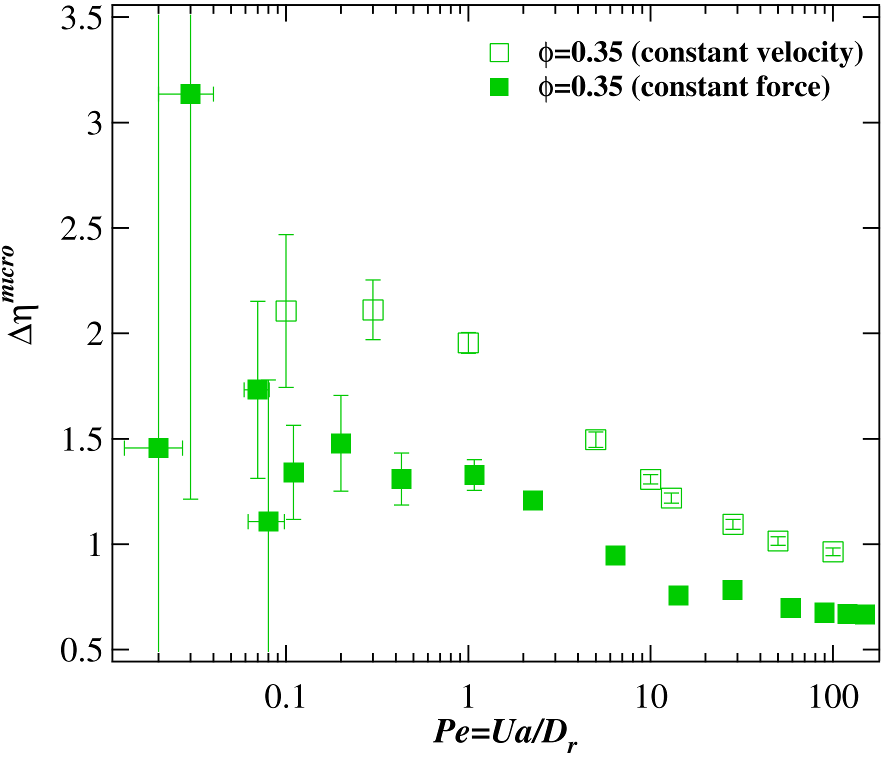

Figure 4.8: The viscosity increment of the constant velocity system (effective viscosity minus the solvent contribution, where $\eta^{eff}/\eta = \langle F_x \rangle / 6\pi\eta a U_x$), plotted against the velocity-based Péclet number $Pe = Ua/D_r$ for a suspension volume fraction of 35%. Also shown is the equivalent constant force data.

as at fixed shear rate, and it is therefore acceptable to compare to the dilute macrorheology theoretical prediction. However, even at the pair level the two microrheology systems are different. Squires and Brady [23] have shown that the effective microviscosity in the constant velocity case is larger than in the constant force case (they predict a factor of 2 difference for equal-sized probes and bath particles), essentially since at fixed velocity the probe must push its way past all the bath particles, while at fixed force it can move sideways if necessary to get past a bath particle, and thereby experience less resistance. Almog and Brenner [2] also found a difference for falling-ball rheometry ($Pe \to \infty$).

In Figure 4.8 the microviscosity increment obtained in the constant velocity case is plotted along with the constant force results for a volume fraction of 35%. As mentioned in §4.2.2, the Péclet number for the constant velocity case is defined based on the imposed velocity rather than the force, $Pe = Ua/D$. We use the relative diffusivity between the bath and the probe, D_r, which is simply the Stokes-Einstein diffusivity for an isolated particle in the constant velocity case (only the bath particles diffuse), and twice that in the constant force case. The constant force data is also plotted as a function of a velocity-based Péclet number, using the calculated average velocity of the probe. The qualitative behavior is the same in both cases. The main difference is quantitative—the constant velocity system is more dissipative as the probe has to force every bath particle it encounters away, which requires a stronger push than the equivalent constant force probe. The ratio of viscosity increments is approximately 3/2 over the entire range of Péclet numbers, slightly lower than the factor of 2 predicted by the dilute theory.

As a final note, it is clear in microrheology that constant force and constant velocity probing are fundamentally (and observably) different. This then raises the question in macrorheology as to whether constant shear rate and constant stress experiments are also different. It has generally been assumed that the viscosities determined from the two situations are the same (for homogeneous deformations with no shear banding), and indeed this can be shown to be true in the linear-response regime (small Pe). In the nonlinear regime, however, it has not been proven that constant stress and constant shear rate experiments give the same rheological behavior. The expectation that they do comes from the fact that the shear rate fluctuations that exist in a constant stress experiment should decrease with the

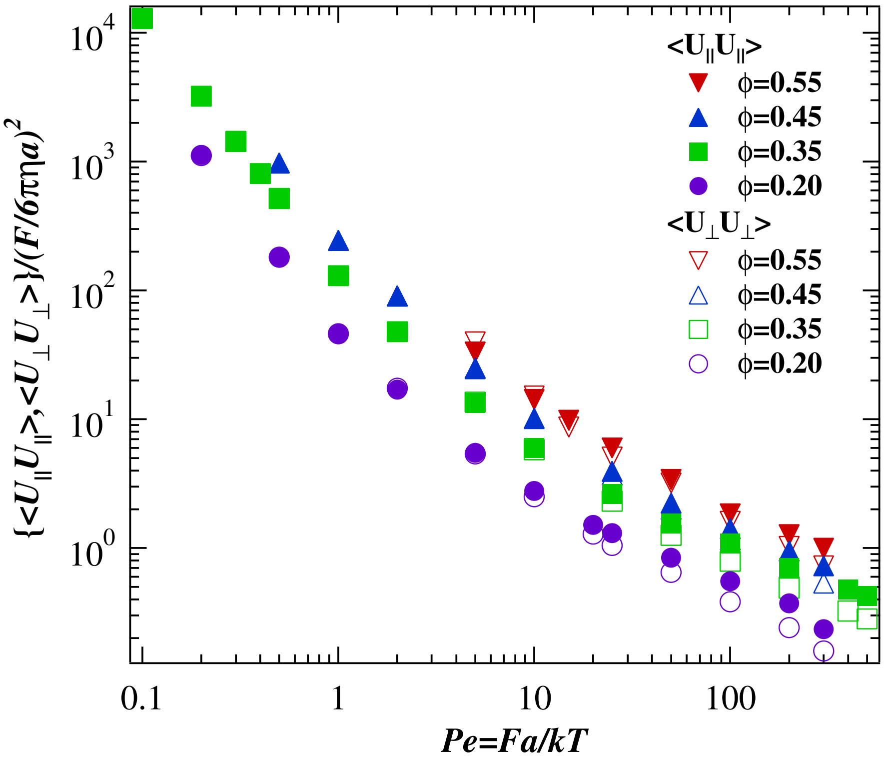

Figure 4.9: The averaged velocity fluctuations for the constant force system plotted against $Pe = Fa/kT$: $U_{\|}$ is the fluctuation in the velocity component parallel to the forcing direction; $U_{\perp}$ is the fluctuation in the velocity component transverse to the forcing direction.

system size and thus vanish in the thermodynamic limit. If the fluctuations do not vanish, say because the system was near a critical point (near a yield stress, for example), then the two situations may be different and their assumed equivalence should be reexamined.

4.4.3 Fluctuations: constant force microrheology

One of the advantages of microrheological techniques is that they allow the study of fluctuations in addition to averages. When the probe particle is much larger than the typical length scale of the surrounding medium, as would be the case for a macrorheology experiment, the velocity fluctuations induced by the surrounding suspension may not be observable. However, if the probe size is comparable to the medium length scale, such fluctuations are important and can be considered as a type of non-continuum effect. For some materials (e.g., living cells and other small or highly heterogeneous systems) the fluctuations

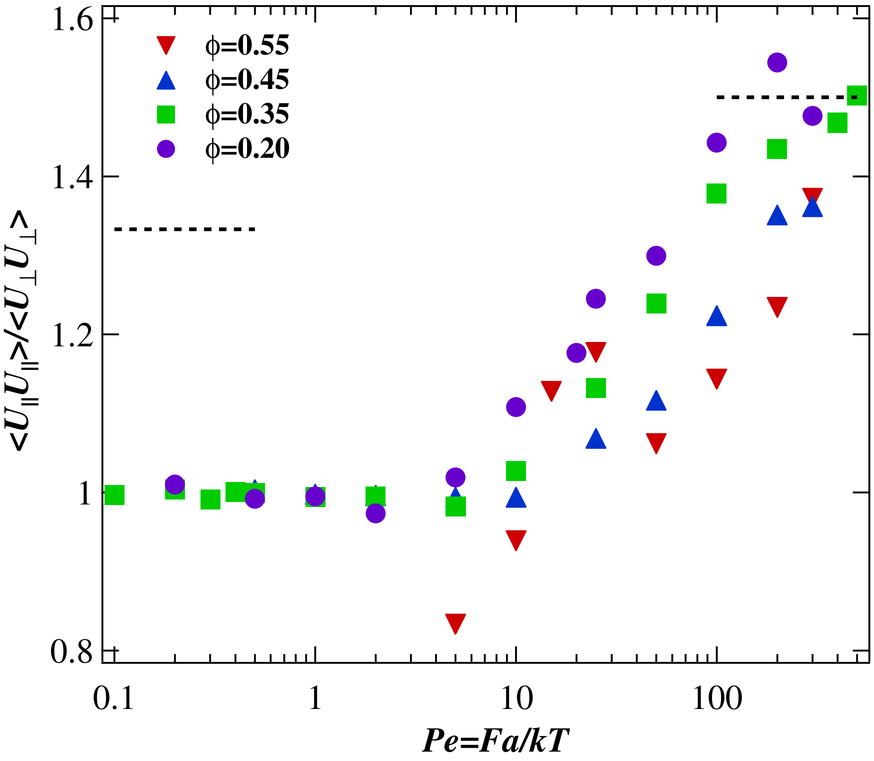

Figure 4.10: The averaged velocity fluctuations for the constant force system plotted against $Pe = Fa/kT$. $U_{\|}$ is the fluctuation in the velocity component parallel to the forcing direction; $U_{\perp}$ is the fluctuation in the velocity component transverse to the forcing direction. The dashed lines are the low and high Pe asymptotic predictions given by the simple dilute theory.

in material properties may play a more significant role than the averages. Although we have not varied the size of our probe for this study, we can examine the behavior of velocity fluctuations as a function of Péclet number and volume fraction. For a constant external force the particle velocity will fluctuate, both in the direction of mean motion and in the transverse directions.

In Figures 4.9 and 4.10, fluctuation results are shown for all volume fractions studied. Here, $U_\|$ is the fluctuation in the velocity component parallel (x) to the forcing direction and $U_\perp$ is the fluctuation in the velocity component transverse (y or z) to the forcing direction. The dimensionless sampling time step is 0.001. The mean squared velocity fluctuations (non-dimensional) are shown in Figure 4.9. In the case of the transverse fluctuations, there is an additional average over the two (identical) transverse directions, i.e. $\langle U_\perp U_\perp \rangle = (\langle U_y U_y \rangle + \langle U_z U_z \rangle)/2$. The mean squared velocity fluctuations decrease with increasing forcing/Péclet number. There does not appear to be any significant difference between the parallel and transverse directions at low Péclet number, but the results at high Pe show some difference, which are clear when we examine the ratio $\langle U_\| U_\| \rangle / \langle U_\perp U_\perp \rangle$ shown in Figure 4.10. The dashed lines in this figure are the asymptotic limits given by the simple dilute theory of Squires and Brady [23]. The increasing anisotropy with increasing Péclet number between the fluctuations oriented parallel versus transverse to the imposed force is clear. At high Pe there is an increased probability of collisions on the 'front' of the probe, and although these will partially contribute to transverse fluctuations (unless the collision is perfectly 'head-on'), they will mainly contribute to parallel fluctuations—leading to the pronounced anisotropy.

The simulation results approach the dilute theory limit for high Péclet numbers, but it is unclear whether the ratio will continue growing or will asymptote to the theory prediction. The relative fluctuations are smaller for low Pe than for high Pe, as the dilute theory suggests, but are lower than the $Pe \ll 1$ theoretical limit. The agreement at high Pe may be due to fluctuations in the $Pe \gg 1$ limit caused mostly by collisions with particles in the high particle density shell on the front of the probe—the boundary layer—, with a clear directionality (on the average) regardless of the overall concentration, whereas in the small Pe limit the directionality of the collisions may be affected by the relatively large

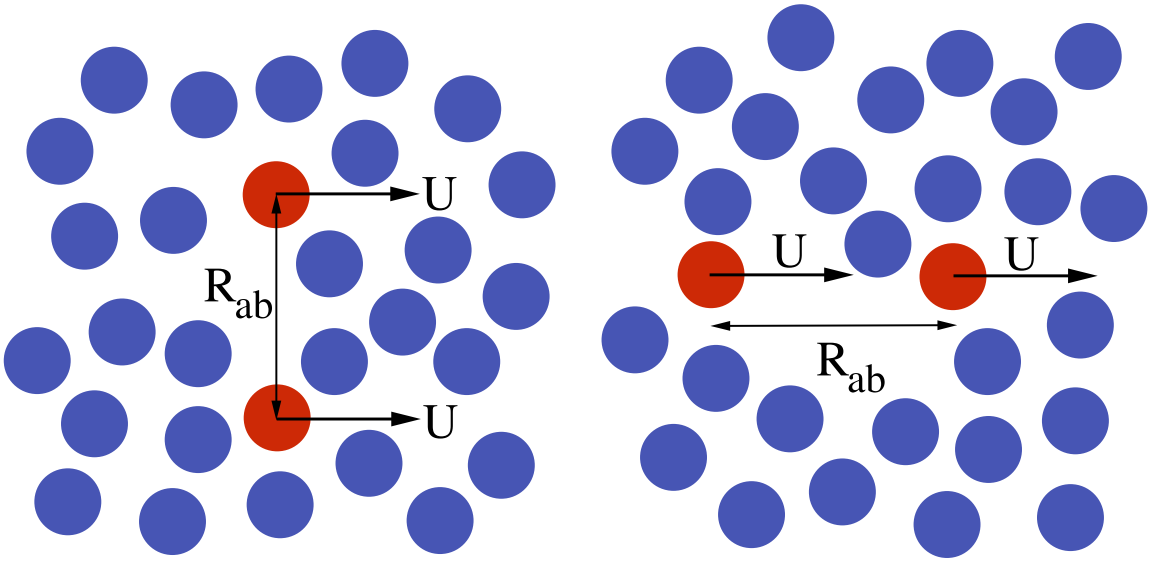

Figure 4.11: The two-particle problem: will two probes separated by some distance R_{ab} between centers experience attractive and/or repulsive interactions? Do probes moving side-by-side interact differently from probes moving in a line (i.e., one probe following the other)?

concentrations present.

4.4.4 Interactions between probes

One can conceive of many interesting variations of these constant-force and constant-velocity problems. In this next section we chose to look at interactions between pairs of probes (see Figure 4.11). We know from the previous analysis that the images of the probe (recall that the simulation cell is repeated in all directions) do not affect the results when the box is big enough. 'Big enough' means that the images are separated by approximately five particle diameters or more in the transverse directions (to the motion), and that the cell is long enough that the particle does not run into its own wake (which involves some trial-and-error design). Therefore we can place two probes close to one another and examine their interactions while neglecting their interactions with their images (given a 'big enough' cell). We choose to study what happens to the interactions between two probes dragged with some constant velocity U (the same for both probes) when the distance between them is such that they are creating an excluded volume (which the surrounding particles cannot enter). We look at three different values of Pe, for distances ranging

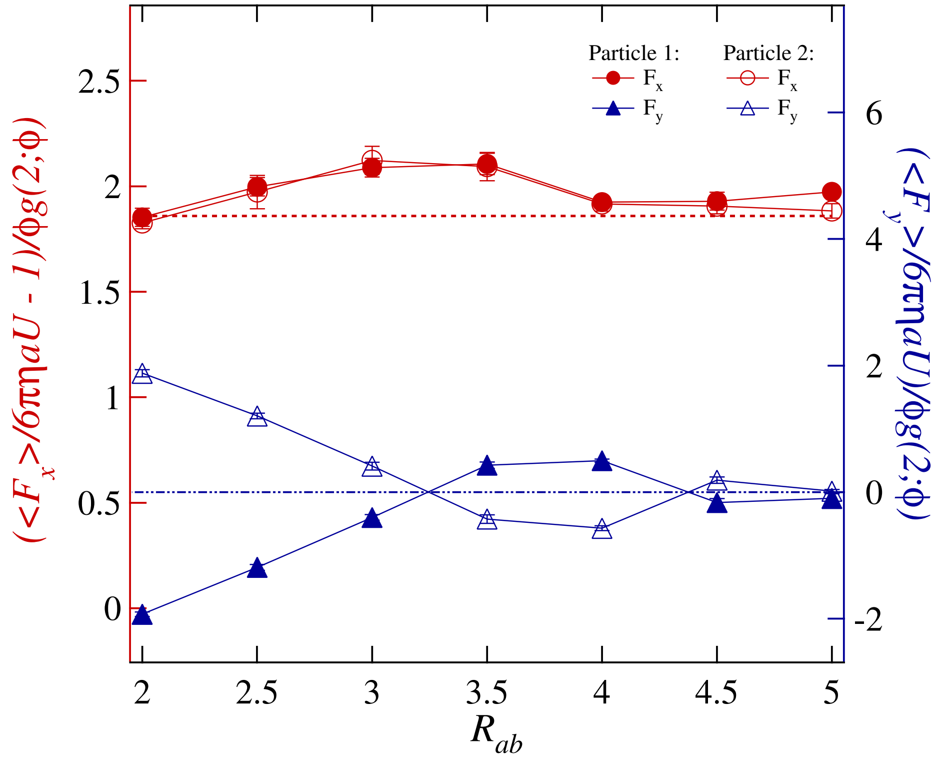

Figure 4.12: $Pe_U = 1$. The two probe particles are dragged with the same velocity, and the distance between their centers is $R_{ab} = \Delta y$ (they are separated in a direction transverse to the direction of travel). $R_{ab} = 2$ corresponds to contact (distances are scaled by the particle radius a). The forces on this graph are the forces one is required to impose on the particle in order to keep it moving with a constant velocity $\boldsymbol{U} = (U, 0, 0)$. A negative F_y therefore implies that the particle is actually experiencing an upward-directed force (and vice versa). Particle 1 is at a lower y than particle 2. The particles are attracted to each other when the separation about a particle radius or less, they repel each other when the separation is between a radius and two radii approximately, and the interaction dies out for longer distances. The force in the direction of travel is only slightly affected (the dashed red line represents the average force obtained in the single probe problem) primarily in the region where the interactions switch from repulsive to attractive.

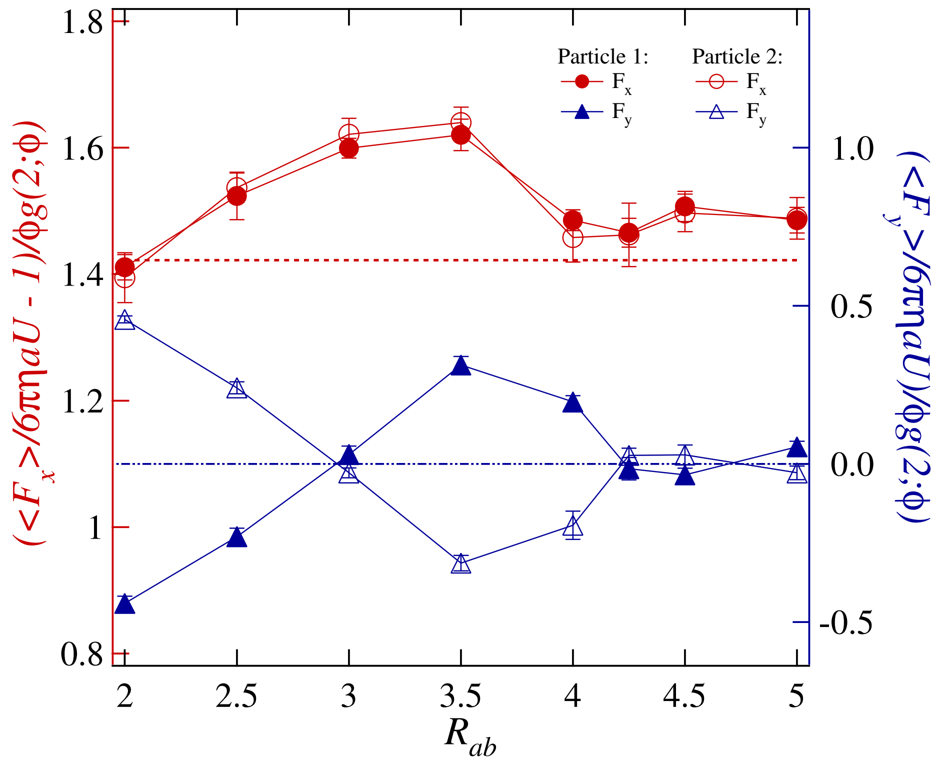

Figure 4.13: $Pe_U = 5$. The particles are attracted to each other when the separation is about a particle radius or less, they repel each other when the separation is between one and two radii approximately, and the interaction dies out for longer distances. The force in the direction of travel is only slightly affected (the dashed red line represents the average force obtained in the single probe problem) primarily in the region where the interactions switch from repulsive to attractive.

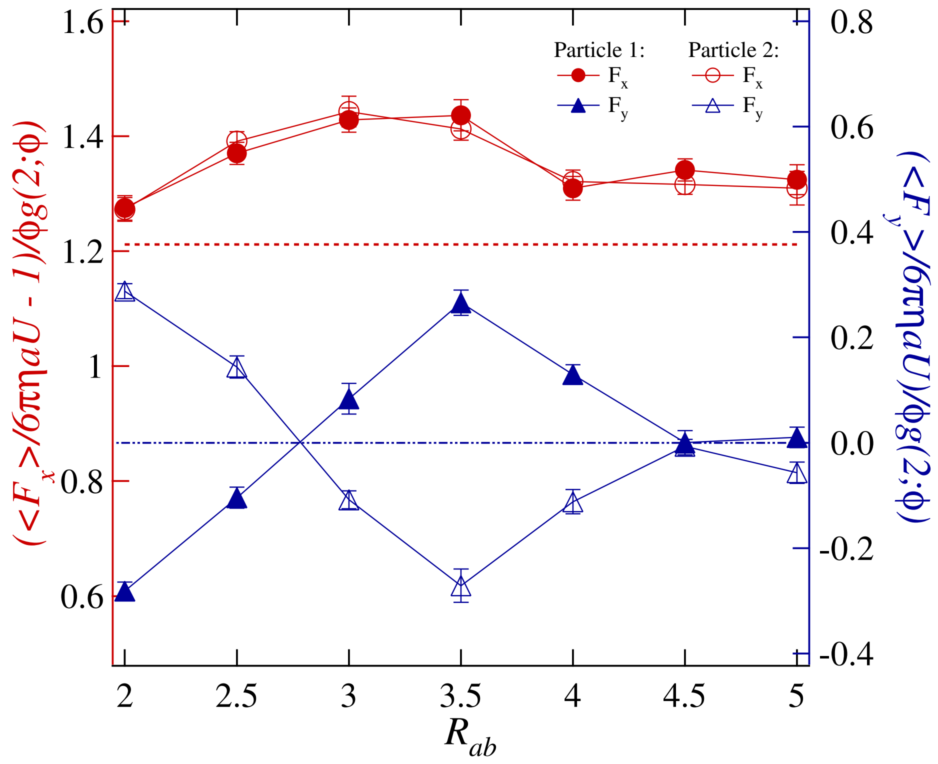

Figure 4.14: $Pe_U = 10$. The particles are attracted to each other when the separation is about a particle radius or less, they repel each other when the separation is between one and two radii approximately, and the interaction dies out for longer distances. The force in the direction of travel is only slightly affected (the dashed red line represents the average force obtained in the single probe problem) primarily in the region where the interactions switch from repulsive to attractive.

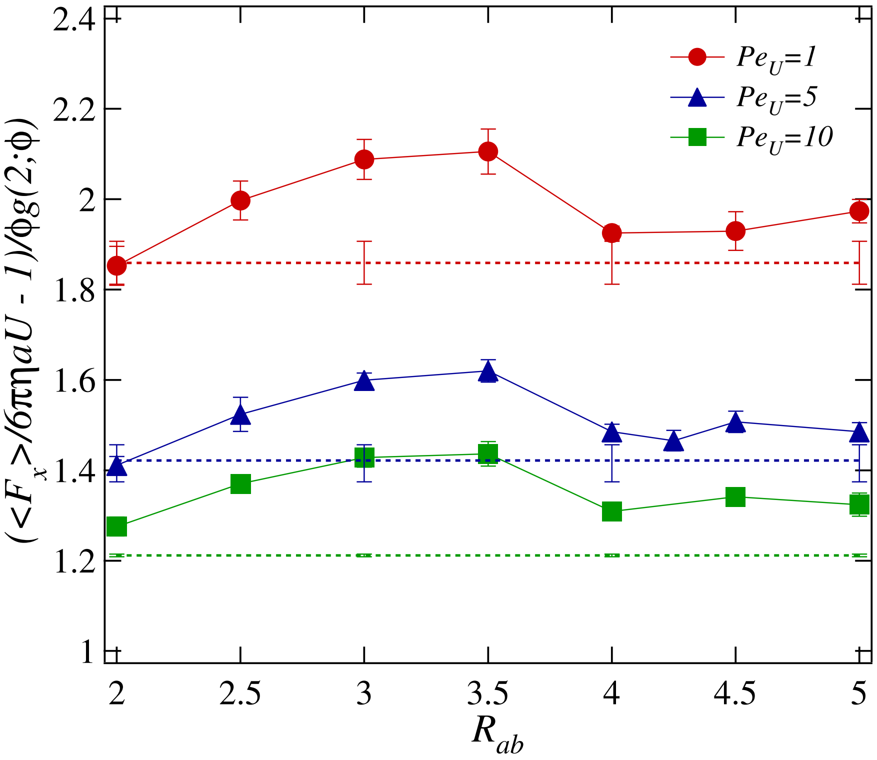

Figure 4.15: A comparison of the forces applied in the x direction for the three different cases of probes separated by $R_{ab} = \Delta y$. Interactions are stronger for the smaller Pe_U, and appear to be slightly longer ranged. The dashed lines represent the respective average forces obtained from the single probe problem.

between contact and three radii apart in the y direction (transverse to motion), and with no relative separation in the other two dimensions. As a reality check, we also test the case of one particle moving behind the other, $R_{ab} = \Delta x$ (no separation transverse to the direction of motion), to test the effect of the wake upon the force required to move the trailing particle.

In Figure 4.12 we see the effect of separation distance upon the forces in the x and y direction. Both probe particles move with the same velocity ($Pe_U = 1$), and the distance between their centers is R_{ab} (in the y direction, transverse to the direction of travel; it is 0 in the direction of travel), with particle 1 ‘beneath’ particle 2. $R_{ab} = 2$ corresponds to contact (distances are scaled by the particle radius). The forces on this graph are the forces one is required to impose on the particles in order to keep them moving with a constant velocity $\boldsymbol{U} = (U, 0, 0)$. A negative F_y therefore implies that a particle is actually experiencing an upward-directed force (and vice versa). The particles are attracted to each

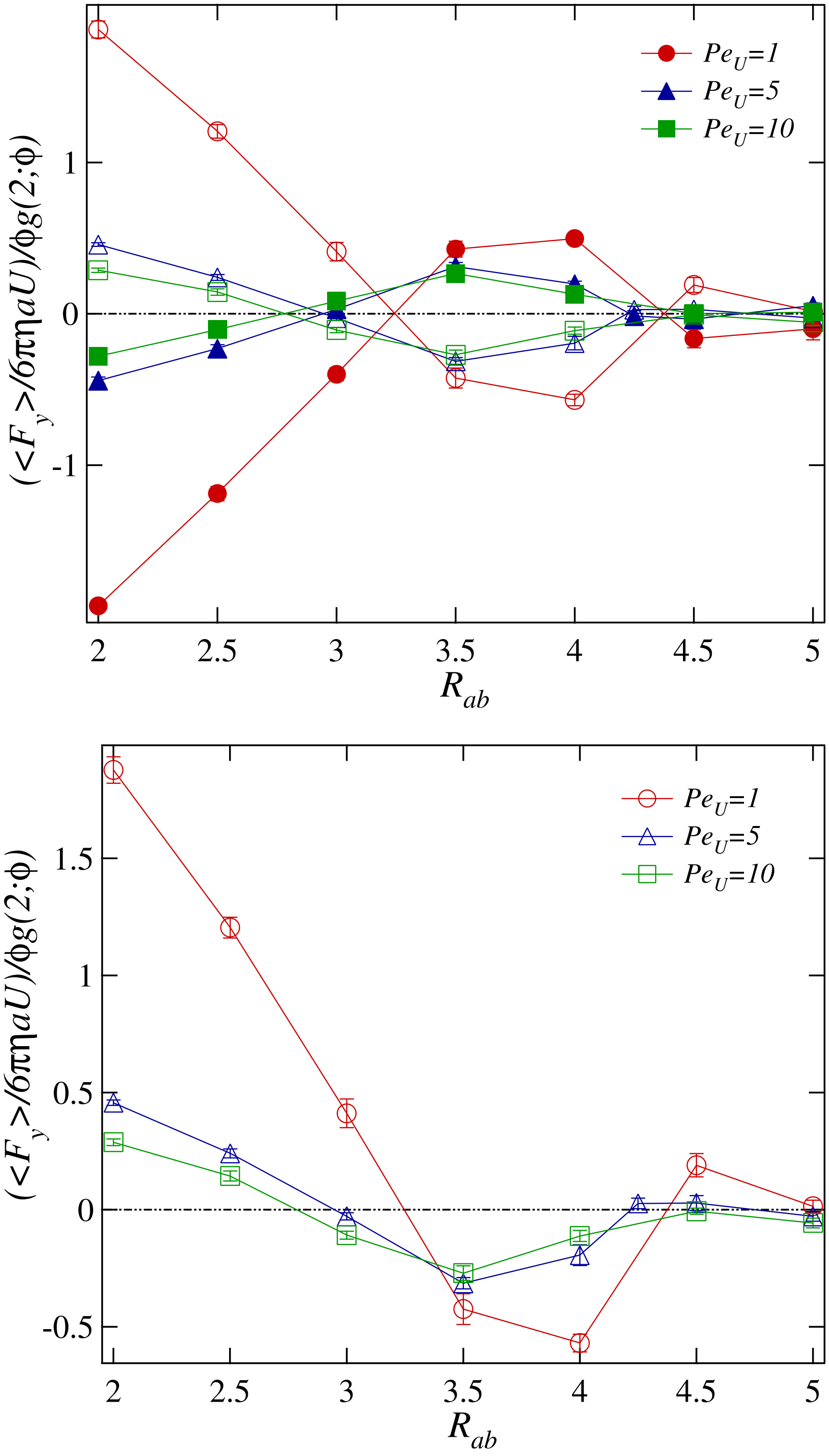

Figure 4.16: Both: a comparison of the forces applied in the y direction for the three different cases of probes separated by $R_{ab} = \Delta y$. Bottom: for simplicity, only one of the particles in each pair is shown. Interactions are stronger for the smaller Pe_U, and appear to be slightly longer ranged.

other when the separation about a particle radius or less, they repel each other when the separation is between a radius and two radii approximately, and the interaction dies out for longer distances. The force in the direction of travel is only slightly affected (the dashed red line represents the average force obtained in the single probe problem), and that effect is localized to the region where the interactions switch from repulsive to attractive.

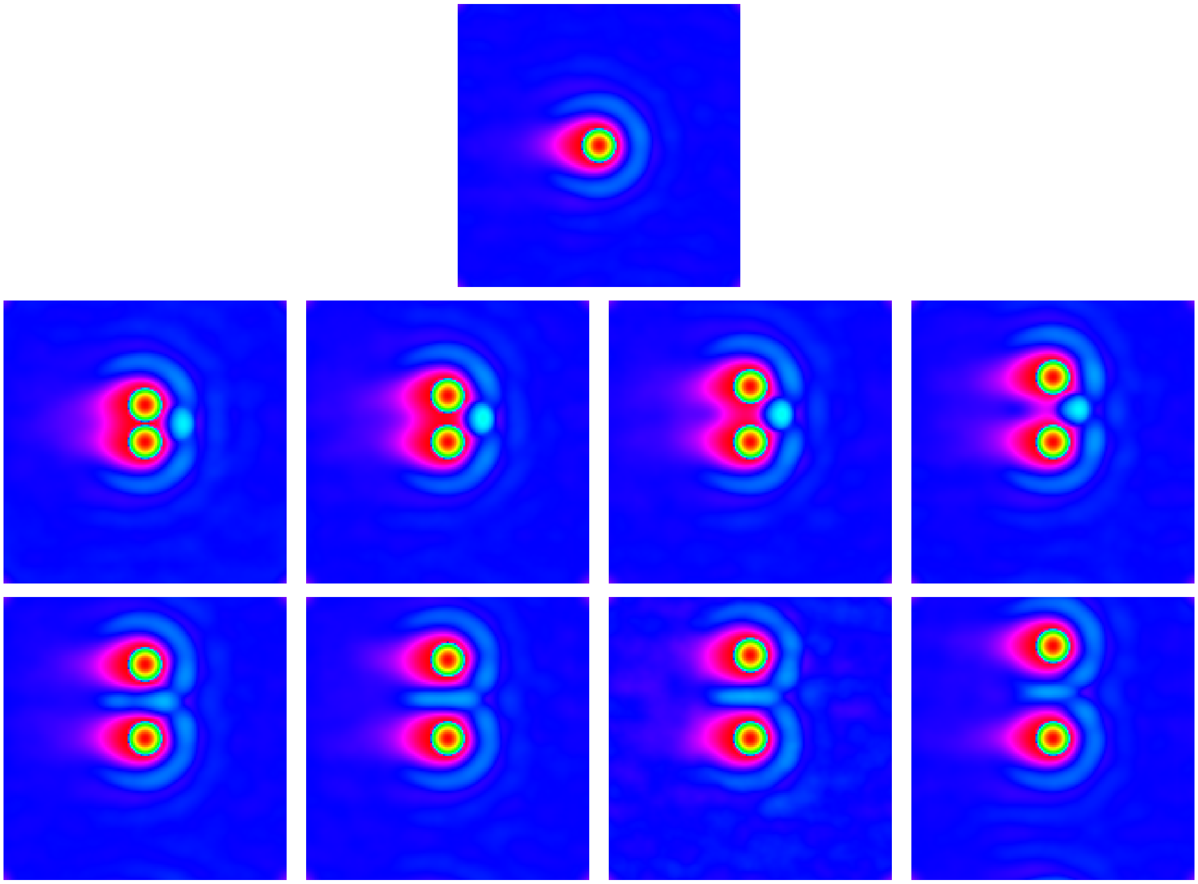

Figure 4.17: Brownian dynamics results for the average density around a pair of probe particles pulled with constant velocity for $\phi = 0.35$ for $Pe_U = Ua/D = 5$. Pictures shown are of the $x - y$ plane (x is the flow direction). Shown are cases of different separations Δy (transverse to the motion) between the probes. Total number of particles used for the simulations is 300. The very top picture is of the single probe problem (constant velocity) for $Pe_U = 5$, for comparison. From left to right: top row: $R_{ab} = \Delta y = 2, 2.5, 3, 3.5$; bottom row: $R_{ab} = \Delta y = 4, 4.25, 4.5, 5$. R_{ab} is the distance between particle centers, therefore $R_{ab} = 2$ indicates contact. The particles attract each other for $R_{ab} = 2, 2.5$, repel each other when the separation is greater, up to $R_{ab} < 4.25$, and do not have significant interactions for $R_a b \geq 4.25$.

Figures 4.13 and 4.14 illustrate the cases of $Pe_U = 5$ and $Pe_U = 10$ respectively, for which

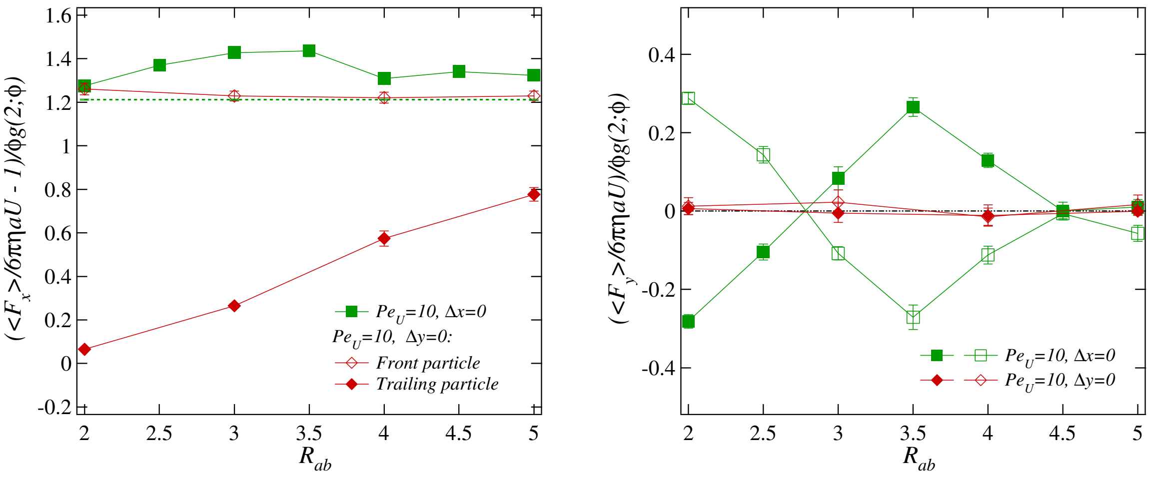

Figure 4.18: Left: a comparison of the forces applied in the direction of travel for the different cases of probes separated by $R_{ab} = \Delta y$ and probes separated by some $R_{ab} = \Delta x$ in the direction of travel. F_x is the same for both particles in the pair when $\Delta x = 0$, but not when one of the particles is moving behind the other close enough to be affected by the lower density region in the wake, especially when the trailing particle is directly behind the other. Thus the particle that is following (the solid rhombus) requires a smaller applied force to achieve the same velocity because it is subject to less resistance. Right: when $R_{ab} = \Delta x$ ($\Delta y = \Delta z = 0$), the symmetry in y results in F_y being the same for both particles.

the interactions between the particles are similar in character, but not magnitude. In Figures 4.15 and 4.16 we see a comparison between the three different cases, for the forces in the direction of travel F_x and the forces directed along the line of centers F_y. Force-thinning is seen in the difference in F_x, with the lower Péclet results corresponding to higher microviscosities. The same trend is seen for the interaction force, with the particles in the $Pe_U = 1$ case experiencing the strongest interactions. It also appears that the forces at lower Péclet are slightly longer ranged, although in all three cases the interactions appear to asymptote to the undisturbed (single probe) value for separations greater than one particle diameter. The corresponding density pictures are shown in Figure 4.17.

Finally, when one probe trails the other, we can see the strong effect upon the mobility of the trailing particle (see Figure 4.18). Compared to the previous case, for the probes separated by $R_{ab} = \Delta y$ at $Pe_U = 10$, the probes separated by some $R_{ab} = \Delta x \neq 0$ in the direction of travel do not need the same applied force F_x to move with the same velocity. This force is the same for both particles in the pair when $\Delta x = 0$, but not when one of the particles is moving behind the other close enough to be affected

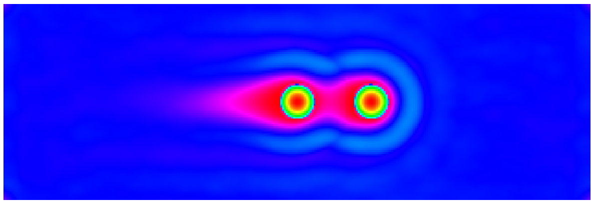

Figure 4.19: Brownian dynamics results for the average density around a pair of probe particles pulled with constant velocity for $\phi = 0.35$ and $Pe_U = Ua/D = 10$. The probes are separated by one particle diameter in the flow direction (one probe is trailing the other). Total number of particles used for the simulations is 300. Pictures shown are of the $x - y$ plane (x is the flow direction).

by the lower density region in the wake. The particle that is following requires a smaller applied force to achieve the same velocity because it is subject to less resistance. However, the symmetry in y results in F_y being the same for both particles. An example of a density profile for the trailing probe case is shown in Figure 4.19. It is logical to assume that if one were to fully examine the parameter space, allowing particles to be separated by some $\Delta x \neq 0$ and $\Delta y \neq 0$, one could map out some very rich behavior linked to depletion interactions.

4.5 Conclusions

Microrheology presents great opportunities in the study of complex materials—from biomaterials to colloids to gels—but it also presents great challenges in terms of reconciling its results with those of traditional macrorheology. This has in many respects limited the use of microrheology to the fairly well understood ‘passive’ regime of unforced probes, which only measures the linear viscoelastic properties of the material. However, the recent theoretical analyses by Squires and Brady [23] and Khair and Brady [18] have extended our understanding of microrheology in colloidal dispersions to the nonlinear, ‘active’ regime. The work shown here complements these theoretical analyses, presenting a study of active microrheology in colloids of finite and high volume fractions and providing a check on the theoretical predictions. The colloidal system chosen was well-defined and studied, allowing for a comparison to macrorheological results.

The agreement between the simple theory [23] and the simulation results was very good for the effective viscosity data, although there was no clear agreement and some differences between the relative fluctuations measured at finite volume fractions versus the dilute regime. The simulations also agreed with the theoretical analysis in showing that the viscosity measured when the probe is dragged with a constant velocity is consistently higher than in the constant force case, symptomatic of the greater resistance encountered when the probe cannot deviate from its path and has to force all bath particles out of its way. The simple theory also provided an excellent guide in terms of scaling, allowing us to collapse the effective microviscosity increment data for different volume fractions onto a single universal curve (with the exception of the high volume fraction, 55%, case, for $Pe < 100$). The apparent yield behavior shown by the 55% dispersion was also seen in experiments at high volume fractions [15]; it is not an effect that can be predicted by the simple dilute theory.

When interpreted as an effective viscosity, the microrheological measurements show force-thinning that closely resembles the shear-thinning of the macroviscosity for sheared suspensions. One of the most reassuring conclusions of this study is that the effective viscosity measured by microrheology shows the same qualitative (and almost quantitative) behavior as the viscosity measured using traditional rheology. However, one must take into consideration the different volume fraction scalings (in particular, the relevant dilute theories show that the microviscosity scales with ϕ, while the macroviscosity scales with ϕ^2). Yet, with the correct scaling, the quantitative differences are small, despite the fact that the two are fundamentally different—dipole versus quadrupole forcing. Evidently the essence of microstructural deformation and relaxation is captured by both micro and macro measurements. The microrheological studies also show a clear distinction between constant force and constant velocity probes, raising the question as to whether this distinction—constant shear rate vs. constant stress—is also manifest in nonlinear macrorheology.

The Brownian dynamics simulations have also allowed us to study the interactions between neighboring probe particles. When the particles are close enough to create a volume excluded to bath particles, the probes can attract or repel each other depending on the separation distance (when the separation is transverse to the direction of motion). A probe landing in another's wake will also experience a greater mobility, and therefore requires a smaller force to achieve the same velocity—it will therefore be attracted to the probe it is trailing. The effect of one probe upon another can be quite significant and shows the importance of the microstructural deformation upon the motion of any (probe) particle and therefore upon the measured microviscosity.

The current study ignored the effect of hydrodynamic interactions. However, we know from the behavior in macrorheological experiments and the theoretical work of Khair and Brady [18] that such interactions play an important role at higher Péclet numbers, where they result in force (or shear)-thickening. It would be interesting to perform the analogous microrheological simulations with hydrodynamics included and compare with their theoretical predictions as well as to macrorheology results. One can also consider the effects of factors such as the probe size (relative to the bath particles), size polydispersity in general, and interactions between multiple probes in further detail—these and other parameters may be very important in the microrheology context. Microrheology measurements are more strongly affected by the character of the material and the particulars of the probing method than the equivalent macrorheology measurements: on the positive side, this indicates that microrheological techniques can be quite sensitive. However, one should keep in mind, when comparing between micro and macro, that current microrheology measurements and techniques focus on obtaining the microviscosity, a scalar quantity, and cannot provide the full stress tensor for the material (at least with a single spherical particle). At the very least, microrheology can be used to provide information complementary to that obtained by macrorheology techniques and merits further study and development.

Bibliography

[1] M.P. Allen and D.J. Tildesley. *Computer Simulation of Liquids.* Oxford University Press, 1987.

[2] Y. Almog and H. Brenner. Non-continuum anomalies in the apparent viscosity experienced by a test sphere moving through an otherwise quiescent suspension. *Phys. Fluids*, 9:16–22, 1997.

[3] A. R. Bausch, F. Ziemann, A. A. Boulbitch, K. Jacobson, and E. Sackmann. Local measurements of

viscoelastic parameters of adherent cell surfaces by magnetic bead rheometry. *Biophys. J.*, 75:2038–2049, 1998.

[4] J. Bergenholtz, J.F. Brady, and M. Vicic. The non-Newtonian rheology of dilute colloidal suspensions. *J. Fluid Mech.*, 456:239–275, 2002.

[5] J.F. Brady. The long-time self-diffusivity in concentrated colloidal dispersions. *J. Fluid Mech.*, 272:109–133, 1994.

[6] V. Breedveld and D.J. Pine. Microrheology as a tool for high-throughput screening. *J. Mat. Sci.*, 38:4461–4470, 2003.

[7] J.C. Crocker. Measurement of the hydrodynamic corrections to the Brownian motion of two colloidal spheres. *J. Chem. Phys.*, 106:2837–2840, 1997.

[8] J.C. Crocker, J.A. Matteo, A.D. Dinsmore, and A.G. Yodh. Entropic attraction and repulsion in binary colloids probed with a line optical tweezer. *Phys. Rev. Lett.*, 82:4352–4355, 1999.

[9] J.C. Crocker, M.T. Valentine, E.R. Weeks, T. Gisler, P.D. Kaplan, A.G. Yodh, and D.A. Weitz. Two-point microrheology of inhomogeneous soft materials. *Phys. Rev. Lett.*, 85:888–891, 2000.

[10] D.R. Foss and J.F. Brady. Brownian Dynamics simulation of hard-sphere colloidal dispersions. *J. Rheol.*, 44:629–651, 2000.

[11] D.R. Foss and J.F. Brady. Structure, diffusion and rheology of Brownian suspensions by Stokesian Dynamics simulations. *J. Fluid Mech.*, 407:167–200, 2000.

[12] H. Freundlich and W. Seifriz. Über die elastizität von solen und gelen. *Z. Phys. Chem.*, 104:233–261, 1922.

[13] T. Gisler and D.A. Weitz. Scaling of the microrheology of semidilute F-actin solutions. *Phys. Rev. Lett.*, 82:1606–1609, 1999.

[14] W.H. Guilford, R.C. Lantz, and R.W. Gore. Locomotive forces produced by single leukocytes in-vivo and in-vitro. *Am. J. Physiol.–Cell Physiol.*, 37:C1308–C1312, 1995.

[15] P. Habdas, D. Schaar, A.C. Levitt, and E.R. Weeks. Forced motion of a probe particle near the colloidal glass transition. *Europhys. Lett.*, 67:477–483, 2004.

[16] L.E. Helseth and T.M. Fischer. Fundamental limits of optical microrheology. *J. Colloid Interf. Sci.*, 275:322–327, 2004.

[17] D.M. Heyes and J.R. Melrose. Brownian dynamics simulations of model hard-sphere suspensions. *J. Non-Newtonian Fluid Mech.*, 46:1–28, 1993.

[18] A. Khair and J.F. Brady. Active and nonlinear microrheology of dilute colloidal dispersions. Submitted to J. Fluid Mech.

[19] A.W.C. Lau, B.D. Hoffman, A. Davies, J.C. Crocker, and T.C. Lubensky. Microrheology, stress fluctuations, and active behavior of living cells. *Phys. Rev. Lett.*, 91:Art. No. 198101, 2003.

[20] F.C. MacKintosh and C.F. Schmidt. Microrheology. *Curr. Op. Colloid Interf. Sci.*, 4:300–307, 1999.

[21] T.G. Mason, K. Ganesan, J.H. vanZanten, D. Wirtz, and S.C. Kuo. Particle tracking microrheology of complex fluids. *Phys. Rev. Lett.*, 79:3282–3285, 1997.

[22] M.D. Rintoul and S. Torquato. Computer simulations of dense hard-sphere systems. *J. Chem. Phys.*, 105:9258–9265, 1996.

[23] T.M. Squires and J.F. Brady. A simple paradigm for active and nonlinear microrheology. Submitted to Phys. Fluids.

[24] J.C. van der Werff, C.G. de Kruif, C. Blom, and J. Mellema. Linear viscoelastic behavior of dense hard-sphere dispersions. *Phys. Rev. A*, 39:795–807, 1989.

[25] F. Ziemann, J. Radler, and E. Sackmann. Local measurements of viscoelastic moduli of entangled actin networks using an oscillating magnetic bead micro-rheometer. *Biophys. J.*, 66:2210–2216, 1994.

Table 4.1: The constant-force results for $\phi = 0.20$. The microviscosity is defined by $\eta^{micro} = (F/6\pi\eta a\langle U\rangle - 1)/\phi g(2;\phi)$ (using the Carnahan-Starling approximation for g); $Pe_F = Fa/kT$ is the force-based Péclet number and the mean velocity is non-dimensionalized by $F/6\pi\eta a$. ($\phi g(2;\phi) = 0.3516$)

Pe_F	$\langle U\rangle$	$\eta_{eff}/\eta - 1$	η^{micro}
0.20	0.6093 ± 0.0832	0.6706 ± 0.2173	1.9074 ± 0.6182
0.50	0.6397 ± 0.0315	0.5669 ± 0.0761	1.6124 ± 0.2165
1.00	0.6462 ± 0.0197	0.5489 ± 0.0475	1.5614 ± 0.1350
2.00	0.6681 ± 0.0159	0.4976 ± 0.0355	1.4153 ± 0.1009
5.00	0.6795 ± 0.0161	0.4726 ± 0.0358	1.3443 ± 0.1018
10.00	0.7134 ± 0.0070	0.4019 ± 0.0137	1.1433 ± 0.0390
20.00	0.7515 ± 0.0071	0.3308 ± 0.0126	0.9409 ± 0.0358
25.00	0.7554 ± 0.0089	0.3239 ± 0.0155	0.9214 ± 0.0441
50.00	0.7681 ± 0.0063	0.3021 ± 0.0107	0.8593 ± 0.0305
100.00	0.7820 ± 0.0102	0.2790 ± 0.0167	0.7936 ± 0.0476
200.00	0.7921 ± 0.0051	0.2625 ± 0.0082	0.7467 ± 0.0233
300.00	0.8060 ± 0.0093	0.2408 ± 0.0143	0.6850 ± 0.0406

Table 4.2: Simulation details for the $\phi = 0.20$ constant-force runs. The Péclet number is $Pe_F = Fa/kT$, N_p indicates the number of particles in the cell (including the probe particle), L_x, L_y, and L_z are the dimensions of the simulation cell, τ_{run} gives the run-length, and the time step used is $\Delta t = 0.0001$.

Pe_F	N_p	L_x	$L_y = L_z$	τ_{run}
0.20	300	18.453	18.453	5000.0
0.50	300	18.453	18.453	5000.0
1.00	300	18.453	18.453	5000.0
2.00	300	18.453	18.453	5000.0
5.00	300	18.453	18.453	5000.0
10.00	300	18.453	18.453	5000.0
20.00	300	18.453	18.453	5000.0
25.00	300	18.453	18.453	5000.0
50.00	500	55.129	13.782	5000.0
100.00	500	55.129	13.782	5000.0
200.00	600	76.766	12.794	5000.0
300.00	600	76.766	12.794	5000.0

Table 4.3: The constant-force results for $\phi = 0.35$. The microviscosity is defined by $\eta^{micro} = (F/6\pi\eta a\langle U\rangle - 1)/\phi g(2;\phi)$ (using the Carnahan-Starling approximation for g); $Pe_F = Fa/kT$ is the force-based Péclet number and the mean velocity is non-dimensionalized by $F/6\pi\eta a$. ($\phi g(2;\phi) = 1.0514$)

Pe_F	$\langle U\rangle$	$\eta_{eff}/\eta - 1$	η^{micro}
0.10	0.3264 ± 0.1434	1.4564 ± 90.0734	1.3852 ± 85.6672
0.20	0.2859 ± 0.1017	3.1353 ± 1.9223	2.9819 ± 1.8283
0.30	0.5118 ± 0.1208	1.1071 ± 0.6716	1.0530 ± 0.6388
0.40	0.3747 ± 0.0568	1.7320 ± 0.4201	1.6473 ± 0.3995
0.50	0.4312 ± 0.0404	1.3403 ± 0.2239	1.2747 ± 0.2130
1.00	0.4068 ± 0.0362	1.4781 ± 0.2272	1.4058 ± 0.2160
2.00	0.4343 ± 0.0232	1.3091 ± 0.1235	1.2451 ± 0.1175
5.00	0.4300 ± 0.0131	1.3275 ± 0.0729	1.2626 ± 0.0693
10.00	0.4531 ± 0.0076	1.2076 ± 0.0374	1.1485 ± 0.0356
25.00	0.5143 ± 0.0093	0.9451 ± 0.0349	0.8989 ± 0.0332
50.00	0.5699 ± 0.0109	0.7553 ± 0.0337	0.7184 ± 0.0321
100.00	0.5611 ± 0.0081	0.7826 ± 0.0256	0.7443 ± 0.0243
200.00	0.5890 ± 0.0096	0.6981 ± 0.0277	0.6640 ± 0.0263
300.00	0.5972 ± 0.0077	0.6748 ± 0.0219	0.6418 ± 0.0208
400.00	0.5998 ± 0.0088	0.6675 ± 0.0249	0.6349 ± 0.0237
500.00	0.6007 ± 0.0150	0.6659 ± 0.0413	0.6333 ± 0.0393

Table 4.4: Simulation details for the $\phi = 0.35$ constant-force runs. The Péclet number is $Pe_F = Fa/kT$, N_p indicates the number of particles in the cell (including the probe particle), L_x, L_y, and L_z are the dimensions of the simulation cell, τ_{run} gives the run-length, and the time step used is $\Delta t = 0.0001$.

Pe_F	N_p	L_x	$L_y = L_z$	τ_{run}
0.10	300	15.313	15.313	5000.0
0.20	300	15.313	15.313	5000.0
0.30	300	15.313	15.313	5000.0
0.40	300	15.313	15.313	5000.0
0.50	300	15.313	15.313	5000.0
1.00	300	15.313	15.313	5000.0
2.00	300	15.313	15.313	5000.0
5.00	300	15.313	15.313	5000.0
10.00	300	15.313	15.313	5000.0
25.00	300	15.313	15.313	5000.0
50.00	300	15.313	15.313	5000.0
100.00	1000	106.171	10.617	5000.0
200.00	500	53.086	10.617	5000.0
300.00	600	63.703	10.617	5000.0
400.00	1000	106.171	10.617	5000.0
500.00	1000	106.171	10.617	5000.0

Table 4.5: The constant-force results for $\phi = 0.45$. The microviscosity is defined by $\eta^{micro} = (F/6\pi\eta a\langle U\rangle - 1)/\phi g(2;\phi)$ (using the Carnahan-Starling approximation for g); $Pe_F = Fa/kT$ is the force-based Péclet number and the mean velocity is non-dimensionalized by $F/6\pi\eta a$. ($\phi g(2;\phi) = 2.0962$)

Pe_F	$\langle U\rangle$	$\eta_{eff}/\eta - 1$	η^{micro}
0.50	0.1849 ± 0.0670	5.0691 ± 1.9421	2.4183 ± 0.9265
1.00	0.1985 ± 0.0188	4.0805 ± 0.4694	1.9467 ± 0.2240
2.00	0.2159 ± 0.0316	3.7365 ± 0.7316	1.7825 ± 0.3490
5.00	0.2314 ± 0.0173	3.3453 ± 0.3148	1.5959 ± 0.1502
10.00	0.2492 ± 0.0111	3.0202 ± 0.1765	1.4408 ± 0.0842
25.00	0.3244 ± 0.0120	2.0866 ± 0.1159	0.9954 ± 0.0553
50.00	0.3851 ± 0.0054	1.5972 ± 0.0360	0.7620 ± 0.0172
100.00	0.4163 ± 0.0085	1.4033 ± 0.0493	0.6695 ± 0.0235
200.00	0.4275 ± 0.0080	1.3399 ± 0.0440	0.6392 ± 0.0210
300.00	0.4179 ± 0.0040	1.3932 ± 0.0231	0.6647 ± 0.0110

Table 4.6: Simulation details for the $\phi = 0.45$ constant-force runs. The Péclet number is $Pe_F = Fa/kT$, N_p indicates the number of particles in the cell (including the probe particle), L_x, L_y, and L_z are the dimensions of the simulation cell, τ_{run} gives the run-length, and the time step used is $\Delta t = 0.0001$.

Pe_F	N_p	L_x	$L_y = L_z$	τ_{run}
0.50	300	14.082	14.082	5000.0
1.00	300	14.082	14.082	5000.0
2.00	300	14.082	14.082	5000.0
5.00	300	14.082	14.082	5000.0
10.00	300	14.082	14.082	5000.0
25.00	300	14.082	14.082	5000.0
50.00	300	14.082	14.082	5000.0
100.00	300	22.354	11.177	5000.0
200.00	400	39.056	9.764	5000.0
300.00	600	58.584	9.764	5000.0

Table 4.7: The constant-force results for $\phi = 0.55$. The microviscosity is defined by $\eta^{micro} = (F/6\pi\eta a\langle U\rangle - 1)/\phi g(2;\phi)$ (using the Carnahan-Starling approximation for g); $Pe_F = Fa/kT$ is the force-based Péclet number and the mean velocity is non-dimensionalized by $F/6\pi\eta a$. ($\phi g(2;\phi) = 4.3759$)

Pe_F	$\langle U\rangle$	$\eta_{eff}/\eta - 1$	η^{micro}
5.00	0.0021 ± 0.0101	59.6430 ± 8549.3746	13.6300 ± 1953.7599
10.00	0.0114 ± 0.0059	168.5457 ± 5303.4833	38.5172 ± 1211.9873
15.00	0.0079 ± 0.0098	-62.5029 ± 6223.4379	-14.2836 ± 1422.2214
25.00	0.0963 ± 0.0309	11.1079 ± 5.9453	2.5385 ± 1.3587
50.00	0.1453 ± 0.0106	5.9178 ± 0.4984	1.3524 ± 0.1139
100.00	0.2473 ± 0.0104	3.0514 ± 0.1674	0.6973 ± 0.0383
200.00	0.2252 ± 0.0051	3.4427 ± 0.1006	0.7867 ± 0.0230
300.00	0.2427 ± 0.0006	3.1205 ± 0.0097	0.7131 ± 0.0022

Table 4.8: Simulation details for the $\phi = 0.55$ constant-force runs. The Péclet number is $Pe_F = Fa/kT$, N_p indicates the number of particles in the cell (including the probe particle), L_x, L_y, and L_z are the dimensions of the simulation cell, τ_{run} gives the run-length, and the time step used is $\Delta t = 0.0001$.

Pe_F	N_p	L_x	$L_y = L_z$	τ_{run}
5.00	300	13.171	13.171	5000.0
10.00	300	13.171	13.171	5000.0
15.00	300	13.171	13.171	5000.0
25.00	300	13.171	13.171	5000.0
50.00	300	13.171	13.171	5000.0
100.00	300	13.171	13.171	5000.0
200.00	300	27.397	9.132	5000.0
300.00	500	39.349	9.837	5000.0

Table 4.9: The constant-velocity results for $\phi = 0.35$. The microviscosity is defined by $\eta^{micro} = (\langle F \rangle / 6\pi\eta a U - 1)/\phi g(2;\phi)$ (using the Carnahan-Starling approximation for g); $Pe_U = Ua/D$ is the velocity-based Péclet number and the mean force is non-dimensionalized by $6\pi\eta a U$. ($\phi g(2;\phi) = 1.0514$)

Pe_U	$\langle F \rangle$	$\eta_{eff}/\eta - 1$	η^{micro}
0.10	3.1063 ± 0.3627	2.1063 ± 0.3627	2.0032 ± 0.3450
0.30	3.1114 ± 0.1421	2.1114 ± 0.1421	2.0081 ± 0.1352
1.00	2.9548 ± 0.0498	1.9548 ± 0.0498	1.8592 ± 0.0474
5.00	2.4950 ± 0.0362	1.4950 ± 0.0362	1.4219 ± 0.0345
10.00	2.3071 ± 0.0218	1.3071 ± 0.0218	1.2431 ± 0.0207
13.00	2.2183 ± 0.0240	1.2183 ± 0.0240	1.1587 ± 0.0228
28.30	2.0933 ± 0.0236	1.0933 ± 0.0236	1.0398 ± 0.0225
50.00	2.0145 ± 0.0205	1.0145 ± 0.0205	0.9649 ± 0.0195
100.00	1.9638 ± 0.0186	0.9638 ± 0.0186	0.9167 ± 0.0177

Table 4.10: Simulation details for the $\phi = 0.35$ constant-velocity runs. The Péclet number is $Pe_U = Ua/D$, N_p indicates the number of particles in the cell (including the probe particle), L_x, L_y, and L_z are the dimensions of the simulation cell, τ_{run} gives the run-length, and the time step used is $\Delta t = 0.0001$.

Pe_U	N_p	L_x	$L_y = L_z$	τ_{run}
0.10	300	15.313	15.313	5000.0
0.30	300	15.313	15.313	5000.0
1.00	300	15.313	15.313	5000.0
5.00	300	15.313	15.313	5000.0
10.00	300	31.851	10.617	5000.0
13.00	300	31.851	10.617	5000.0
28.30	300	38.585	9.646	5000.0
50.00	400	49.280	9.856	5000.0
100.00	1000	106.171	10.617	5000.0

Table 4.11: The constant-velocity results for $Pe_U = 1$. The microviscosity is defined by $\eta^{micro} = (\langle F\rangle/6\pi\eta a U - 1)/\phi g(2;\phi)$ (using the Carnahan-Starling approximation for g); $Pe_U = Ua/D$ is the velocity-based Péclet number and the mean force is non-dimensionalized by $6\pi\eta a U$.

ϕ	$\langle F\rangle$	$\eta_{eff}/\eta - 1$	η^{micro}
0.15	1.5797 ± 0.0384	0.5797 ± 0.0384	2.5658 ± 0.1700
0.35	2.9548 ± 0.0498	1.9548 ± 0.0498	1.8592 ± 0.0474

Table 4.12: The constant-velocity results for $Pe_U = 5$. The microviscosity is defined by $\eta^{micro} = (\langle F\rangle/6\pi\eta a U - 1)/\phi g(2;\phi)$ (using the Carnahan-Starling approximation for g); $Pe_U = Ua/D$ is the velocity-based Péclet number and the mean force is non-dimensionalized by $6\pi\eta a U$.

ϕ	$\langle F\rangle$	$\eta_{eff}/\eta - 1$	η^{micro}
0.15	1.4439 ± 0.0233	0.4439 ± 0.0233	1.9647 ± 0.1031
0.25	1.8664 ± 0.0148	0.8664 ± 0.0148	1.6709 ± 0.0285
0.35	2.4950 ± 0.0362	1.4950 ± 0.0362	1.4219 ± 0.0345
0.45	3.8624 ± 0.0448	2.8624 ± 0.0448	1.3655 ± 0.0214
0.55	6.7257 ± 0.2983	5.7257 ± 0.2983	1.3085 ± 0.0682

Table 4.13: Simulation details for the $Pe_U = 1$ and $Pe_U = 5$ constant-velocity runs. The Péclet number is $Pe_U = Ua/D$, ϕ the volume fraction, N_p indicates the number of particles in the cell (including the probe particle), L_x, L_y, and L_z are the dimensions of the simulation cell, τ_{run} gives the run-length, and the time step used is $\Delta t = 0.0001$.

Pe_U	ϕ	N_p	L_x	$L_y = L_z$	τ_{run}
1	0.15	500	60.678	15.169	5000.0
1	0.35	300	15.313	15.313	5000.0
5	0.15	500	60.678	15.169	5000.0
5	0.25	300	35.632	11.877	5000.0
5	0.35	300	15.313	15.313	5000.0
5	0.45	300	14.082	14.082	5000.0
5	0.55	300	13.171	13.171	5000.0

Table 4.14: The long-time self-diffusivity D^s_∞ for a Brownian suspension ($Pe = 0$) as a function of volume fraction. The long-time self-diffusivity is scaled by the Stokes-Einstein diffusivity D; the results were obtained for systems of 300 particles.

ϕ	D^s_∞
0.10	0.8524
0.20	0.6821
0.30	0.5098
0.35	0.4185
0.40	0.3192
0.50	0.1237
0.55	0.0267
0.60	0.0082

Table 4.15: The constant-force velocity fluctuation results for $\phi = 0.20$. The velocities (fluctuations thereof) are non-dimensionalized by $F/6\pi\eta a$. U' indicates a fluctuation in the direction of the applied force; V' indicates fluctuations in the (2) directions transverse to the external force. The sampling time step is 0.001.

Pe_F	$\langle U'U' \rangle$	$\langle V'V' \rangle$	$\langle U'U' \rangle / \langle V'V' \rangle$
0.20	1125.8463	1114.5635	1.0101
0.50	179.7960	181.2289	0.9921
1.00	45.8433	46.0628	0.9952
2.00	16.9768	17.4376	0.9736
5.00	5.4923	5.3891	1.0192
10.00	2.7799	2.5087	1.1081
20.00	1.5130	1.2858	1.1767
25.00	1.3073	1.0499	1.2451
50.00	0.8426	0.6484	1.2995
100.00	0.5527	0.3831	1.4426
200.00	0.3730	0.2416	1.5441
300.00	0.2349	0.1591	1.4765

Table 4.16: The constant-force velocity fluctuation results for $\phi = 0.35$. The velocities (fluctuations thereof) are non-dimensionalized by $F/6\pi\eta a$. U' indicates a fluctuation in the direction of the applied force; V' indicates fluctuations in the (2) directions transverse to the external force. The sampling time step is 0.001.

Pe_F	$\langle U'U' \rangle$	$\langle V'V' \rangle$	$\langle U'U' \rangle / \langle V'V' \rangle$
0.10	12846.5642	12888.0204	0.9968
0.20	3225.4347	3213.9103	1.0036
0.30	1421.5845	1433.7603	0.9915
0.40	807.3519	806.6959	1.0008
0.50	516.3829	516.5483	0.9997
1.00	129.5296	130.2489	0.9945
2.00	47.5806	47.8086	0.9952
5.00	13.3595	13.5969	0.9825
10.00	5.9671	5.8075	1.0275
25.00	2.6173	2.3109	1.1326
50.00	1.5575	1.2570	1.2391
100.00	1.0876	0.7890	1.3783
200.00	0.7016	0.4890	1.4346
400.00	0.4771	0.3250	1.4678
500.00	0.4235	0.2819	1.5021

Table 4.17: The constant-force velocity fluctuation results for $\phi = 0.45$. The velocities (fluctuations thereof) are non-dimensionalized by $F/6\pi\eta a$. U' indicates a fluctuation in the direction of the applied force; V' indicates fluctuations in the (2) directions transverse to the external force. The sampling time step is 0.001.

Pe_F	$\langle U'U' \rangle$	$\langle V'V' \rangle$	$\langle U'U' \rangle / \langle V'V' \rangle$
0.50	977.0603	973.4298	1.0037
1.00	244.0539	244.5653	0.9979
2.00	90.5158	90.8341	0.9965
5.00	24.7579	24.9001	0.9943
10.00	10.1160	10.1746	0.9942
25.00	3.9420	3.6890	1.0686
50.00	2.2340	2.0001	1.1169
100.00	1.4160	1.1569	1.2240
200.00	0.9490	0.7023	1.3513
300.00	0.7295	0.5357	1.3619

Table 4.18: The constant-force velocity fluctuation results for $\phi = 0.55$. The velocities (fluctuations thereof) are non-dimensionalized by $F/6\pi\eta a$. U' indicates a fluctuation in the direction of the applied force; V' indicates fluctuations in the (2) directions transverse to the external force. The sampling time step is 0.001.

Pe_F	$\langle U'U' \rangle$	$\langle V'V' \rangle$	$\langle U'U' \rangle / \langle V'V' \rangle$
5.00	33.1619	39.7972	0.8333
10.00	14.2130	15.1365	0.9390
15.00	9.8197	8.7059	1.1279
25.00	5.9874	5.0855	1.1773
50.00	3.4067	3.2087	1.0617
100.00	1.8441	1.6130	1.1433
200.00	1.2724	1.0310	1.2342
300.00	0.9958	0.7257	1.3722

Table 4.19: The constant-velocity two-particle results for $Pe_U = 1$, $\phi = 0.35$. The mean forces are non-dimensionalized by $6\pi\eta aU$. x is the direction in which the probe particles are traveling, y is the direction (transverse to this motion) in which we choose to separate them. The centers of the particles are separated by a distance R_{ab} in the y direction, but not in x or z—thus, the center-to-center distance is R_{ab}. ($R_{ab} = 2$ corresponds to contact.) The forces in this table are the forces that are imposed on the particles to keep them moving with a constant velocity $\boldsymbol{U} = (U, 0, 0)$. Superscripts 1 and 2 are used to indicate particles 1 and 2 respectively, with particle 1 being at a lower y than particle 2.

R_{ab}	$\langle F_x^1 \rangle$	$\langle F_y^1 \rangle$	$\langle F_x^2 \rangle$	$\langle F_y^2 \rangle$
2.00	2.9482 ± 0.0454	-2.0286 ± 0.0380	2.9203 ± 0.0290	1.9745 ± 0.0589
2.50	3.1000 ± 0.0455	-1.2487 ± 0.0501	3.0741 ± 0.0828	1.2667 ± 0.0470
3.00	3.1956 ± 0.0465	-0.4202 ± 0.0461	3.2321 ± 0.0701	0.4321 ± 0.0644
3.50	3.2142 ± 0.0525	0.4486 ± 0.0548	3.2007 ± 0.0700	-0.4464 ± 0.0690
4.00	3.0241 ± 0.0164	0.5228 ± 0.0270	3.0149 ± 0.0367	-0.5988 ± 0.0394
4.50	3.0290 ± 0.0450	-0.1722 ± 0.0642	3.0039 ± 0.0384	0.1996 ± 0.0517
5.00	3.0751 ± 0.0273	-0.1041 ± 0.0776	2.9794 ± 0.0357	0.0156 ± 0.0267

Table 4.20: Simulation details for the $Pe_U = 1$, $\phi = 0.35$ two-particle runs. The center-to-center distance between the two probes is $R_ab = \Delta y$ and τ_{run} gives the run-length. All simulations used $N_p = 300$ particles in the cell (including the probe particles), with $L_x = L_y = L_z = 15.313$ as the dimensions of the simulation cell; the time step used is $\Delta t = 0.0001$.

R_{ab}	τ_{run}
2.00	4790.0
2.50	5595.0
3.00	4786.0
3.50	4063.0
4.00	5000.0
4.50	5589.0
5.00	5000.0

Table 4.21: The constant-velocity two-particle results for $Pe_U = 5$, $\phi = 0.35$. The mean forces are non-dimensionalized by $6\pi\eta aU$. x is the direction in which the probe particles are traveling, y is the direction (transverse to this motion) in which we choose to separate them. The centers of the particles are separated by a distance R_{ab} in the y direction, but not in x or z—thus, the center-to-center distance is R_{ab}. ($R_{ab} = 2$ corresponds to contact.) The forces in this table are the forces that are imposed on the particles to keep them moving with a constant velocity $\boldsymbol{U} = (U, 0, 0)$. Superscripts 1 and 2 are used to indicate particles 1 and 2 respectively, with particle 1 being at a lower y than particle 2.

R_{ab}	$\langle F_x^1 \rangle$	$\langle F_y^1 \rangle$	$\langle F_x^2 \rangle$	$\langle F_y^2 \rangle$
2.00	2.4835 ± 0.0209	-0.4644 ± 0.0245	2.4663 ± 0.0413	0.4805 ± 0.0118
2.50	2.6020 ± 0.0396	-0.2421 ± 0.0280	2.6157 ± 0.0244	0.2527 ± 0.0201
3.00	2.6814 ± 0.0166	0.0313 ± 0.0281	2.7044 ± 0.0264	-0.0301 ± 0.0159
3.50	2.7036 ± 0.0260	0.3286 ± 0.0287	2.7239 ± 0.0260	-0.3304 ± 0.0259
4.00	2.5617 ± 0.0173	0.2061 ± 0.0207	2.5328 ± 0.0409	-0.2042 ± 0.0469
4.25	2.5410 ± 0.0241	-0.0159 ± 0.0372	2.5374 ± 0.0529	0.0281 ± 0.0239
4.50	2.5848 ± 0.0250	-0.0367 ± 0.0224	2.5737 ± 0.0315	0.0297 ± 0.0327
5.00	2.5616 ± 0.0214	0.0563 ± 0.0179	2.5648 ± 0.0344	-0.0300 ± 0.0221

Table 4.22: Simulation details for the $Pe_U = 5$, $\phi = 0.35$ two-particle runs. The center-to-center distance between the two probes is $R_ab = \Delta y$ and τ_{run} gives the run-length. All simulations used $N_p = 300$ particles in the cell (including the probe particles), with $L_x = L_y = L_z = 15.313$ as the dimensions of the simulation cell; the time step used is $\Delta t = 0.0001$.

R_{ab}	τ_{run}
2.00	5000.0
2.50	5000.0
3.00	5000.0
3.50	5000.0
4.00	5000.0
4.25	5000.0
4.50	5000.0
5.00	5000.0

Table 4.23: The constant-velocity two-particle results for $Pe_U = 10$, $\phi = 0.35$. The mean forces are non-dimensionalized by $6\pi\eta aU$. x is the direction in which the probe particles are traveling, y is the direction (transverse to this motion) in which we choose to separate them. The centers of the particles are separated by a distance R_{ab} in the y direction, but not in x or z—thus, the center-to-center distance is R_{ab}. ($R_{ab} = 2$ corresponds to contact.) The forces in this table are the forces that are imposed on the particles to keep them moving with a constant velocity $\boldsymbol{U} = (U, 0, 0)$. Superscripts 1 and 2 are used to indicate particles 1 and 2 respectively, with particle 1 being at a lower y than particle 2.

R_{ab}	$\langle F_x^1 \rangle$	$\langle F_y^1 \rangle$	$\langle F_x^2 \rangle$	$\langle F_y^2 \rangle$
2.00	2.3408 ± 0.0221	-0.2959 ± 0.0181	2.3379 ± 0.0218	0.3026 ± 0.0150
2.50	2.4405 ± 0.0202	-0.1097 ± 0.0212	2.4628 ± 0.0174	0.1510 ± 0.0221
3.00	2.5016 ± 0.0222	0.0878 ± 0.0308	2.5168 ± 0.0279	-0.1138 ± 0.0179
3.50	2.5102 ± 0.0285	0.2794 ± 0.0251	2.4853 ± 0.0207	-0.2851 ± 0.0331
4.00	2.3766 ± 0.0218	0.1362 ± 0.0191	2.3890 ± 0.0214	-0.1177 ± 0.0242
4.50	2.4101 ± 0.0203	0.0001 ± 0.0242	2.3833 ± 0.0176	-0.0069 ± 0.0135
5.00	2.3921 ± 0.0272	0.0106 ± 0.0203	2.3768 ± 0.0307	-0.0598 ± 0.0215

Table 4.24: Simulation details for the $Pe_U = 10$, $\phi = 0.35$ two-particle runs. The center-to-center distance between the two probes is $R_ab = \Delta y$ and τ_{run} gives the run-length. All simulations used $N_p = 300$ particles in the cell (including the probe particles), with $L_x = 24.307$ and $L_y = L_z = 12.154$ as the dimensions of the simulation cell; the time step used is $\Delta t = 0.0001$.

R_{ab}	τ_{run}
2.00	5000.0
2.50	5000.0
3.00	5000.0
3.50	5000.0
4.00	5000.0
4.50	5000.0
5.00	5000.0

Table 4.25: The constant-velocity two-particle results for $Pe_U = 10$, $\phi = 0.35$. The mean forces are non-dimensionalized by $6\pi\eta aU$. x is the direction in which the probe particles are traveling, y is one of the directions transverse to this motion. The centers of the particles are separated by a distance R_{ab} in the x direction, but not in y or z—thus, the center-to-center distance is R_{ab}. ($R_{ab} = 2$ corresponds to contact.) The forces in this table are the forces that are imposed on the particles to keep them moving with a constant velocity $\boldsymbol{U} = (U, 0, 0)$. Superscripts 1 and 2 are used to indicate particles 1 and 2 respectively, with particle 1 trailing particle 2.

R_{ab}	$\langle F_x^1 \rangle$	$\langle F_y^1 \rangle$	$\langle F_x^2 \rangle$	$\langle F_y^2 \rangle$
2.00	1.0677 ± 0.0034	0.0069 ± 0.0160	2.3260 ± 0.0282	0.0131 ± 0.0228
3.00	1.2785 ± 0.0102	-0.0054 ± 0.0253	2.2919 ± 0.0233	0.0241 ± 0.0328
4.00	1.6035 ± 0.0370	-0.0120 ± 0.0286	2.2840 ± 0.0259	-0.0151 ± 0.0235
5.00	1.8169 ± 0.0326	-0.0006 ± 0.0115	2.2929 ± 0.0225	0.0176 ± 0.0259

Table 4.26: Simulation details for the $Pe_U = 10$, $\phi = 0.35$ two-particle runs. The center-to-center distance between the two probes is $R_ab = \Delta x$ and τ_{run} gives the run-length. All simulations used $N_p = 300$ particles in the cell (including the probe particles), with $L_x = 31.851$ and $L_y = L_z = 10.617$ as the dimensions of the simulation cell; the time step used is $\Delta t = 0.0001$.

R_{ab}	τ_{run}
2.00	5000.0
3.00	5000.0
4.00	5000.0
5.00	5000.0

Chapter 5

Conclusions

In chapters 2 and 3 we have shown two examples of instability mechanisms that may affect suspensions and other complex fluids that share similar characteristics. In chapter 2 we analyzed an interfacial instability that was driven by a jump in the second normal stress difference across that interface. We found that such a jump in the normal stresses can lead to a growing instability transverse to the main flow, and think that this mechanism may explain the instability that leads to the band formation in the viscous suspension experiments of Tirumkudulu and coworkers [5], although since the experimental observations are for fully-developed and nonlinear effects a direct comparison is not possible. The cylindrical geometry of the experiments would also add other complications. Our analysis found that the most unstable wavelength was typically on the order of the thickness of the suspension layer, with the growth rate proportional to the shear rate and the second normal stress difference [1].

In chapter 3 we analyzed an instability driven by the stratification of density within a flowing suspension. In a non-neutrally buoyant suspension, the shearing motion generates a density profile that increases with height, leading to this Rayleigh-Taylor-like instability that allows perturbations transverse to the flow to grow. Although we are not aware of comparable experiments for viscous suspension flows, a similar mechanism was shown for a qualitatively similar granular flow [3], where they obtained longitudinal vortices (and a transverse wave pattern on the surface of their flow). The most unstable wavelength of our system was also quite close to the observed granular flow instability wavelength. The most unstable wavelength was on the order of the channel height, but the growth rate of the instability was very small, indicating that this instability is not very strong in viscous suspensions and would require either a long time and/or a long distance to develop [2]. In addition, a real system would also be subject to the second-normal stress difference instability discussed in chapter 2, a possibility which was not included in the present analysis.

The instabilities studied in chapters 2 and 3 may lead to pattern formation in suspensions. Pattern formation (due to migration of particles into particle-rich regions) is an effect that shows up when an instability has entered the nonlinear regime, and can therefore be suggested by the linear analyses performed, but would require nonlinear analysis in order to determine whether the patterns result from these initial instabilities or from other mechanisms.

In chapter 4 we numerically studied ‘active’ microrheology and the transition from the linear to the nonlinear regime. We did this by choosing a prototypical example, the motion of a particle due to an imposed force (or velocity) through a colloidal suspension. Colloids have been well-studied both experimentally and theoretically, and allowed us to compare our microrheological results to the results of macrorheology. The movement of the tracer through the suspension generates a resistance from the disturbed microstructure (there is a buildup of particle density on the front of the tracer and a low-density wake region behind) which retards the tracer’s motion. This system displays ‘shear-thinning’, similarly to the macrorheological sheared suspension, but the comparison is not exact (and the scaling with volume fraction is also different). We note therefore that the use and application of microrheological results needs to be carefully considered. Also, comparable length scales between the measurement device (the tracer) and the medium lead to interesting effects and distinctions between types of microrheological methods. For instance, we see differences between applying a constant force versus a constant velocity to the tracer—the measured microviscosity is always higher in the constant velocity case. The simulations compare well to the simple dilute theory results [4] but also allow us to see high-concentration effects such as yielding behavior, which cannot be captured by the simple theory. In addition, we look at the effect of tracers upon each other—neighboring tracers may attract or repel each other depending on their relative separation (which can result in an excluded volume effect for the surrounding particles). These type of microrheological measurements can provide very useful and interesting information, and can be used to study novel problems and old problems in a novel way.

Bibliography

[1] J.F. Brady and I.C. Carpen. Second normal stress jump instability in non-Newtonian fluids. *J. Non-Newtonian Fluid Mech.*, 102:219–232, 1997.

[2] I.C. Carpen and J.F. Brady. Gravitational instability in suspension flow. *J. Fluid Mech.*, 472:201–210, 2002.

[3] Y. Forterre and O. Pouliquen. Longitudinal vortices in granular flows. *Phys. Rev. Lett.*, 86:5886–5889, 2001.

[4] T.M. Squires and J.F. Brady. A simple paradigm for active and nonlinear microrheology. Submitted to Phys. Fluids.

[5] M. Tirumkudulu, A. Mileo, and A. Acrivos. Particle segregation in monodisperse sheared suspensions in a partially filled rotating horizontal cylinder. *Phys. Fluids*, 12:1615–1618, 2000.